SIGNIFICANCE OF POTASSIUM HOMEOSTASIS FOR NEURODEGENERATION IN GLAUCOMA

By

Rachel A. Fischer

Dissertation
Submitted to the Faculty of the
Graduate School of Vanderbilt University
in partial fulfillment of the requirements
for the degree of
DOCTOR OF PHILOSOPHY
in
Pharmacology
September 30, 2019
Nashville, Tennessee

Approved:

Rebecca M. Sappington, Ph.D.
Jerod S. Denton, Ph.D.
David J. Calkins, Ph.D.
C. David Weaver, Ph.D.
Yaqiong Xu, Ph.D.

I dedicate this doctoral dissertation to my parents—Sue and Peter, and my siblings—Nissa, Mike, and Karin. Thank you for your support, love, and encouragement over the past five years.

ACKNOWLEDGEMENTS

The work presented in this dissertation was a collaborative effort and I would like to extend my thanks and acknowledgements to many people who have helped me along the way. First and foremost, I would like to thank my advisor, Dr. Rebecca Sappington. Her support and mentorship throughout my graduate school career was invaluable and has made me a better scientist. Along with Dr. Sappington, my dissertation committee provided me with excellent guidance. Dr. David Calkins was always a constant presence in the lab and offered me support, encouragement, and advice whenever I needed it. Dr. Jerod Denton has been an excellent committee chair and I am very thankful to have had his support. Dr. Dave Weaver has not only provided me with guidance during committee meetings, but was also generous enough to help me set up a new experiment in the Sappington lab and provide me with reagents. Finally, thank you to Dr. Yaqiong Xu for being a great committee member and collaborator.

I have been very fortunate to have an amazing and inspiring group of colleagues to work with in the Sappington lab. A big thank you to Cathryn Formichella, M.S. for being an outstanding lab manager and friend from my first day in lab. Thank you to Dr. Franklin Echevarria for his guidance as I first joined the lab and all of his advice and encouragement. I would not have made it through the last few years of graduate school without the friendship, guidance, and everyday support provided by Dr. Lauren Wareham. Thank you from the bottom of my heart. And thank you to my fellow pharmacology graduate student, Rebecca Weiner. I would like to thank the undergraduate students that I’ve had the privilege to mentor including Abigail Roux, Hannah Mallaro, and Steven Patalano. I thank them for all their hard work and contributions to my dissertation project. Finally, I would like to thank all of the other members of

the Sappington Lab, past and present, including William McLaughlin, Stephen Davis, Noah Vasilakes, Abigayle Waterson, Emma Kingsbury, Michael Dublin, Brandy Sweet, Priya Sankaran, Sean Lee, Jeremy Britt Hatcher, Emily Sanford, PJ Goralski, and Gabby Dallas for providing a great work environment.

The Sappington lab and the Vanderbilt Vision Research Center are very collaborative environments and I would like to thank some of the people who have helped me with experiments over the years. Thank you to Dr. Wendi Lambert for help with microbead injections and for your advice and help whenever I asked. I would like to thank Dr. David Calkins and Dr. Michael Risner for their expertise and help with all of the electrophysiology experiments. I had the opportunity to participate in a collaboration between the Sappington lab and two engineering labs, the Li and Xu labs. For their help on those projects, I would like to thank Dr. Deyu Li, Dr. Kirsten Dodson, Matthew Fitzgerald, Alberto Esteban Linares, Dr. Yaqiong Xu, Yuchen Zhang, and Thayer Walmsley. Additionally, I would like to thank all of the members of the Vanderbilt Vision Research Center community for their support. A special thank you to all the members of the Calkins, Rex, Kuchtey, and Brantley labs for providing a fun and collaborative work environment. Finally, much of the data I have published has been collected with the help of Vanderbilt core staff including, Dr. Purnima Ghose of the Vision Research Center Histology Core, the Vanderbilt Cell Imaging Shared Resource staff, the Vanderbilt Mass Spectrometry Core staff, the Vanderbilt Technologies for Advanced Genomics staff, and the Vanderbilt Technologies for Advanced Genomics Analysis and Research Design staff.

I would like to acknowledge the funding that made this research possible. I was fortunate to be supported by the Vanderbilt Vision Research Center T32 training grant for three years. Along with the T32, my work was also supported by various grants obtained by Dr. Sappington

including those from the National Eye Institute, the Vanderbilt Vision Research Center, and Research to Prevent Blindness.

I want extend a big thank you to all the administrative staff at Vanderbilt that has been there to answer my questions and support me in so many ways, including Carolyn Berry from the IGP, Karen Gieg and Cindi Kellam from the Pharmacology Dept, and Angel Gaither, Jill Brott, and Susan Kelton from the VVRC/VEI. I would also like to thank some of the leadership from the IGP, Pharmacology graduate program, including Jim Patton, Roger Chalkley, Joey Barnett, Christine Konradi, and Sean Davies.

Finally, I want to thank my family for supporting me throughout the last five years of grad school, and my entire life. Their unwavering love and encouragement made this journey that much easier. I also want to acknowledge the many friends I made during my time in Nashville. I wouldn’t have made it through grad school without the love, support, and encouragement from my Nashville family.

TABLES OF CONTENTS

LIST OF FIGURES

CHAPTER 1

INTRODUCTION[1]

Glaucoma: Neurodegeneration of the optic nerve

Glaucoma is a leading cause of irreversible blindness worldwide and the second leading cause of blindness in the U.S. It is estimated that nearly 80 million people worldwide will suffer from glaucoma by the year 2020.[1] In the United States, glaucoma accounts for approximately 12% of all cases of blindness.[2] Vision loss during glaucoma results from degeneration of retinal ganglion cells (RGCs) and their axons, which form the optic nerve (**Figure 1.1**).[3] The two main risk factors for glaucoma are advanced age and elevated intraocular pressure (IOP). Elevated IOP is the primary modifiable risk factor and current target for therapeutics. Because RGC degeneration is progressive and irreversible, treatments aimed at lowering IOP slow, but do not halt, progression of the disease.[3] New therapeutic interventions that address the fundamental mechanisms of RGC degeneration are necessary to halt progression of the disease and preserve vision.

Clinical manifestations of glaucoma

Disease progression during glaucoma is monitored clinically through both functional and structural manifestations within the eye and optic nerve. For example, cupping of the optic disc is a visible, structural manifestation of damage to the optic nerve during glaucoma. The optic disc is the opening in the back of the eye through which RGC axons exit to form the optic nerve.

---

[1] Portions of this chapter were published as Fischer et al. (2019) American Journal of Physiology—Cell Physiology.

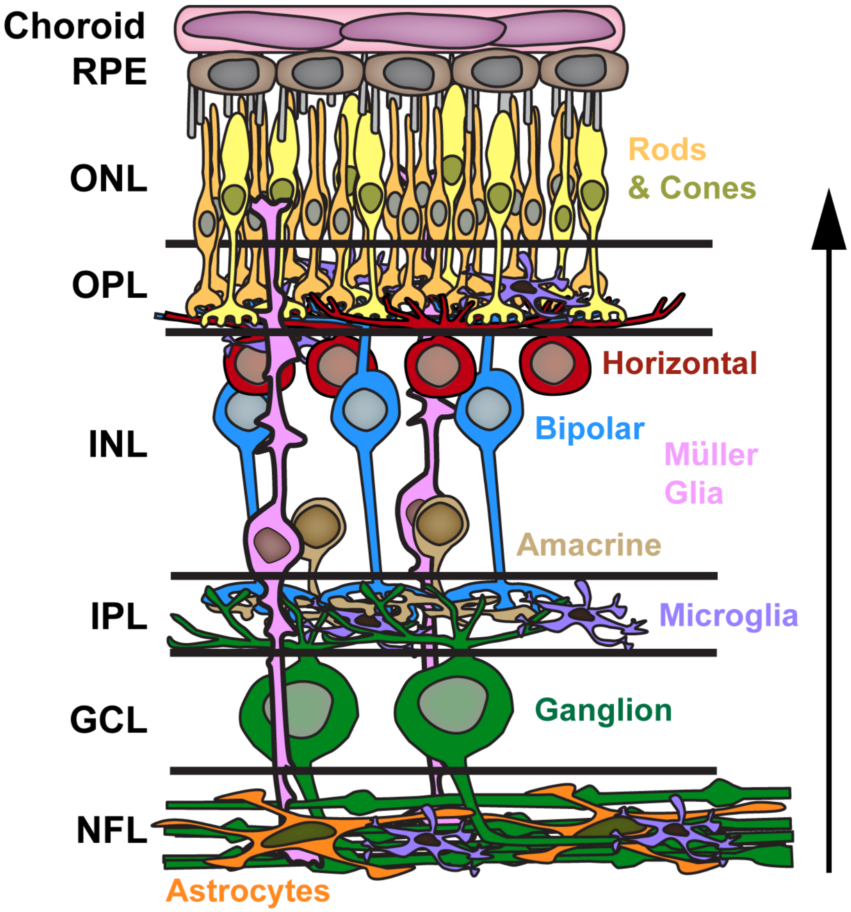

Figure 1.1. Cell types and circuitry of the retina. Light traverses through all the layers of the retina (arrow) to reach the photoreceptor cells located in the outer nuclear layer (ONL). Photoreceptors synapse directly onto bipolar cells in the outer plexiform layer (OPL). Horizontal cells in the inner nuclear layer (INL) modulate synaptic transmission between photoreceptor and bipolar cells. Bipolar cells synapse on RGCs in the inner plexiform layer (IPL), where amacrine cells are also located to modulate the synaptic transmission between bipolar cells and RGCs. RGC somas are located in the ganglion cell layer (GCL), while their axons are located in the nerve fiber layer (NFL). Müller glia, a retina-specific glial cell type, span the entire retina, from the ONL to the NFL. Astrocytes are located primarily in the NFL, while microglia are dispersed throughout the retina. (RPE = retinal pigment epithelium)
[Figure adapted from Calkins (2012) Prog Retin Eye Res[3] with permission from DJ Calkins and used in accordance with Copyright Clearance Center's RightsLink service.]

Progressive degeneration of RGC axons results in cupping of the optic disc. Optic disc cupping occurs when the center of the optic disc, known as the optic cup, becomes enlarged compared to the surrounding optic disc. Clinicians routinely measure the cup/disc (c/d) ratio as a measure of glaucoma progression using fundoscopy; an increase in c/d ratio correlates with severity of RGC loss (**Figure 1.2**). In addition to loss of nerve fibers, cupping results from compression or stretching of connective tissues surrounding the optic disc, in response to elevated IOP.[4] Another structural change that is visible to clinicians is thinning of the retinal nerve fiber layer (NFL). The NFL is where RGC axons are located in the retina (**Figure 1.1**). As RGC axons are lost during glaucoma, thinning of this layer can be visualized using optical coherence tomography (OCT).[5]

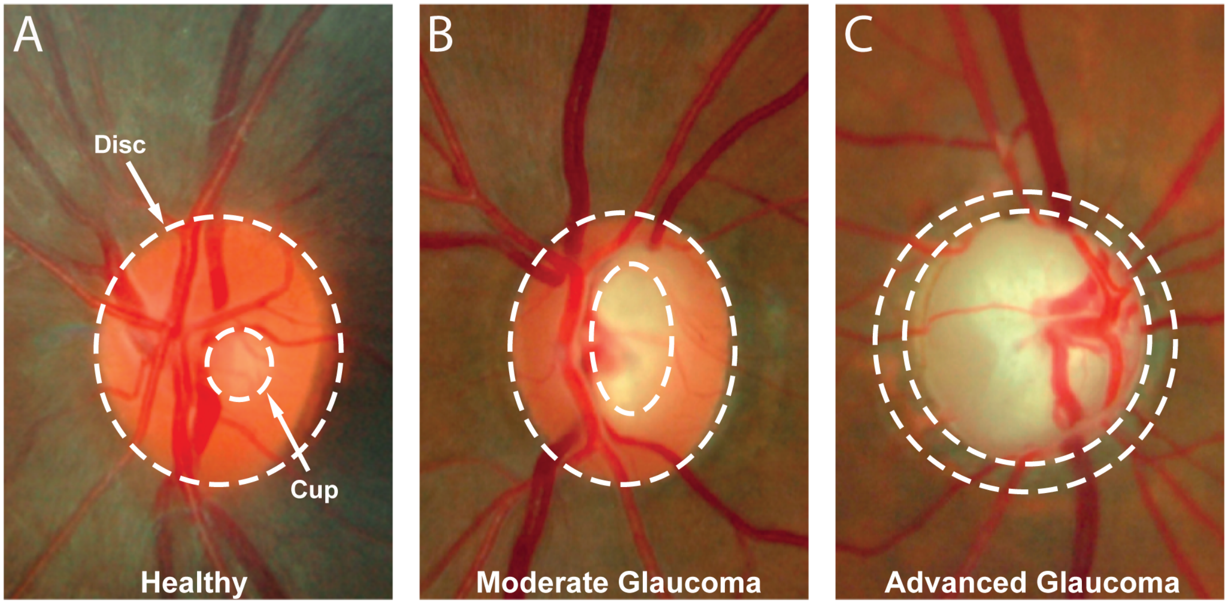

Figure 1.2. Progression of optic disc cupping in glaucoma. The optic disc is where RGC axons collect to exit the eye and form the optic nerve. **(A)** A fundus image of a healthy optic disc and optic cup (denoted with dotted lines and arrows). The optic cup-to-disc (c/d) ratio is 0.2. **(B)** In a patient with moderate glaucoma, the central cup gets larger and the c/d ratio increases to 0.7. **(C)** In a patient with advanced glaucoma, the central cup represents almost all of the optic disc area with c/d = 0.99. [Figure adapted from Bourne (2012) Comm Eye Health[6] and used in accordance with the Creative Commons Attribution-Non Commercial 4.0 International License.]

Functional attributes of glaucoma manifest as irreversible vision loss. Clinicians can measure an individual's visual field using a perimetry test. During this exam, a patient fixes their gaze while light flashes at specific locations across their visual field; the patient responds if they can see the light. Any area where the patient does not respond to the light flash represents a visual deficit.[7] Vision loss during glaucoma typically begins in the periphery and progresses into the central visual field. This often results in patients being unaware of a visual deficit until it progresses past their peripheral visual field.[7,8]

Glaucoma: Age-related sensitivity to ocular hypertension

The primary site of injury to the RGC during glaucoma is at the optic nerve head (ONH). The ONH is anatomically related to the optic disc. The optic disc is the anterior surface of the optic nerve head visible through fundoscopy.[3] The ONH is a biomechanical structure composed of astrocytes, vasculature, and extracellular matrix components.[3,9] The ONH serves as a transition point for RGC axons leaving the eye. Within the retina and ONH, the RGC axon is unmyelinated and becomes myelinated immediately proximal to the ONH.[3] The biomechanical force of intraocular pressure culminates at the ONH. The primary function of the ONH is to manage mechanical stress and strain through its load-bearing connective tissue in order to protect the optic nerve.[9] When IOP is elevated during glaucoma, the increase in biomechanical stress is transduced through the architectural (extracellular matrix), inflammatory (glial), and vascular factors of the ONH to the unmyelinated portion of the RGC axon, which is the segment of the axon most vulnerable to stress.[3] This initiates processes within the RGC axon that will eventually lead to degeneration and cell death.[3]

Sensitivity to ocular hypertension manifests as three different subtypes of glaucoma: open angle glaucoma (OAG), closed angle glaucoma (CAG), and normotensive glaucoma (NTG).[10-12] All three present with a similar clinical profile and will result in biomechanical strain on the ONH, but patients with OAG and CAG will have significantly elevated IOP or ocular hypertension.[3,10,12,13] IOP is maintained in the eye by the balance of aqueous humor production and drainage.[12] Aqueous humor is produced by the ciliary body and its two major outflow pathways are through the trabecular meshwork or the uveoscleral pathway (**Figure 1.3**).[10,12,14] Normal IOP values for humans are typically within the range of 15-21mmHg.[15,16] IOP values are elevated above 21mmHg during OAG and CAG, due to reduced drainage of aqueous humor. During OAG, there is increased resistance within the trabecular meshwork, which results in diminished outflow of aqueous humor (**Figure 1.3**).[10,12,17] During CAG, the iris covers the trabecular meshwork, creating an obstruction and blocking drainage of aqueous humor (**Figure 1.3**).[12,17,18]

Patients with NTG present with IOP values ≤ 21mmHg, however, still benefit from IOP lowering therapies.[12,13,19] This supports the hypothesis that the actual risk factor for glaucoma is sensitivity to IOP, rather than elevated IOP.[3] Patients with NTG still display clinical progression of pathology similar to OAG and CAG patients, which is further evidence for another major risk factor for glaucoma: age.[3] Individuals over the age of 55 have a 7-fold greater likelihood of developing glaucoma. In younger individuals, the structures within the ONH are more resilient and compliant, allowing them to more easily respond to pressure-induced stress or strain.[20] As one ages, there are significant changes that occur in the load-bearing tissues of the ONH, such as changes in expression and composition of extracellular matrix proteins.[9] During glaucoma, biomechanical stressors to the ONH are occurring in addition to age-related stressors that are already diminishing the ability of the ONH to manage IOP-related stress.[13] Thus, it is a combination of aging and sensitivity to IOP that are the main risk factors for developing glaucoma.[3,13]

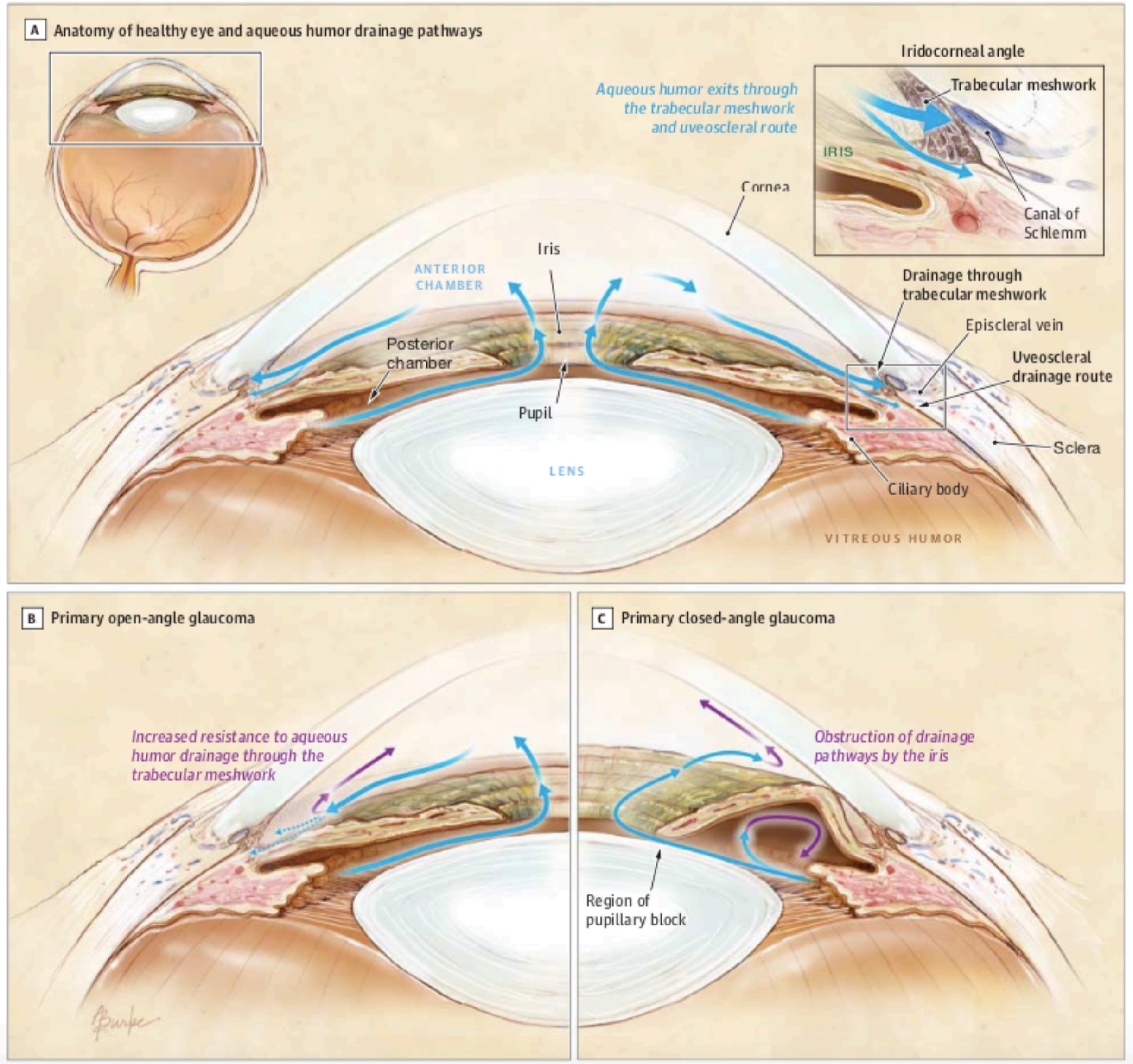

Figure 1.3. Aqueous humor dynamics in the healthy and glaucomatous eye. (A) Aqueous humor is secreted by the ciliary body. It flows into the anterior portion of the eye where it then drains through the trabecular meshwork or through the uveoscleral outflow pathway. The balance between aqueous humor production and drainage determines the IOP of the eye. **(B)** In OAG, there is increased resistance to aqueous outflow through the trabecular meshwork, resulting in elevated IOP. **(C)** In CAG, the iris collapses and creates an obstruction to the aqueous humor drainage pathways, resulting in elevated IOP. [Figure from Weinreb et al. (2014) JAMA[12] and used in accordance with Copyright Clearance Center's RightsLink service.]

Animal models of glaucoma

Animal models of glaucoma have been invaluable in providing key insights to the progression and potential treatment of glaucoma pathology. While not all patients who suffer from glaucoma experience elevated IOP, it is still the most commonly used method to reproduce clinical features of glaucoma in animal models. The two most commonly used models of glaucoma are the Microbead Occlusion Model (MOM)[16] and the DBA/2J transgenic mouse[21-23], both of which utilize IOP elevations to model glaucoma.

Many glaucoma models artificially elevate IOP as a means to recapitulate glaucoma pathology.[24,25] While artificial IOP elevation will typically only produce a short-term IOP elevation (≤ 8 weeks), it does have the advantage that IOP can be elevated in animals of any age or with any genetic background. One method for artificial IOP elevation is through occlusion of the trabecular meshwork. This is often done by translimbal laser photocoagulation of the trabecular meshwork[26], or injection of polystyrene[16] or magnetic microbeads[27], which cluster at the irdocorneal angle and block drainage of the aqueous humor. Another method is to impede drainage of the aqueous humor into the vasculature. This is accomplished by occlusion of veins in the eye that are critical for the aqueous humor outflow pathways through ophthalmic catery[28], injection of hypertonic saline[29], or photocoagulation[30]. These methods reliably result in elevation of IOP and subsequent loss of RGCs. However, these measures of glaucoma progression are not equivalent across all models and can differ as a result of the duration and magnitude of IOP elevation.

An important factor for finding an ideal animal model of glaucoma is to find a degree of IOP elevation and RGC loss that mimics that seen in human patients. As such, MOM has become the method of choice to model acute, inducible ocular hypertension.[16,27,31-33] The MOM model involves injection of polystyrene microbeads into the anterior chamber of the rodent eye; control eyes receive an equivalent injection of saline. Microbeads will eventually migrate to the irdocorneal angle and obstruct aqueous humor outflow through the trabecular meshwork.

Microbead injection produces a modest ~30% IOP elevation. This closely resembles IOP values in human patients with untreated mild to moderate ocular hypertension, who on average display an approximately 38% increase in IOP.[16] Animals also recover well from the minimal surgery required for microbead injection, compared to more invasive surgery required with other inducible models.[34,35]

For models resulting in long-term, age-related IOP elevation, the DBA/2J transgenic mouse is most commonly used.[21] DBA/2J mice suffer from iris pigment dispersion due to a premature stop codon mutation in the *Gpnmb* gene and iris stromal atrophy due to a recessive *Tryp1b* gene mutant allele.[21] These mutations cause iris pigment and cellular debris to obscure aqueous humor drainage pathways and result in IOP elevation.[22,36] This most closely models CAG and exfoliation glaucoma.[12,37] The DBA/2J model closely resembles the human condition as IOP elevation occurs as the mice age. Young DBA/2J mice (~2mo) display IOP values of 15-16mmHg, while DBA/2J mice over the age of 10mo have IOP values of 22-23mmHg.[38] However, there is large variability with the DBA/2J model in the onset and magnitude of IOP elevation. This variability however is similar to the variability within the human population suffering from glaucoma and the levels of RGC axon loss appear to correlate with magnitude of IOP elevation.[3,38]

Axonopathy: Temporal progression of glaucoma pathology

RGC degeneration begins in the axon and occurs in a temporal sequence of events that is common to several neurodegenerative diseases, such as Alzheimer's disease, Parkinson's disease, and amyotrophic lateral sclerosis.[3,39-45] This common path to degeneration, termed axonopathy, is associated with functional deficits in axon transport, that precede structural degeneration of the axon.[3] RGC degeneration begins in the axon terminals and progresses in a retrograde fashion towards the soma.[3] Later stages of degeneration include dendritic pruning and synapse elimination at the soma, followed by apoptotic death.[13,46-49] The period of time between onset of functional deficits and the physical degeneration of RGCs represents a potential therapeutic window to interrupt axonopathy prior to irreversible, structural loss. Thus, there is a fundamental need to identify cellular mechanisms that underlie the transition from functional to structural loss.

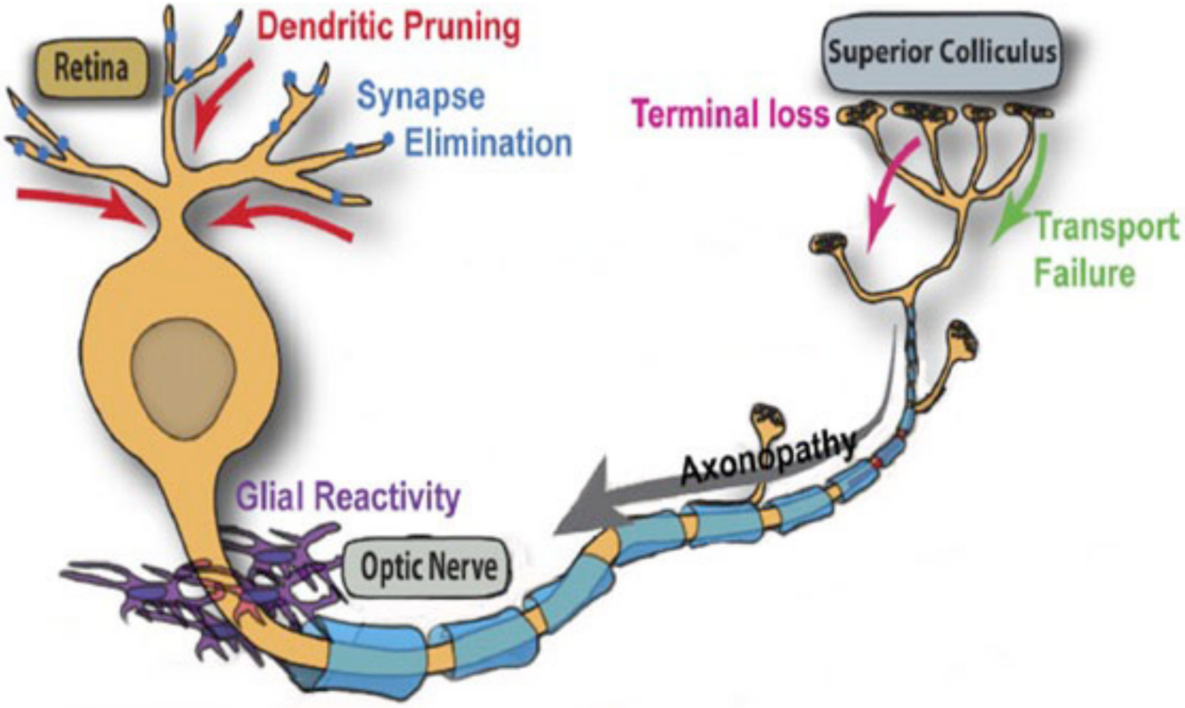

Figure 1.4. Critical events in RGC degeneration during glaucoma. Axonopathy in glaucoma begins with functional deficits in axon transport. Transport deficits are followed by structural degeneration that begins in axon terminals and progresses in a retrograde fashion towards the soma. Later stages of degeneration include dendritic pruning and synapse elimination at the soma, followed by apoptotic death. Glial reactivity and inflammation in the retina and the optic nerve head also accompany RGC degeneration.
[Figure adapted from Crish and Calkins (2011) Neuroscience[13] with permission from DJ Calkins and used in accordance with Copyright Clearance Center’s RightsLink service.]

Deficits in axon transport

One of the earliest features of axonopathy is deficits in axon transport, occurring prior to physical degeneration of the axon (**Figure 1.4**).[50] Axon transport is the cellular process responsible for active movement of vesicles, mitochondria, RNA, and proteins from the cell soma through the cytoplasm of the axon. Movement away from the soma towards the distal end of the axon is called anterograde transport, while movement from the distal end of the axon back proximal to the soma is called retrograde transport.[51] Axon transport in neurons occurs primarily along microtubules. Molecular motor proteins, kinesin and dynein, are responsible for driving axon transport. Anterograde transport is kinesin-driven, while retrograde transport is dynein-driven.[51] Functional axon transport is critical for delivery of growth factors, such as nerve growth factor or brain-derived neurotrophic factor, along the axon.[3,52] New protein complexes, organelles, or mitochondria that are synthesized in the cell soma must be transported down the axon by anterograde transport.[53] Maintaining functional axon transport is critical for the health of the axon and continuance of biological processes.

Axon transport deficits can be measured experimentally through the use of neural tracers. Anterograde transport can be measured using the neural tracer, cholera toxin beta subunit (CTB). In the DBA/2J mouse, moderate loss of CTB transport from the retina to the superior colliculus in the brain (SC; primary terminus of RGCs in rodents) is seen by as early as 3 months of age, with severe CTB transport deficits seen by 11-12 months of age.[3,50] Subsequently, the neural tracer, FluoroGold, can be used to measure retrograde axon transport. Decreases in the retrograde transport of FluoroGold first occur in DBA/2J mice around 6-8 months of age. More significant deficits in FluoroGold transport begin around 13 months, but labeling can persist until up to 18 months.[3,54] Therefore, during glaucoma, the onset of retrograde transport deficits is slower than anterograde transport deficits in RGCs and the ability to perform retrograde transport persists longer than anterograde transport. The difference in motor proteins utilized to perform anterograde and retrograde transport may provide a possible mechanism for why anterograde transport is challenged earlier in glaucoma pathology. As stated previously, kinesin drives anterograde transport, while dynein drives retrograde transport.[51] Both kinesin and dynein hydrolyze ATP in order to "walk" along microtubules.[40] However, kinesin only has one ATP hydrolysis site, allowing for a step size of 8 nm, while dynein has four ATP hydrolysis sites and a step size of up to 32 nm.[3] Dynein is therefore four times more efficient at consuming ATP than kinesin, which makes kinesin-driven anterograde transport more vulnerable during glaucoma when ATP stores along the axon become diminished.[3]

Deficits in axon transport are not occurring simply due to the degeneration of axons, as there is evidence that RGC axons are still intact during the timeframe that axon deficits are seen.[54] Between 3-10 months of age in DBA/2J mice, when significant deficits in CTB transport to the SC are seen, there is intact labeling of RGC terminals and synaptic markers within the SC and intact RGC axons within the optic nerve.[50] In other neurodegenerative diseases, disruptions in axon transport are due to mutations in motor proteins, cytoskeletal proteins, and other associated proteins.[39] This would suggest there could be a potential role for altered cytoskeletal proteins during glaucoma. The three primary cytoskeletal proteins are microtubules, actin, and intermediate filaments. Axon transport in neurons is primarily dependent on microtubule networks.[51] Neurofilaments, the main intermediate filament in neurons, are transported along the axon to help stabilize microtubule structure.[39] Microtubule-associated proteins (MAPs), such as tau, are bound to the microtubules along the length of the axon to promote microtubule polymerization and stabilization.[51] Studies by Wilson *et al.* found that elevations in phosphorylated neurofilament-heavy chain are seen in the optic nerve of 8-10 month old DBA/2J mice, which correlates with axon transport deficits.[55] Hyperphosphorylated tau (ptau) is elevated in the optic nerve of DBA/2J mice between 3-8 months. Ptau is suggested to have an increased affinity to the motor complex protein dynactin, involved in retrograde axon transport.[55] Finally, β-tubulin levels are decreased in the optic nerve of 10-12 month old DBA/2J mice, which could lead to destabilization of microtubules.[55] These studies suggest that modification of cytoskeletal proteins occur during glaucoma, prior to loss of functional axon transport and physical axon degeneration.

Structural axon degeneration

Structural degeneration of the axon begins to occur following the functional insults to the RGC axon described in the previous section (**Figure 1.4**). Axon degeneration during glaucoma is characterized by a decrease in both the axon density and total number of axons in the optic nerve.[3] The overall volume of the nerve is maintained by remodeling of astrocyte processes to expand and fill the spaces left by axon dropout, forming a glial scar.[3,56]

In the DBA/2J mouse model of glaucoma, axon loss, reported as both reductions in axon density and total number of axons, is seen between 10-13 months of age.[38] However, there appears to be a strong correlation between the degree of IOP elevation and amount of axon loss. It was found that a young, 4 month old DBA/2J mouse already showing a high IOP elevation can exhibit the same level of axon loss as a 10 month old DBA/2J mouse.[38] The effect of degree of IOP elevation on axon loss is also prevalent in inducible models of glaucoma. Several microbead studies in rodents with moderate IOP elevation of ~30% for 4-5 weeks report significant reductions in both axon density and number of axons by ~15-25%.[16,33] Other inducible models utilizing a larger IOP elevation of up to 90% report larger axon losses, between 30-50%.[57,58] A meta-analysis of inducible glaucoma models found that increasing IOP levels correlates with increases in axon degeneration, further confirming the link between IOP elevation and axon loss.[3]

Axon degeneration in the central nervous system (CNS) occurs through two primary mechanisms: "dying back" and Wallerian degeneration.[59-64] There is evidence for both mechanisms occurring during glaucoma, depending on which model of glaucoma is being utilized.[3] "Dying back" refers to distal to proximal degeneration, where axon degeneration begins at the axon terminals (distal end) and progress slowly towards the soma (proximal to eye).[59-61] In DBA/2J mice, histological analysis of DiI labeling showed a higher density of axons proximal to the globe, compared to the distal end.[65] A larger amount of degenerating axon profiles were also found in distal optic nerve sections, compared to proximal in aged DBA/2J mice (13 months).[50] In addition, axon transport deficits appear to progress in a distal to proximal fashion. CTB labeling in DBA/2J mice shows that transport loss first occurs in the SC, the most distal site for RGC axons, then progresses to more anterior brain targets, such as the lateral geniculate nucleus, followed by the optic tract, optic nerve, and finally the retina.[50]

In contrast, Wallerian degeneration refers to a form of degeneration that occurs following an injury, such as axotomy, wherein the axon distal to the injury will degenerate in a proximal to distal fashion.[62-64] As stated previously, the primary site of injury to the RGC during glaucoma is at the ONH.[3] Indeed, several studies show that early stages of glaucoma pathology begin at the ONH. Large elevations in IOP (100% for 2 weeks) have been shown to produce significantly greater reductions in axon loss in proximal portions of the optic nerve, relative to distal portions.[66] Therefore, an acute, large IOP elevation could potentially produce an axotomy-like injury at the ONH, which leads to proximal to distal RGC axon degeneration.[13]

Independent of the mechanisms of axon degeneration, it has been widely shown that degeneration of the RGC axon occurs prior to loss of the cell soma.[3] In DBA/2J mice, significant reductions in the density of RGC somas in the retina are not seen until 18-21 months of age[54], much later in life than reported axon loss, which is seen between 10-13 months of age.[38] Across several inducible models, regardless of the degree of IOP elevation, RGC axon loss is 2-3 times greater than soma loss.[3] Finally, when the functional capacity of the RGC soma and axon terminals was measured using electroretinography and visual evoked potentials, respectively, it was found that while there is a complete loss of signal from the RGC axon, there is a diminished, but still present, signal from the RGC soma in significantly aged DBA/2J mice.[67]

Synapse elimination and dendritic pruning

Dendrites are projections extending from the soma of neurons that receive electrochemical information via synaptic connections with other neurons. In the retina, RGC dendrites form synaptic connections with bipolar and amacrine cells (**Figure 1.1**). In glaucoma, synapse elimination, which leads to dendritic remodeling and eventual loss, occurs prior to loss of the cell soma (**Figure 1.4**).[3] One hypothesis for the process of synapse elimination during glaucoma involves the classical complement cascade, a component of the innate immune system, during which cellular material is targeted for phagocytosis and elimination by microglia.[49] C1q, the initiating protein of this cascade, is expressed during early stages of glaucoma in the DBA/2J mouse, where it becomes localized to synapses prior to either synapse elimination or RGC cell death. As glaucoma progresses in the DBA/2J mouse (10-11 months), C1q becomes upregulated in the retina at the same time that levels of the synaptic marker, PSD-95, decrease.[49] This indicates a role for the complement cascade in synapse elimination during glaucoma. Furthermore, genetic knockout of *C1qa* in DBA/2J mice or treatment with a pharmacological inhibitor of C1q in MOM mice prevented pressure-induced synapse elimination.[68]

Following synapse elimination, RGC dendrites lose complexity, coverage, and eventually degenerate. In DBA/2J mice, there is decreased complexity, remodeling, and shrinkage of RGC dendritic arbors by 11-12 months of age.[48,69] Changes in the dendritic arbor of RGCs has also been examined in various inducible models of glaucoma in primates[70], cats[71], and rodents[69]. It was found that elevated IOP leads to decreases in complexity of dendritic branching, dendritic field radius, and the length and number of dendritic branches.[69-71]

Several studies show that different subtypes of RGCs are more vulnerable to dendritic remodeling and degeneration. Chronic elevation of IOP in rhesus monkeys results in decreased dendritic field size in parasol cells, but not midget cells.[70] In cats with experimental glaucoma, dendritic arbor shrinkage was more pronounced in αRGCs, than in βRGCs.[71] In mice with microbead-induced IOP elevation for 7 days, OFF-transient RGCs displayed dendritic shrinkage and remodeling of dendritic arbors.[46] Consistent with these findings, Della Santina *et al.* found that OFF-transient RGCs displayed reduced size and complexity of dendritic arbor after 4 weeks of microbead-induced IOP elevation, compared to ON-sustained and OFF-sustained RGCs.[32] In contrast to these studies, others have found ON-RGCs to have greater susceptibility to IOP-related changes in dendritic remodeling. Feng *et al.* found significantly reduced dendritic field size and soma size in ON-RGCs, compared to ON-OFF RGCs, in mice with inducible glaucoma that results in large IOP increases (>100%).[72] In addition, 2 weeks of microbead-induced IOP elevation was shown to decrease dendritic arbor complexity, dendritic field size, and dendrite length in αON-sustained RGCs and dendrites of ON-OFF RGCs that stratify in the ON sublamina.[47] While additional studies are needed to elucidate the effect on specific subtypes of RGC, it is clear that IOP elevation has a significant effect on remodeling of dendritic arbors of RGCs.

RGC apoptosis

The last step in RGC axonopathy, following functional deficits, structural axon degeneration, synapse elimination, and dendritic pruning, is cell death of the RGC soma (**Figure 1.4**).[3] In DBA/2J mice, RGC loss, as measured by neuronal-specific nuclear protein (NeuN) immunohistochemistry, is not seen until mice are 18 months of age; very late in the pathological timeline.[54] In certain acute, inducible models, RGC loss can be seen as early as one week following IOP elevation. However, inducible models consistently show significantly less RGC soma loss, compared to axon loss, indicating that the soma is surviving later in the pathological timeline, even after the axon has begun to degenerate.[3]

Cell death primarily occurs through two mechanisms: apoptosis or necrosis. Necrosis is caused by an external factor, such as a toxin or trauma to the cell, and results in cell membrane rupture and release of cellular contents, which can be damaging to surrounding cells. Apoptosis, or programmed cell death, is a controlled sequence of events wherein the cellular contents are broken down within the plasma membrane in “apoptotic bodies”.[73] The apoptotic process in mammalian cells can be initiated either extrinsically or intrinsically.[73]

The extrinsic apoptosis pathway is also known as the death receptor pathway. It is initiated by binding of the ligands, Fas or tumor necrosis factor (TNF), to their respective receptors.[74,75] Activation of the death receptors (Fas receptor or TNFR) results in activation of a series of caspases that eventually digest the cellular contents and cause destruction of the cell.[73,76,77] Many studies show involvement of the extrinsic apoptosis pathway in RGC loss during glaucoma. IOP elevation and associated RGC loss has been shown to occur alongside increased Fas[78], and TNF-α signaling[79]. Genetic deletion of TNF-α or TNF-α neutralizing antibodies have been shown to block these apoptotic events.[79] Finally, there are increased expression levels of caspase-3 and caspase-8 in glaucomatous eyes.[73,78,80,81]

The intrinsic apoptosis pathway involves factors inside the cell, such as oxidative stress or deprivation of neurotrophins, activating the cell death process, rather than receptor-mediated signaling. These intrinsic apoptotic factors cause release of cytochrome c from the mitochondrial intermembrane space to the cytoplasm.[82] Cytochrome c release is mediated by the Bcl-2 family of proteins located on the outer mitochondrial membrane. Of this family, Bax, Bid, and Bad are pro-apoptotic and promote cytochrome c release, while Bcl-2 and Bcl-xL are anti-apoptotic and inhibit cytochrome c release.[83] After it is released into the cytoplasm, cytochrome c forms the apoptosome by binding to Apaf-1 and procaspase-9.[84-86] The apoptosome triggers activation of the same series of caspases as in the extrinsic pathway.[73,77,85] The intrinsic apoptosis pathway is also implicated in glaucoma; it has been reported that IOP elevation causes cytochrome c release.[80] In addition, Bax deficiency has been shown to be protective against RGC loss in DBA/2J mice; Bax-deficient DBA/2J mice with severe axon loss (95%) show normal, healthy numbers of RGC somas in the retina.[87] Finally, IOP elevation results in upregulation of procaspase-9 and caspase-9 expression in the retina.[73]

Shared pathological timeline among neurodegenerative diseases

The temporal sequence of events leading to the degenerative events described above is common to several neurodegenerative diseases, such as Alzheimer's disease, Lewy body dementia, multiple system atrophy, Charcot-Marie-Tooth disease, and amyotrophic lateral sclerosis (ALS).[3,39-45] Many of these diseases share similar pathological features to glaucoma; such as deficits in axon transport, synapse elimination, dendritic pruning, and apoptosis.

Disrupted axon transport is an early feature of pathology and possibly even a causative event in many neurodegenerative diseases, including Alzheimer's disease, Parkinson's disease, and ALS.[39-41] Loss of functional axon transport can disrupt many cellular processes. For example, anterograde axon transport is needed for protein and lipid delivery to synapses and transport of mitochondria for local energy requirements, while retrograde axon transport is critical for clearing misfolded or aggregated proteins.[41] Mutations in the motor proteins that drive microtubule-based axon transport are implicated in Alzheimer's disease, Huntington's disease, Parkinson's disease, ALS and Charcot-Marie-Tooth disease.[42,53] In addition, decreased transport of mitochondria to the distal portions of axons has been reported in Alzheimer's disease and other neurodegenerative diseases.[3,53]

The next steps in axonopathy following axon transport deficits and axon degeneration, is synapse elimination and dendritic pruning. There is evidence for this occurring across many neurodegenerative diseases. Synaptic dysfunction and reduced synaptic density is reported as one of the early stages of Alzheimer's disease pathology.[88-91] Patients showing early clinical and neuropathological features of Alzheimer's disease showed a 20% loss in synapses in the hippocampus.[90] In conjunction with synapse elimination, studies have found dendritic arbor regression, and dysfunction and loss of dendritic spines in Alzheimer's disease.[89] In fact, the amount of synapse loss and dendritic arbor loss in Alzheimer’s disease correlates with severity of dementia and degree of cognitive and memory impairment.[88-90] One hypothesis for synapse loss in Alzheimer’s disease is soluble amyloid beta protein binding directly to dendritic spines, which promotes spine destabilization and synapse loss.[89] Another hypothesis suggests that aggregates of cofilin protein disrupt the microtubule network and prevent nutrient and protein delivery along neurites, effectively “choking off” the synapse.[89] In patients with Huntington’s disease, there is evidence for decreased molecular composition, size, and density of synapses.[91] In addition, weakening of synapses, structural abnormalities and eventual synapse loss have all been reported in patients with ALS.[91] As with Alzheimer’s disease, impaired dendritic protein transport is also implicated in Huntington’s disease.[88]

Apoptotic cell death has been reported as the end stage of pathology in many neurodegenerative diseases. Neuronal apoptosis has been implicated in the following cell populations and diseases: hippocampal and cortical neurons in Alzheimer’s disease, midbrain dopamine neurons in Parkinson’s disease, striatal neurons in Huntington’s disease, lower motor neurons in ALS, and neurons in various locations in the CNS in traumatic brain and spinal cord injury and stroke.[92,93] Several studies show that the caspase family of proteins plays a key role in apoptotic cell death in Alzheimer’s disease, Huntington’s disease, Parkinson’s disease, ALS, and dementia associated with HIV.[92] These numerous examples demonstrate the many pathological features of axon degeneration that are shared between glaucoma and other neurodegenerative disorders.

Sectorial degeneration: Spatial progression of glaucoma pathology

Studies by others and us in animal models indicate that RGC axonopathy and subsequent RGC loss does not occur in a uniform manner across the retina, but tends to occur simultaneously in clusters of neighboring RGCs.[50,65,94-96] This topographic degeneration of RGCs is consistent with patterned vision loss in glaucoma patients and suggests that external cues in the immediate milieu may play an important role in disease progression.[97-100] It is critically important for understanding glaucoma pathology to identify extracellular events that could underlie the spatiotemporal progression from functional deficits to structural RGC degeneration.

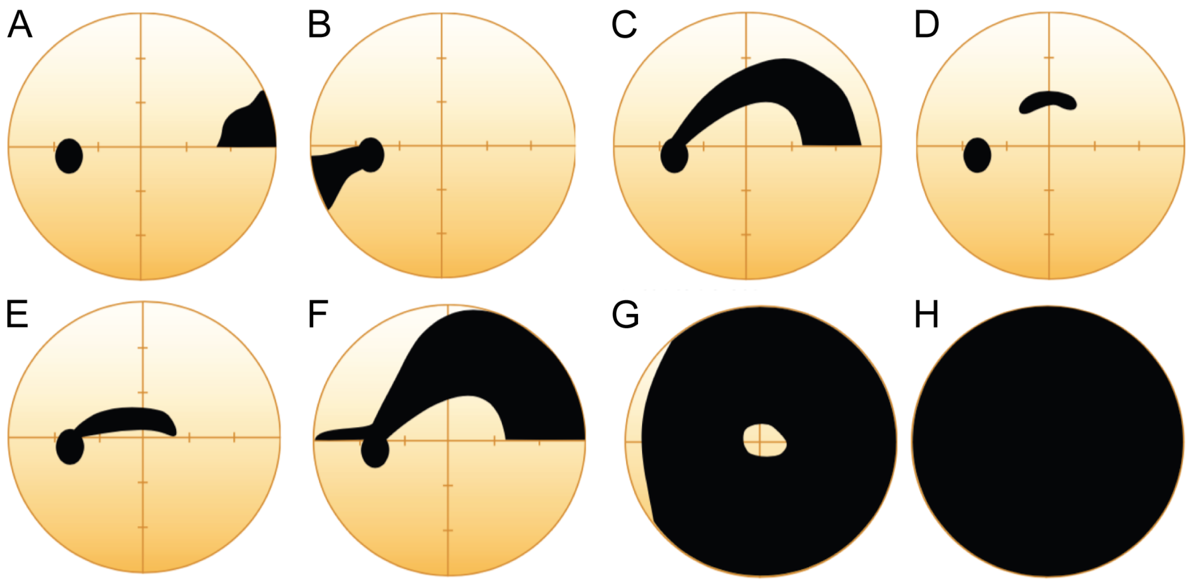

Figure 1.5. Glaucomatous field defects in human patients. Representations of visual field maps collected using standard perimetry from glaucoma patients (left eye only) with varying degrees of vision loss. Dark areas correspond to areas of decreased visual sensitivity. **A-H** are various examples of glaucomatous visual field defects. (**A**) A nasal step defect obeying the horizontal meridian. (**B**) A temporal wedge defect. (**C**) The classic arcuate defect, which is a comma-shaped extension of the blind spot. (**D**) A paracentral defect 10-20 degrees from the blind spot. (**E**) A superior, fixation-threatening paracentral defect. (**F**) An arcuate defect with peripheral breakthrough. (**G**) Tunnel vision defect with temporal crescent sparing. (**H**) End stage, complete field loss.
[Figure adapted from Broadway (2012) Comm Eye Health[101] and used in accordance with the Creative Commons Attribution-Non Commercial 4.0 International License.]

Vision loss: scotomas

In glaucoma, the most frequent, early visual field defects are circumscribed, paracentral scotomas in the central 30 degrees of the visual field (**Figure 1.5**).[100] Scotomas are defined as an area of the visual field with diminished or completely degraded visual acuity, surrounded by intact, normal vision. Paracentral scotomas are located around the central 10 degrees of the visual field.[100] Examples of several types of visual field defects during glaucoma are shown in **Figure 1.5**. Several studies have been done on patients with OAG to track the progressive changes to their visual field, specifically the changes to scotomas. Depending on the study, 24-79% show increases in scotoma depth, 14-52% show development of new scotomas, and 7-50% show enlargement of the scotoma.[98,99] During glaucoma, the rate of visual field loss significantly correlates with the size and number of scotomas. This suggests that axons within the optic nerve can slowly be lost in early stages of glaucoma without a significant change in the visual field. There appears to be a critical point of axon loss at which point defects in visual function finally manifest.[99] Several studies have been performed to correlate visual field defects with the amount of RGC loss. The consensus across studies is that visual field defects begin to occur when RGC loss exceeds 25-30%.[102,103] This demonstrates that if there is vision loss, significant damage to the optic nerve has already occurred.

Visual function is often measured experimentally in rodents using the optokinetic reflex test. This test measures the animal's innate response to track a moving stimuli, wherein eye movement will track with the direction of the stimulus. This test will measure the overall visual acuity, as well as contrast sensitivity thresholds.[104,105] Deficits in optokinetic reflex can also be seen in glaucoma patients, however it is not the most commonly used clinical assessment of visual function.[106] In microbead-injected mice, IOP elevation resulted in significantly impaired visual acuity after only 3 days, which persisted to 30 days post-injection, compared to controls. The reduced visual acuity in these mice was associated with a 43% reduction in Brn3a+ RGCs.[32] Another study utilizing laser photocoagulation alongside microbead injection to elevate IOP for 2 months in mice showed reduced visual acuity associated with a 17% reduction in Brn3a+ RGCs and 18% reduction in Brn3b+ RGCs, compared to controls.[107] Altered visual function is also seen in DBA/2J mice. DBA/2J mice begin to show significantly reduced visual acuity by 7-8 months of age, compared to younger DBA/2J mice and age-matched WT controls.[108,109] Progressive decreases in visual acuity occur between 9-11 months and by 12-14 months DBA/2J mice could not detect the visual stimulus at all, indicating that visual dysfunction progresses with age in DBA/2J mice.[109] Rangarajan *et al.* additionally show that age and the degree of IOP elevation in DBA/2J mice alone are not a good indicator of visual function. Rather the amount of RGC loss is a better predictor of visual performance, with significant RGC loss by 6-8 months and severe RGC loss by 12-16 months.[109]

Topographic RGC degeneration

As outlined in the previous sections, several studies in animal models of glaucoma have revealed significant deficits in the uptake and transport of neural tracers by RGCs following exposure to elevated IOP.[13,50,94,110,111] These deficits in axon transport result in decreased connectivity between RGCs and their post-synaptic targets.[13,50,94,110,111] Interestingly, these deficits in axon transport do not occur uniformly throughout the retina. Rather, deficits occur in clusters of neighboring RGCs, such that there are areas of intact and deficient transport within a single glaucomatous retina. In DBA/2J mice, RGC degeneration in the retina occurs in a sectorial pattern.[112] RGC loss in the retina appears in pie-shaped sectors that extend from the optic disc to

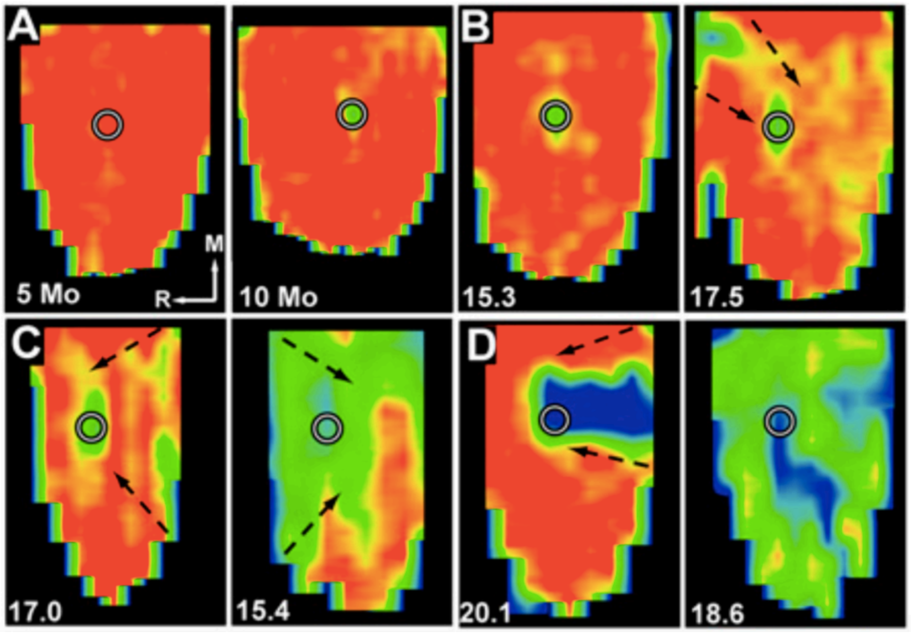

Figure 1.6. Sectorial transport deficits. (A) Maps of CTB transport to the SC in 5 and 10 month old WT mice (C57/Bl6). Optic disc gap is indicated as a circle and rostral (R) and medial (M) are noted. Maps of CTB transport to the SC in DBA/2J mice at 3 months **(B)**, 5 months **(C)**, and 8 months old **(D)** with deficits progressing from rostral or caudal edge to the optic disc gap (denoted with arrows). IOP in mmHg is indicated.
[Figure adapted from Crish et al. (2010) PNAS[50] and used in accordance with the Creative Commons Attribution-Non Commercial 4.0 International License.]

the periphery of the retina.[48,65] Additionally, histological staining of axons in the optic nerve shows clusters of degenerating axons in DBA/2J mice.[65] 5-8 month old DBA/2J mice show sectorial loss of CTB transport to the SC (**Figure 1.6**).[50] RGC inputs to the SC maintain retinotopic organization, meaning the SC contains a complete topographic representation of the retina. Therefore, deficits in CTB transport to the SC also occur in pie-shaped sectors (**Figure 1.6, panels C and D**). This is consistent with sectorial vision loss in glaucoma patients, which begins in the periphery and extends towards the central retina.[50] Translimbal laser photocoagulation in rats resulted in sectorial degeneration similar to that seen in DBA/2J mice. RGC loss in this model also occurred in pie-shaped sectors of the retina, as measured by FluoroGold labeling. Within a single laser-induced glaucoma retina, there were sectors of mild and severe RGC degeneration.[95] In addition to changes seen in RGCs, astrocyte reactivity is a key feature of glaucoma pathology in the retina and optic nerve. It has been shown that astrocyte reactivity in DBA/2J glaucomatous retina occurs in microdomains. These microdomains of astrocytes are also biomarkers for functional decline in RGCs.[94]

Clusters of pathology in other neurodegenerative diseases

Spatial patterning of pathological lesions is characteristic of many neurodegenerative diseases, including Alzheimer's disease, Lewy body dementia, Pick's disease, and corticobasal degeneration.[113,114] Brain lesions in these diseases vary in morphology and molecular composition and can include extracellular protein deposits, intracellular inclusions, and changes in the morphology of individual neurons (i.e. swelling). For example, Parkinson's disease is caused by the development of intraneuronal inclusions, called Lewy bodies. Lewy bodies mainly consist of aggregates of misfolded α-synuclein protein.[43] Formation of Lewy bodies and expansion of the pathology throughout the brain occurs in a predictable, topographic manner.[43]

Despite the differences in molecular composition of brain lesions across neurodegenerative diseases, they often exhibit similar spatial patterns, forming clusters, which implies shared pathological mechanisms.[114] One such mechanism is hypothesized to be the cell-to-cell transfer of pathogenic proteins, which would result in spreading of neurodegeneration through a pathological influence on neighboring neurons.[113] Cell death processes in one cell can affect the health and viability of neighboring cells. If neighboring cells are exposed to factors produced by the dying cells, this could trigger a similar process in the healthy cells.[92] This hypothesis of "contagious apoptosis" is illustrated in **Figure 1.7**.[92] For example, during a stroke, a neuron receives an ischemic insult, triggering an apoptotic cascade, involving release of interleukin-1β, TNF-α, and reactive oxygen species (ROS). These factors then initiate apoptotic cascades in neighboring cells that have received a similar, but smaller ischemic insult. Thus, cells that might not have died from the sublethal ischemia alone, will now die due to the diffusible toxic factors produced by dying, neighboring cells (**Figure 1.7**).[92] A similar process also occurs during ALS caused by mutant SOD1 protein, which initiates an apoptotic cascade in motor neurons. As these neurons are dying, they release proapoptotic factors that target neighboring cells. Since the neighboring cells also contain mutant SOD1 protein, they are predisposed to initiation of a similar cell-death cascade.[92]

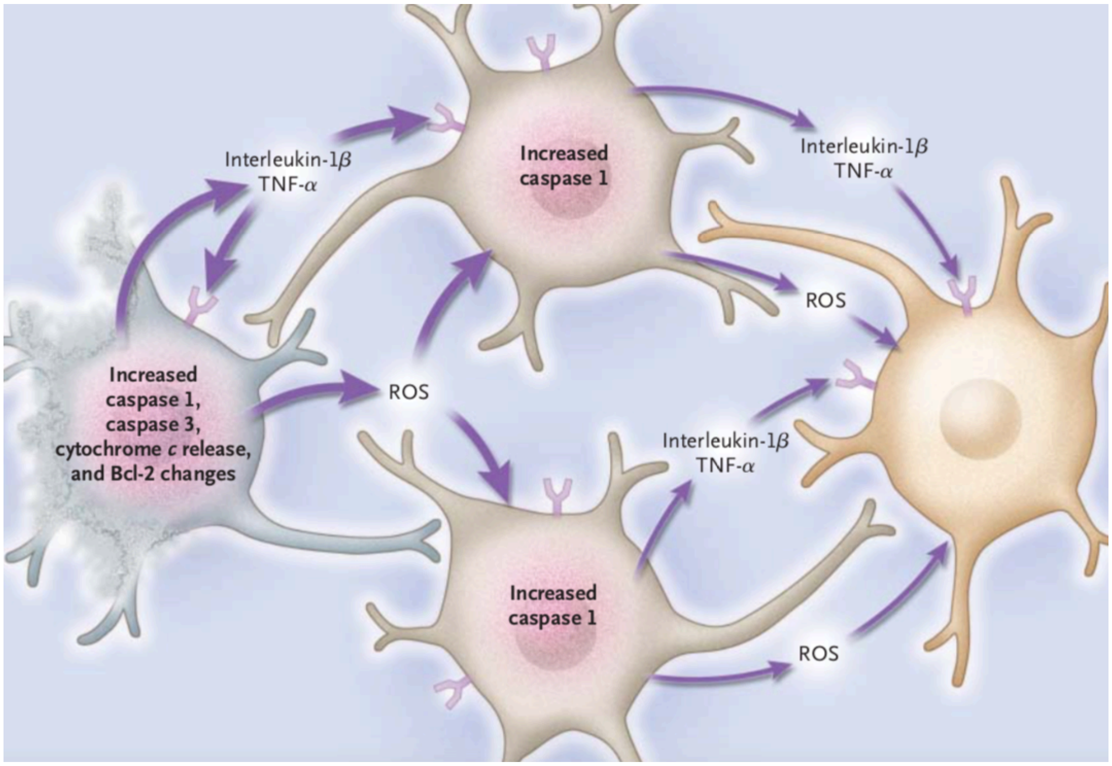

Figure 1.7. Contagious apoptosis. Following an ischemic event, a neuron (gray, left) undergoes apoptosis, cascades are activated, and toxic factors (interleukin-1β, TNF-α, and ROS) are released. These toxic factors induce neighboring cells (tan, center) to enter an apoptotic cascade, initially resulting in up-regulation of caspase 1. Eventually these neurons will begin to secrete the same toxic factors, which will, in turn, affect the surrounding healthy neurons (pink, right).
[Reproduced with permission from Friedlander (2003) NEJM[92], Copyright Massachusetts Medical Society.]

Functional deficits: RGC electrophysiological dysfunction

As outlined in the previous section, deficits in RGC axon transport do not occur uniformly throughout the glaucomatous retina. Studies have shown that RGC axonopathy occurs in clusters of neighboring cells throughout the retina.[48,50,65,95,112] This topographic degeneration of RGCs suggests that external cues in the immediate microenvironment may play an important role in spreading of axonopathy. Investigations into the mechanism of topographic spreading of axonopathy led to the question of whether deficits in axon transport reflect measurable changes in RGC function. Not surprisingly, several studies indicate that glaucomatous axonopathy is accompanied by changes in the electrophysiological properties of RGCs. Short-term elevations in IOP (1-2 weeks) via microbead injection in mice induce contrasting electrophysiological profiles in RGCs, where response to a preferred light stimulus is stronger, but spontaneous activity is decreased.[47] Beyond 4 weeks of elevated IOP, both the amplitude and frequency of induced and spontaneous activity is reduced in mice with ocular hypertension.[32,47,115,116] This is accompanied by increased depolarization of the resting membrane potential and increased variability in membrane noise.[47,115,116] These previous studies highlight important changes in RGC physiology happening during glaucoma pathology prior to physical degeneration of RGCs.

RGC physiology can also be measured in animals and human patients using electroretinography (ERG) and visual evoked potentials (VEP). The electrical response of the RGC soma or cortical RGC inputs is measured using ERG and VEP, respectively. RGC dysfunction will result in decreased amplitude and increased latency of the ERG and VEP waveforms.[117] In studies of human patients with OAG, there is increased latency and decreased amplitude of pattern ERG (PERG) and VEP peak waveforms, compared to normal controls.[118,119] Studies in DBA/2J mice show reduced amplitude of PERG and VEP waveforms between 4 and 7 months of age, with amplitudes continuing to steadily decrease as the animals age.[120,121] IOP elevation in several inducible glaucoma models in rodents also reduced the amplitude of ERG waveforms.[122,123] RGC dysfunction, reflected as changes in ERG or VEP waveforms, is susceptible to pharmacological intervention, as several studies in both human patients and DBA/2J mice have shown that IOP lowering therapies or neuroprotective agents can prevent or reverse ERG and VEP deficits.[107,117,120,124,125]

The period of time between onset of functional deficits and the physical degeneration of RGCs represents a potential therapeutic window to interrupt axonopathy and potentially recover vision that has been lost. Restoring function to unhealthy RGCs prior to structural degeneration could be a potentially good therapeutic approach. As the primary function of a neuron is to fire action potentials, one would therefore want to restore and maintain the electrophysiological function of these cells. There are many processes that could be targeted to maintain neuronal physiological in RGCs.

Maintenance of ion homeostasis in the retina

Maintaining electrochemical gradients of ions is critically important for sustaining proper electrophysiological function. Neurons require the correct balance of ions inside and outside the cell to initiate firing of action potentials, and depend on the reestablishment of those electrochemical gradients between action potentials to maintain continued firing. In the retina, the primary means by which RGCs reset the electrochemical gradient of ions is through the action of the Na/K-ATPase. The Na/K-ATPase resets the electrochemical gradients of ions following an action potential by pumping three Na^+ ions out for every two K^+ ions taken in.[126] A secondary means is through K^+ siphoning by Müller glia. Müller glia remove excess extracellular

K^+ via K^+ channels with inward rectifying capabilities, a process similar to K^+ buffering by astrocytes in brain.[127-129]

Role of Na/K-ATPase in neuronal signaling

The Na/K-ATPase is a membrane-bound protein, whose primary role is to maintain electrochemical Na^+ and K^+ ion gradients, by establishing high internal K^+ and low internal Na^+ concentrations.[126,130] In order to do this, the Na/K-ATPase uses energy from hydrolysis of one ATP molecule to transport three Na^+ ions out for every two K^+ ions taken in.[126] Broader functions of the Na/K-ATPase include controlling basic cellular homeostasis, such as osmotic balance and resting membrane potential[126,130], and supporting the excitability of neuronal and contractile tissues.[130] Additionally, the electrochemical Na^+ gradient produced by the Na/K-ATPase drives Na^+-coupled transporters, which mediate the translocation of ions, such as H^+, Ca^{2+}, or Cl^-, substrates like glucose and amino acids, or neurotransmitters across the plasma membrane.[126]

Na/K-ATPase activity is particularly important during the repolarization and hyperpolarization phases of the action potential. The action potential begins with the depolarization phase, where voltage-gated Na^+ channels open and Na^+ moves down its electrochemical gradient into the cell. Next, the repolarization phase begins with voltage-gated Na^+ channels closing, and voltage-gated K^+ channels opening, following which K^+ will move down its electrochemical gradient out of the cell. At this point, there are high levels of K^+ and low levels of Na^+ outside the cell. In order to fire another action potential, the electrochemical gradients of ions must be reestablished. This occurs during the latter half of the repolarization phase and during the hyperpolarization phase of the action potential and is accomplished primarily by activity of the Na/K-ATPase pumping Na^+ and K^+ ions back across their electrochemical gradients. Failure to reestablish the electrochemical gradients of ions between action potentials could lead to the inability of a cell to continue to fire action potentials.

Expression of Na/K-ATPase in retina

The Na/K-ATPase protein is comprised of two subunits, the α and β subunits. The α subunit is the catalytic subunit, responsible for catalytic and transport properties of the enzyme.[130] It also contains binding sites for cations, ATP, and pharmacological agents, such as ouabain.[130] The β subunit is a glycoprotein and is required for structural and functional formation of the α subunit. The β subunit can also modulate Na/K-ATPase transport properties, as it's involved in the occlusion of K^+ and modulation of Na^+ and K^+ affinity.[130] Additionally, it acts as a chaperone, stabilizing the correct folding of the α polypeptide to facilitate its delivery to the plasma membrane and plays a role in formation of tight junctions and cell polarity.[130] The *Atp1* gene family encodes the Na/K-ATPase in retina. *Atp1a1-4* encode the α1-4 isoforms of the catalytic subunit, and *Atp1b1-4* encode the β1-4 isoforms of the glycoprotein subunit.[126] RGCs in the retina express α1, α3, β1, and β2, while axons in the optic nerve express primarily α3 and β1.[131,132] The Na/K-ATPase is also expressed in many other cell types in the retina. In the retinal glial cells, Müller glia primarily express α2 and β2, while astrocytes in the optic nerve can express α1 or α2.[132] Photoreceptor inner segments express α3, β2, and β3.[132] There are also low levels of expression in bipolar cells, horizontal cells, and amacrine cells.[132] The α1β1 isoform of the protein is ubiquitously expressed in neurons and functions as a housekeeping pump to maintain basal ionic gradients.[126] During firing of an action potential, the α1 and α2 isoforms are activated first and once they reach saturation, α3 then becomes activated.[126]

There is some evidence for altered expression or activity of the Na/K-ATPase in the retina during disease, specifically glaucoma. Gene analysis studies found downregulation of Na/K-ATPase expression in circulating leucocytes in the blood of glaucoma patients.[133] They hypothesize that oxidative stress occurring during glaucoma could lead to reduced activity and expression of the Na/K-ATPase.[13,133] The Na/K-ATPase has also been linked to diabetic retinopathy. Diabetes causes oxidative stress in the eye, which results in elevated protein kinase C (PKC) activity leading to decreased Na/K-ATPase activity.[134] This, in turn, results in impaired ion homeostasis in the eye and altered activity of retinal and peripheral nerves.[134] Diabetic retinopathy also causes reduced metabolic activity due to the switch from the aerobic to anaerobic pathway. This significantly reduces the amount of ATP available to sustain Na/K-ATPase activity.[134] Studies show a potential link between diabetes (diabetic retinopathy) and glaucoma. External stressors, such as elevated IOP, have a more deleterious effect on diabetic eyes than normal eyes. There is additionally some evidence for diabetes causing RGC loss, which would compound the loss of RGCs seen during glaucoma, if both occurred in the same patient.[134]

Altered Na/K-ATPase activity or expression is also implicated in other neurodegenerative diseases. Reduced activity of the $\alpha1$, $\alpha2$, and $\alpha3$ subunits of the Na/K-ATPase is seen in neurons, glia, and myelinated axon tracts in the G93A mouse model of ALS.[135] It is hypothesized that the selective downregulation of the α subunit of the Na/K-ATPase is a downstream effect of oxidative damage to neurons caused by mutant SOD1 protein.[135] In *Drosophila melanogaster*, mutations in the gene encoding the α subunit of the Na/K-ATPase results in behavioral abnormalities, reduced life span, neuronal hyperexcitability, and age-dependent neurodegeneration.[136] Finally, the Na/K-ATPase may play a role in hypoxia-ischemia (HI)-

induced striatal neurodegeneration in newborn piglets.[137] Na/K-ATPase activity was significantly decreased (50-100%) 3-24hrs after HI.[137] Also, $\alpha 1$, $\alpha 3$ and $\beta 1$ isoform protein expression were all significantly reduced 3-24hrs after HI.[137] This indicates that reduced expression and activity of the Na/K-ATPase early after HI participates in pathology of striatal neurodegeneration.

Expression of the Na/K-ATPase can be modulated at the protein level by altering translocation of the protein to the plasma membrane or by promoting endocytosis.[138,139] Na/K-ATPase endocytosis is initiated by PKC- or p38-mediated phosphorylation of the $\alpha 1$ subunit of the Na/K-ATPase.[140-143] Following endocytosis, the Na/K-ATPase is degraded by the proteasome.[140,141] There is evidence that cell surface expression of the Na/K-ATPase can be modulated by trafficking of protein between a plasma membrane-associated pool and pool within intracellular compartments that has been internalized by endocytosis.[139,144,145] The Na/K-ATPase undergoes constitutive endocytosis and degradation.[143] Regulation of Na/K-ATPase cell surface expression can occur via control of this constitutively high rate of internalization and degradation. This process does not require *de novo* protein synthesis and thus is a very efficient mode of regulation allowing rapid adaptation of activity in response to cellular signals.[143] For example, an increase in the intracellular Na^+ concentration has been shown to increase Na/K-ATPase cell surface expression by inhibiting p38 kinase-mediated endocytosis, and eventual degradation, of the Na/K-ATPase.[143]

Role of K^+ siphoning in neuron signaling in retina

Several studies show that maintaining activity is crucial for neurons, like RGCs, to fulfill their physiological function and to simply survive throughout adulthood. Support from surrounding glia plays a critical role in maintaining RGC physiology and may play an important role in the progression of pathology in glaucoma. Müller glia are a retina-specific glial cell and the most abundant among glial subtypes in the retina.[146,147] The primary function of Müller glia is homeostatic regulation and metabolic support of retinal neurons, including neurotransmitter uptake, production of neurotransmitter precursors, production of trophic and anti-oxidative factors, and recycling of photopigments.[129,148]

Another important aspect of homeostatic regulation performed by Müller glia is a process referred to as K^+ siphoning.[128,129] This process is similar to spatial K^+ buffering by astrocytes in the brain.[127] Müller glia membranes have high K^+ conductance and are highly permeable to K^+, causing the membrane potential to be close to the equilibrium potential for K^+.[148] As RGCs fire action potentials, K^+ ions are released into the plexiform layers of the retina (**Figure 1.1**).[148-150] This produces a local driving force for inward K^+ currents in Müller glia cells, and as such Müller glia remove excess extracellular K^+ in the plexiform layers through K^+ channels with inward rectifying capabilities (**Figure 1.8**). A channel that is inwardly rectifying passes current more easily into the cell (inwardly) than out of the cell. The excess K^+ taken up by Müller glia is then transported into the blood, vitreous, and subretinal space (**Figure 1.8**).[148,150] K^+ siphoning by Müller glia is critical for RGCs to maintain proper physiology.[127,146,151,152] As outlined above, the electrochemical gradients of ions must be reset in order for a neuron to continue to fire action potentials. Müller glia assist RGCs in reestablishing the K^+ concentration gradient during the repolarization and hyperpolarization phases of the action potential.

Studies suggest that inwardly rectifying K^+ (Kir) channels, Kir4.1 and Kir2.1, in Müller glia are primarily responsible for K^+ regulation in the retina.[148,151,153] However, when Kir channels are blocked, the remaining K^+ conductance in Müller glia is mediated by two-pore domain (K2P) K$^+$ channels.[148,154] Accordingly, many K2P channels, including TWIK-1, TREK-2, TRESK, TASK-1, and TRAAK channels display weak inwardly rectifying properties.[155]

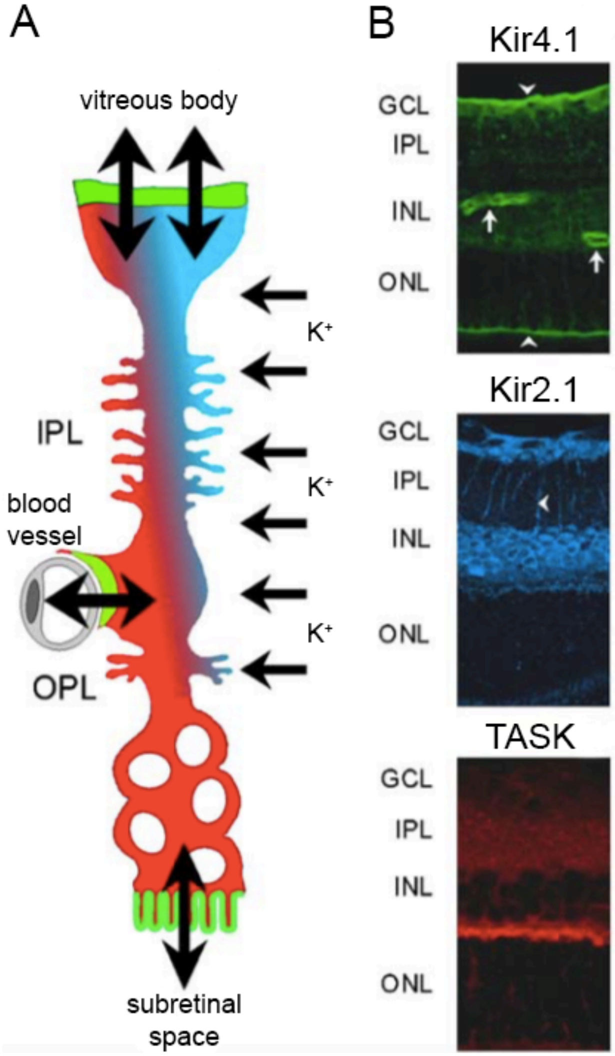

Figure 1.8. K$^+$ siphoning by Müller glia. (A) K$^+$ is released during neuronal signaling into the IPL. This generates a high extracellular K+ concentration and an influx of K$^+$ into Müller glia cells. K$^+$ efflux from the Müller glia then occurs into the vitreous, subretinal space, and blood vessels. The coloring indicates the distribution of K$^+$ channels along the Müller glia membrane: Kir4.1 in green, Kir2.1 in blue, and TASK in red. **(B)** Immunohistochemical staining for Kir4.1 (green), Kir2.1 (blue), and TASK3 (red) in rat wildtype retinal sections. Kir4.1 is expressed at the limiting membranes and perivascular membrane (arrows). Kir2.1 and TASK expression are more evenly distributed along the Müller glia membrane. GCL: ganglion cell layer; INL: inner nuclear layer; IPL: inner plexiform layer; ONL: outer nuclear layer. [Figure adapted from Bringmann et al. (2006) Prog Retin Eye Res[148] and used in accordance with Copyright Clearance Center's RightsLink service.]

Expression of Kir and K2P channels in retina

Müller glia express many different types of K^+ channels. The Kir4.1 and Kir2.1 subtypes of the inwardly rectifying K^+ channel family have been the most strongly implicated in mediating K^+ siphoning currents. Kir4.1 channels are weakly rectifying at rest and mainly located at the Müller glia endfeet and along the perivascular membrane area (**Figure 1.8**).[148] Kir2.1 channels are strongly rectifying at rest and present with even distribution across the Müller glia membrane between endfoot and soma, as well as membrane areas that contact retinal neurons (**Figure 1.8**).[148] Several channels from the K2P family, including TWIK-1, TREK-2, TRESK, TASK-1, and TRAAK, also display weak inwardly rectifying properties and are implicated in the K^+ siphoning process by Müller glia.[155] qPCR analysis of K2P channels in adult wildtype mouse retina revealed TWIK-1 to have the highest mRNA levels among the K2P family, followed in order by TRESK, TRAAK, and TASK-1. Finally, TREK-2 mRNA levels were much lower compared to the other four channels.[156] To examine expression and localization patterns, immunohistochemical analysis was also performed for K2P channels in wildtype mouse retinal sections. TWIK-1 and TRESK are expressed in both RGCs and Müller glia.[156] TREK-2 and TRAAK are predominantly expressed in Müller glia, but also expressed at lower levels in RGCs and the INL.[156] Finally, TASK-1 is predominantly expressed in RGCs, but also expressed at lower levels in Müller glia and the INL.[156] TASK expression is evenly distributed across the Müller glia membrane (**Figure 1.8**).[148]

Recent studies suggest that the expression and function of K^+ channels in Müller glia is altered in glaucoma and other retinal disorders, including retinitis pigmentosa and diabetic retinopathy.[157-159] In particular, chronic ocular hypertension in rats reduces Kir4.1, Kir2.1 and TASK-1 protein expression in Müller glia (*in vivo*).[158] Decreased expression of Kir4.1 in Müller glia is also noted in rat models of retinitis pigmentosa and diabetic retinopathy.[157,159] This decreased expression leads to decreased K^+ currents and altered electrophysiological properties in both conditions.[157,159] However, in the DBA/2J mouse model of glaucoma, reactive Müller glia do not exhibit changes in membrane current or membrane potential, as compared to Müller glia from control mice.[67] Rather, Müller glia in aged DBA/2 mice exhibit increased membrane capacitance, which is characteristic of hypertrophied, reactive glial cells.[160]

During reactive gliosis, currents through Kir channels are reduced, leading to activation of other types of K^+ channels, such as K2P channels, as added support to maintain the membrane potential.[161] This demonstrates the importance of investigating the K2P family of channels during a disease state such as glaucoma, where Müller glia gliosis is common.[148] Additionally, TRAAK activation is induced by mechanical stretch or strain to the cell.[162] This mechanical gating could be relevant for pressure-sensitivity in the retina and have significant implications for Müller glia-mediated ion homeostasis in glaucoma.

Potential etiology of spatial clusters of RGC degeneration

Further investigations are needed to fully understand how electrophysiological aberrations relate to axon transport deficiencies evident in the early stages of axonopathy.[47] This stage of disease progression is particularly important, as the period of time between onset of functional deficits and the physical degeneration of RGCs represents a potential therapeutic window to interrupt axonopathy prior to irreversible, structural loss. Several studies have shown that deficits in axon transport do not occur uniformly throughout the glaucomatous retina and that RGC axonopathy occurs in clusters of neighboring cells.[48,50,65,95,112] It is therefore highly likely that any electrophysiological deficits accompanying axon transport deficits in the retina also occur in a topographic manner. The potential for ion dyshomeostasis to act as a propagating agent for electrophysiological impairment introduces a novel possibility for etiology of spatial clustering of RGC pathology and vision loss.

Impairment of electrochemical gradients has the potential to serve as an external cue to propagate physiological dysfunction, and ultimately, degeneration, between RGCs. Disturbance of K^+ and Na^+ gradients produces elevated K^+ in the immediate extracellular milieu, which presents a challenge for neighboring RGCs in the maintenance of their electrochemical gradient. When compounded by IOP-related stress, this could readily produce impairment in spiking ability within these cells. This, in turn, would lead to broader disturbances in K^+ and Na^+ gradients impacting additional surrounding RGCs and so on. Furthermore, this mechanism could be relevant for other neurodegenerative diseases, in which axon transport deficits and spatial spread of degeneration are elements of pathology, i.e. Alzheimer's disease, Lewy body dementia, Down syndrome, and multiple system atrophy.[39-42,113,114]

Specific Aims of Dissertation

The *objective* of this thesis project is to identify extracellular events that could underlie the spatiotemporal progression from functional deficits to structural RGC degeneration in glaucoma. Our *central hypothesis* is that disruption of K^+ homeostasis underlies electrophysiological impairment of RGCs during glaucoma via changes in the expression and activity of the Na/K-ATPase. This hypothesis is based on 1) previous studies which indicate that axon transport deficits in RGCs are accompanied by electrophysiological impairment, specifically difficulty in re-establishing the electrochemical gradients of ions, 2) data indicating decreased expression of the Na/K-ATPase in glaucomatous retina, and 3) *in vitro* studies, which show that ion flux through K^+ channels decreases following exposure to glaucoma-related stressors. To test our central hypothesis, we developed these specific aims:

Aim 1. Determine the nature of the electrophysiological deficits in RGCs during glaucoma.

Our *working hypothesis* is that impaired membrane repolarization underlies electrophysiological impairment of RGCs via inability to properly reestablish ion concentration gradients. To test our hypothesis, we will examine outcome measures of RGC physiology in MOM retina, and compare electrophysiological performance of RGCs to degree of tracer uptake/transport. Additionally, we will examine expression of K^+ channels responsible for establishing ion concentration gradients in MOM retina.

Aim 2. Determine the mechanism responsible for K^+ dyshomeostasis during glaucoma and implications for RGC physiology.

Our *working hypothesis* is that Na/K-ATPase-mediated disruption of K^+ homeostasis underlies electrophysiological impairment of RGCs during glaucoma. In primary, purified cultures of RGCs and Müller glia, we will examine outcome measures of K^+ channel expression, ion homeostasis, and ion flux to examine the impact of glaucoma-related stressors on K^+ dynamics in RGCs and Müller glia individually (*in vitro*). Additionally, we will measure the response of pharmacologically inhibiting or activating K^+ channels on ion flux and physiology in RGC and Müller glia cultures. Finally, we will pharmacologically inhibit the Na/K-ATPase in the intact retinal circuit (*ex vivo*) to examine outcome measures of RGC physiology and relate any changes to those found in K^+ homeostasis *in vitro*.

CHAPTER 2

K^+ CHANNEL-MEDIATED IMPAIRMENT OF MEMBRANE REPOLARIZATION ACCOMPANIES AXON TRANSPORT DEFICITS IN RETINAL GANGLION CELL AXONOPATHY [2]

Introduction

Progressive and irreversible degeneration of RGCs during glaucoma is the cause of irreversible vision loss for millions of individuals worldwide.[3,163] Treatments targeting the primary, modifiable risk factor, elevated IOP, only slow progression of the disease.[3,163] Therefore, new therapeutic interventions that address the fundamental mechanisms of RGC degeneration are necessary to halt progression of the disease and preserve vision.

As described in detail in Chapter 1, RGC degeneration, termed axonopathy, occurs in a temporal series of events that is common to several neurodegenerative diseases, such as Parkinson's disease, Alzheimer's disease, and ALS.[3,39-45] RGC axonopathy beings with functional deficits in axon transport and is followed by retrograde structural degeneration of the axon.[3] Later stages of axonopathy include glial inflammation in the retina and ONH, synapse elimination, dendritic pruning, and finally apoptotic death of the RGC soma.[13,46-49,164] Another key feature of RGC axonopathy is the spatial patterning across the retina. For example, deficits in axon transport occur in clusters of neighboring RGCs, in a pattern that is consistent with sectorial vision loss in glaucoma patients.[3,94,165] Topographic degeneration is another characteristic of axonopathy that is shared among many neurodegenerative diseases.[113,114]

---

[2] Portions of this chapter were published as Fischer et al. (2019) American Journal of Physiology—Cell Physiology.

Axonopathy in glaucoma results in progressive loss of connection between RGCs and both their pre- and post-synaptic targets.[13,47,110,165,166] As such, several studies indicate that glaucomatous axonopathy is accompanied by altered electrophysiological function of RGCs. Short-term elevations in IOP (1-2 weeks) result in reduced spontaneous activity of RGCs, but an increased response to a preferred light stimulus.[47] Longer elevations in IOP (≥4 weeks) lead to reduced frequency and amplitude of both induced and spontaneous electrophysiological activity in RGCs.[47,115,116] Further study is needed to elucidate the relationship between axon transport deficits and electrophysiological dysfunction in RGCs in the early stages of axonopathy.[47] This stage of disease progression is particularly important, as the period of time between onset of functional deficits and the physical degeneration of RGCs represents a potential therapeutic window to interrupt axonopathy prior to irreversible, structural loss.

Here we sought to: 1) identify relationships between electrophysiological function and axon transport deficits in glaucomatous RGCs and 2) elucidate the pressure-dependent mechanisms underlying any such relationship. Our findings indicate that deficits in axon transport reflect measurable deficiencies in the ability of RGCs to maintain spiking frequency. This physiological phenotype appears to arise from elongation of the repolarization phase of the action potential.

There are two mechanisms in the retina by which electrochemical gradients of ions are established during the repolarization phase of the action potential. The primary means by which RGCs reset the electrochemical gradient of ions is through the Na/K-ATPase. The Na/K-ATPase resets the electrochemical gradient following an action potential by pumping 3 Na^+ ions out for every 2 K^+ ions taken in. A secondary means is through K^+ siphoning by Müller glia. In response to action potentials generated by RGCs, Müller glia remove excess extracellular K^+ through K^+

channels with inward rectifying capabilities. K^+ siphoning is critical for RGCs to maintain proper physiology.[127,146,151,152] Inwardly rectifying Kir4.1 and Kir2.1 channels have been implicated as the K^+ channels that are primarily responsible for K^+ siphoning by Müller glia.[151,153] Additionally, K^+ channels from the K2P family with weak inwardly rectifying properties, such as TWIK-1, TREK-2, TRESK, TASK-1, and TRAAK, have also been shown to contribute to K^+ conductance in Müller glia.[154,155] In the previous chapter, evidence was outlined suggesting that the expression and function of Kir and K2P channels in Müller glia is altered in glaucoma and other retinal disorders, including retinitis pigmentosa and diabetic retinopathy (Chapter 1).[157-159]

To determine if elevated IOP directly alters expression and function of K^+ channels in the retina implicated in maintenance of ion homeostasis, we examined changes in the expression of the Na/K-ATPase and Kir and K2P channels with inward-rectifying capabilities in the retina of mice with ocular hypertension.[16] Pressure-induced changes in expression profiles of the Na/K-ATPase, Kir, and K2P channels were investigated via whole retina transcriptome analysis and immunohistochemical staining of whole eye sections.

Materials and Methods

Induction of ocular hypertension using the Microbead Occlusion Model in mice

Mice were housed in accordance with NIH guidelines and maintained on a 12-hour light/dark cycle with free access to food and water. All experiments were approved by the Institutional Animal Care and Use Committee of Vanderbilt University Medical Center. C57Bl/6 mice were obtained from Charles River Laboratories (Wilmington, MA). IOP elevation was induced in 1-month-old C57Bl/6 mice, using the microbead occlusion model, as previously described.[16,96,165,167,168] Briefly, anesthetized animals received bilateral injections of 1.5µL sterile

15-μm polystyrene beads (1×10^6 microbeads/mL; Cat# F8844, Life Technologies). Control mice received bilateral injections of an equal volume of saline.

IOP measurements

IOP elevation lasted 4 weeks, at which point the animals were sacrificed. IOP was measured in awake, behaving mice, using a TonoLab tonometer (TonoLab; Reichert, Depew, NY; 13,21). IOP was determined as the mean of 10 individual measurements. Prior to initial microbead or saline injections, baseline IOP was recorded for 3 consecutive days. Following injections, IOP was recorded 3 times a week throughout the 4-week experiment. Mean IOP with standard deviations are provided for each dataset in result text. For each dataset, microbead injection increased mean IOP by approximately 25%, as compared to naïve or saline-injected eyes ($p<0.01$ for all).

Electrophysiology

48 hours prior to electrophysiology experiments, mice received a bilateral, intravitreal injection of the neural tracer cholera toxin beta subunit to label RGCs.[50,96] Whole-cell recording was performed, as previously described.[47] Under dim red light (630 nm, 800 μW/cm^2, Ushio FND/FG), animals were euthanized by cervical dislocation, and retinas were dissected out of the orbit. Whole retinas were mounted onto a physiological chamber and perfused with carbogen-saturated Ames' medium, supplemented with 20 mM glucose (pH 7.4, 290 Osm), at a rate of 2 mL/min, heated to 32^{o}C (TC-344C, Warner Instruments). Patch pipettes were fabricated from thick-walled borosilicate glass and heat-pulled (P-2000, Sutter Instruments). Pipettes were loaded with (in mM) 125 K-gluconate, 10 KCl, 10 HEPES, 10 EGTA, 4 Mg-ATP, 1 Na-GTP,

and 1 Lucifer Yellow (pH 7.35, 287 Osm), and had a resistance between 4-8 MΩ. We targeted RGCs with large somas (>15 μm in diameter) for whole-cell recording. Whole-cell voltage signals were amplified (Multiclamp 700B, Molecular Devices) and digitized at a sampling rate of 50 kHz (Digidata 1550A, Molecular Devices). Throughout each experiment, access resistance was continually monitored and was less than 30 MΩ.

We measured spontaneous activity under normal extracellular solution conditions for 1-2 min (3 mM KCl). Then, we increased [K^+] of the extracellular bath solution to 13 mM by adding additional KCl. Once, the cell's response stabilized, the bath solution was changed to the normal solution for at least 10 min to allow the tissue to recover. Afterwards, extracellular [K^+] was increased to 23 mM by addition of KCl. After the cell's potential stabilized, we exchanged the high [K^+] solution back to normal solution and thoroughly washed out the chamber prior to further experiments.

In a separate set of experiments, we performed whole-cell current-clamp (0 pA) recordings from RGCs while applying ouabain (10 or 20 μM, Cat# O3125, Sigma Aldrich, St Louis, MO) via a wide-bore pipette attached to pneumatic microinjection device (PicoSpritzer II, General Valve Corp.). The "puff" pipette was positioned approximately 150-200 μm from the RGC soma and 10 or 20 μM ouabain, which was dissolved in extracellular medium, was administered for 30 ms at 10-12 psi while recording the drug-induced spike activity and membrane potential. After each experiment, the drug was thoroughly washed out with extracellular solution.

RNA sequencing

Whole, intact retina was dissected from MOM mice following sacrifice. Immediately following dissection, RNA was extracted from retina using TRIzol (Invitrogen, Cat# 15596026) and treated with deoxyribonuclease (DNase) I (Worthington, Cat# LS006333). Experiments were performed through the Vanderbilt Technologies for Advanced Genomics core at Vanderbilt University Medical Center. DNase-treated total RNA quality was assessed using the 2100 Bioanalyzer (Agilent Technologies). Any samples with integrity values greater than 6 were used to generate polyA (mRNA)-enriched libraries, using stranded mRNA sample kits with indexed adaptors (New England BioLabs, Ipswich, MA). The RNA library quality was assessed using the 2100 Bioanalyzer (Agilent Technologies) and libraries were quantitated using KAPA Library Quantification Kits (KAPA Biosystems, Wilmington, MA). Pooled libraries were subjected to 100bp paired-end sequencing according to the manufacturer's protocol (Illumina NovaSeq6000). Bcl2fastq2 Conversion Software (Illumina, San Diego, CA) was used to generate de-multiplexed Fastq files. Analysis of RNAseq results was performed through the Vanderbilt Technologies for Advanced Genomics Analysis and Research Design (VANGARD) core at Vanderbilt University. Reads were aligned to the GENCODE GRCm38.p5 genome using STAR v2.5.3a. GENCODE vM12 gene annotations were provided to STAR to improve the accuracy of mapping. Quality control on raw reads was performed using FastQC. FeatureCounts v1.15.2 was used to count the number of mapped reads to each gene. Significantly differential expressed genes with adjusted p-value <0.05 and absolute fold change >2 were detected by DESeq2 v1.14. The Data are reported as fold change (log scale) and percent change in RNA transcript levels between saline and microbead retina. The Data have been deposited in NCBI's Gene Expression Omnibus and are accessible through GEO series accession number GSE116915 (https://www.ncbi.nlm.nih.gov/geo/query/acc.cgi?acc=GSE116915).

Immunohistochemistry

We assessed expression and localization patterns of K^+ channel expression using immunohistochemistry.[169-173] Immunohistochemistry experiments were done on longitudinal paraffin-embedded retina sections of whole eyes from microbead-injected, saline-injected, and naïve mice. Samples were incubated in blocking solution containing 5% normal horse serum (NHS; Life Technologies) and 0.1% Triton-X (Fisher Scientific) in 1X PBS. Samples were then incubated overnight at 4°C in primary antibody solution (3% NHS and 0.1% Triton X-100 diluted in 1X PBS) containing: rabbit anti-Total Na/K-ATPase (2ug/ml, Cat# ab58475, Abcam, Cambridge, UK), rabbit anti-α1 Na/K-ATPase (2.85ug/ml, Cat# ANP-001, Alomone, Jerusalem, Israel), mouse anti-β-TubulinIII (2ug/ml, Cat# 801201, BioLegend, London, UK), rabbit anti-Kir2.1 (5ug/ul, Cat# APC-026, Alomone Labs, Jerusalem, Israel), rabbit anti-Kir4.1 (2ug/ml, Cat# APC-035, Alomone Labs), rabbit anti-TRAAK (5ug/ml, Cat# APC-108, Alomone Labs), rabbit anti-TRESK (5ug/ml, Cat# APC-122, Alomone Labs), rabbit anti-TREK2 (5ug/ml, Cat# APC-055, Alomone), rabbit anti-TASK1 (5ug/ml, Cat# APC-024, Alomone), rabbit anti-TWIK1 (5ug/ml, Cat# APC-110, Alomone), and rat anti-CD44 (6.7ug/ml, Cat# 14-0441, Invitrogen). Following 1X PBS washes, samples were incubated for 2 hours at room temperature in a secondary antibody solution containing: 1% NHS, 0.1% Triton X-100 and 647-donkey anti-mouse (7.5ug/ml; Cat# 715-606-150, Jackson ImmunoResearch), 647-donkey anti-rat (7.5ug/ml; Cat# 712-605-153, Jackson ImmunoResearch), or 488-donkey anti-rabbit (7.5ug/ml; Cat# 711-546-152, Jackson ImmunoResearch) in 1X PBS. Samples were counterstained with the nuclear stain DAPI (50ug/ml; Cat# D1306, Life Technologies) and coverslipped in aqueous mounting media (Southern Biotech, Birmingham, AL). Immunolabeling was imaged at 20X, 40X, or 60X using an Olympus FV-1000 inverted confocal microscope (Olympus, Tokyo, Japan). Mean fluorescence intensity was calculated using the FIJI Color Histogram tool (ImageJ).

Statistical analysis

All statistical tests were conducted with SigmaPlot (Systat Software Inc., San Jose, CA). Experimental groups were compared within time points by student's t-test. Normality (Shapiro-Wilk) and equal variance was also assessed for each comparison. Comparisons between time points within groups were assessed by one-way ANOVA followed by pairwise comparison by either the Tukey or Dunn's method. Significant comparisons marked by brackets and asterisks. For all analyses, $p \leq 0.05$ was considered statistically significant.

Results

Impairment of electrochemical gradients in glaucomatous RGCs

In order to examine the potential relationship between electrophysiological function and axon transport deficits in glaucomatous RGCs, we performed whole-cell patch-clamp recordings in RGCs labeled with the neural tracer CTB. Retina from microbead-injected (IOP = 21mmHg+/-0.93mmHg) mice exhibited clusters of RGCs with deficient CTB transport (**right panel; Figure 2.1A**), as compared to intact and uniform tracing observed in saline-injected mice (IOP = 14mmHg+/-0.93mmHg; **left panel; Figure 2.1A**). In microbead-injected mice, RGCs with deficient CTB transport exhibit a significantly more depolarized resting membrane potential (Vm), compared to RGCs from saline retina with intact tracing (**Figure 2.1B**, $p<0.001$). Current clamp mode (20pA/1sec steps; 0-180pA) revealed significantly lower frequency of action potential firing at each current step, excluding 0pA, in RGCs from microbead retina, as compared to RGCs from saline retina (**Figure 2.1C**, $p<0.05$). Representative traces of spiking at 180pA are shown in **Figure 2.1D**. Inability of a neuron to maintain induced spiking can indicate impaired capacity to reestablish electrochemical gradients of ions during repolarization, which is required for the neuron to continuously fire action potentials.

Therefore, we sought to investigate whether altered ion concentration gradients underlie the reduced spiking frequency and depolarized resting membrane potential of glaucomatous RGCs by disrupting the extracellular concentration of K^+ ($[K^+]_E$) in the electrophysiological bath. We recorded spontaneous activity of RGCs in normal, control bath and bath containing 10 or 20mM of KCl. In naïve retina, increasing $[K^+]_E$ depolarized the resting membrane potential and induced firing of action potentials in RGCs.[174] In saline retina (white bars), 10 or 20mM KCl induced a reciprocal increase in the spike frequency of RGCs. This resulted in a significant increase in the event frequency between RGCs in control bath vs. 20mM KCl (**Figure 2.1E**, $p<0.05$). In microbead retina (gray bars), 10 or 20mM KCl also significantly increased the spiking frequency (**Figure 2.1E**, $p<0.05$). However, the magnitude of this increase was smaller, resulting in a significantly lower spike frequency in RGCs from microbead retina than in saline retina (**Figure 2.1E**, $p<0.005$). In RGCs from both saline (white bar) and microbead (gray bar) retina, increasing $[K^+]_E$ induced a reciprocal decrease in the peak amplitude of spikes that was significantly different between control and 20mM KCl bath conditions (**Figure 2.1F**, $p<0.05$ for both). However, the amplitude of spikes in RGCs from microbead retina was lower than those in saline retina at control and 20mM KCl bath conditions (**Figure 2.1F**, $p<0.05$ for both).

To independently evaluate the depolarization and repolarization phases of the action potential, we compared the max rise and decay slope in saline and microbead RGCs following increases in $[K^+]_E$. For the depolarization phase, there was no significant difference in the max rise slope between RGCs from saline or microbead retina, at any $[K^+]_E$ (**Figure 2.1G**, $p>0.05$). For the repolarization phase, increases in the decay slope towards a value of 0 indicated flattening and slowing of this phase. In RGCs from saline retina (white bars), increased $[K^+]_E$ induced a reciprocal increase in the max decay slope of the action potential that was statistically significant at 20mM KCl, as compared to control bath (**Figure 2.1H**, $p<0.05$). In RGCs from microbead retina (gray bars), the decay slope also significantly increased as $[K^+]_E$ increased (**Figure 2.1H**, $p<0.05$). KCl-induced increases in the decay slope were greater in RGCs from microbead retina than those from saline retina, which resulted in a significant difference at 10mM KCl (**Figure 2.1H**, $p<0.001$). These data indicate that RGCs with pressure-induced axon transport deficits also exhibit a compromised ability to maintain induced spiking. Due to the phenotype seen during the repolarization phase of the action potential, we hypothesize that this reduced ability to maintain induced spiking is due to altered electrochemical gradients of ions.

Ocular hypertension alters transcription of K^+ channels in vivo

The Na/K-ATPase is the primary mechanism by which electrochemical gradients of ions are reestablished in neurons, including RGCs. In the retina, K^+ siphoning by Müller glia is an additional mechanism by which electrochemical gradients are maintained. Kir and K2P K^+ channels with inward-rectifying capabilities have been implicated in the maintenance of K^+ homeostasis by Müller glia.[155,158,175,176] To determine whether ocular hypertension alters the expression of K^+ channels responsible for maintenance of ion homeostasis in the retina, we

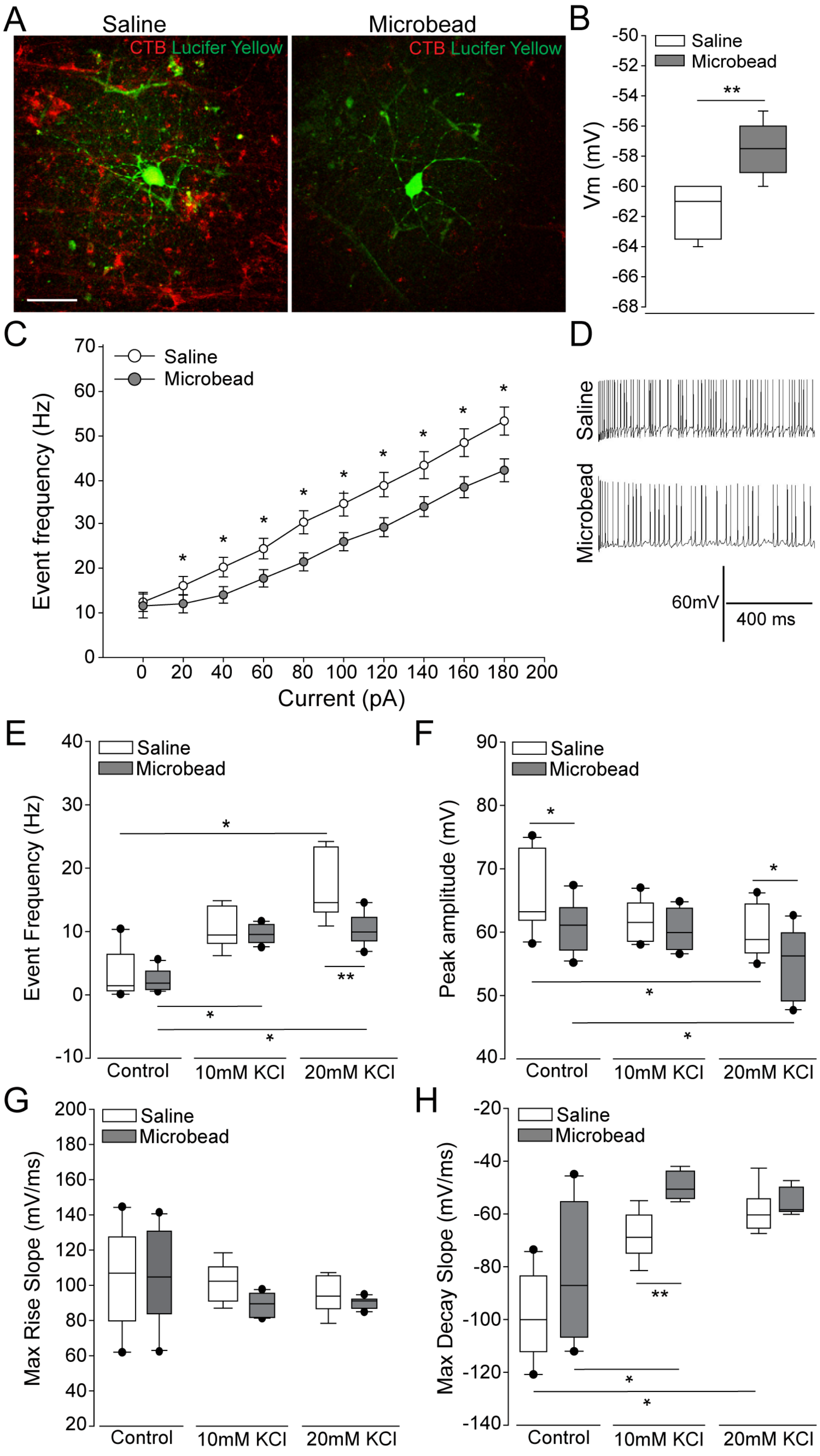
A
Saline
Microbead
CTB Lucifer Yellow
CTB Lucifer Yellow
B
Saline
Microbead
Vm (mV)
**
-50
-52
-54
-56
-58
-60
-62
-64
-66
-68
C
Saline
Microbead
Event frequency (Hz)
Current (pA)
0 10 20 30 40 50 60 70
0 20 40 60 80 100 120 140 160 180 200
D
Saline
Microbead
60mV
400 ms
E
Saline
Microbead
Event Frequency (Hz)
40 30 20 10 0 -10
Control
10mM KCl
20mM KCl
F
Saline
Microbead
Peak amplitude (mV)
90 80 70 60 50 40
Control
10mM KCl
20mM KCl
G
Saline
Microbead
Max Rise Slope (mV/ms)
200 180 160 140 120 100 80 60 40 20
Control
10mM KCl
20mM KCl
H
Saline
Microbead
Max Decay Slope (mV/ms)
-20 -40 -60 -80 -100 -120 -140
Control
10mM KCl
20mM KCl

Figure 2.1. RGCs with deficient axon transport exhibit decreases in induced spiking frequency that result from delayed repolarization. (**A**) Representative confocal micrographs of RGCs in whole retina following electrophysiological recordings from saline- (left) and microbead-injected (right) eyes. RGCs are CTB-traced (red) and filled with lucifer yellow (green). Scale bar = 50µM. (**B**) Mean resting membrane potential (Vm) of RGCs from saline- (white) and microbead-injected (gray) retina. Asterisks indicate $p < 0.001$ and error bars represent SEM. n(saline)=27, n(microbead)=34. (**C**) Frequency of spiking of RGCs from saline- (white) and microbead-injected (gray) retina following current stimulation in 20pA steps for 1 sec from 0 to 180pA. Mean event frequency (Hz) is displayed at each current step. Asterisks indicate $p < 0.05$. n(saline)=26, n(microbead)=26. (**D**) Representative traces of spiking with 180pA stimulation. (**E**) Frequency of spontaneous spiking of RGCs from saline- (white) and microbead-injected (gray) retina in control bath, or bath containing 10mM or 20mM KCl. Data is displayed as mean event frequency (Hz) across cells for each condition. Asterisks indicate $^{*}p < 0.05$, $^{**}p < 0.005$. n(saline)=12, n(microbead)=10, n(saline 10)=9, n(microbead 10)=12, n(saline 20)=9, n(microbead 20)=11. (**F**) Peak amplitude of spontaneous spiking of RGCs. Data is displayed as mean peak amplitude (mV) across cells for each condition. Asterisk indicates $^{*}p < 0.05$. n(saline)=11, n(microbead)=11, n(saline 10)=10, n(microbead 10)=12, n(saline 20)=11, n(microbead 20)=17. (**G**) Max rise slope of spontaneous spiking of RGCs. Data is displayed as mean max rise slope (mV/ms) across cells for each condition. n(saline)=14, n(microbead)=13, n(saline 10)=9, n(microbead 10)=10, n(saline 20)=9, n(microbead 20)=10. (**H**) Max decay slope of spontaneous spiking of RGCs. Data is displayed as mean max decay slope (mV/ms) across cells for each condition. Asterisks indicate $^{*}p < 0.05$, $^{**}p < 0.001$. n(saline)=10, n(microbead)=12, n(saline 10)=9, n(microbead 10)=9, n(saline 20)=9, n(microbead 20)=9.

examined transcription of the Na/K-ATPase (*Atp1*), Kir channel (*Kcnj*), and K2P channel (*Kcnk*) gene families. Transcriptional expression of these genes was quantified by RNA sequencing in whole retina of C57Bl/6 mice 4 weeks after either saline (IOP = 15mmHg+/-0.43mmHg) or microbead (IOP = 21mmHg+/-0.53mmHg) injection. Transcriptome analysis revealed a significant IOP-dependent decrease in the transcription of *Atp1a1* by 41.3% and increase in *Atp1b2* by 53.7% (**Figure 2.2A**, $p<0.005$). There was no significant difference observed in transcription of *Atp1a2, a3, a4, b1, b3,* or *b4* in microbead- versus saline-injected eyes ($p>0.05$; **Figure 2.2A**). *Atp1a1* encodes the $\alpha 1$ isoform of the catalytic subunit, and *Atp1b2* encodes the $\beta 2$ isoform of the glycoprotein subunit of the Na/K-ATPase.

Transcriptome analysis revealed IOP-dependent decreases in the transcription of genes encoding several Kir channels (**Figure 2.2B**). In order of magnitude, microbead-induced IOP elevation decreased transcription of Kir3.2 (*Kcnj6*; 56%), Kir2.2 (*Kcnj12*; 51%) and Kir2.4 (*Kcnj14*; 42%), as compared to saline-injected retina ($p<0.05$ for all; **Figure 2.2B**). There was no significant difference observed in transcription of genes encoding Kir1.1 (*Kcnj1*), Kir2.1 (Kcnj2), Kir2.3 (*Kcnj4*), Kir3.4 (*Kcnj5*), Kir4.1 (*Kcnj10*), Kir6.1 (*Kcnj8*), Kir5.1 (*Kcnj16*), Kir3.1 (*Kcnj3*), Kir3.3 (*Kcnj9*), Kir6.2 (*Kcnj11*), Kir7.1 (*Kcnj13*) and Kir4.2 (*Kcnj15*) in microbead- versus saline-injected eyes ($p>0.05$; **Figure 2.2B**).

For K2P channels, elevated IOP *in vivo* reduced transcription of THIK2 (*Kcnk12*; 60%), TASK-1 (*Kcnk3*; 34%) and TWIK-1 (*Kcnk1*; 26%), as compared to saline-injected eyes ($p<0.05$ for all; **Figure 2.2C**). Like Kir channel expression, there were no statistically significant increases in K2P channel transcription (**Figure 2.2C**). There was no significant difference in transcription of genes encoding TRAAK (*Kcnk4*), TREK-1 (*Kcnk2*), TREK-2 (*Kcnk10*), TRESK (*Kcnk18*), TASK-2 (*Kcnk5*), TWIK-2 (*Kcnk6*), TASK-3 (*Kcnk9*), THIK-1 (*Kcnk13*), TASK-5 (*Kcnk15*), or TWIK-3 (*Kcnk7*) in microbead- versus saline-injected eyes ($p>0.05$ for all; **Figure 2.2C**). Together, these data suggest that elevated IOP *in vivo* decreases transcription of a small subset of Kir and K2P channels with inward-rectifying capabilities. Interestingly, elevated IOP does not increase transcription of any Kir or K2P channels at the whole retina level.

Transcriptome analysis is useful for identifying global shifts in transcriptional expression of K^+ channels. However, ion channel activity is often regulated at the protein level, i.e. by increased protein degradation or increased levels at the plasma membrane. Therefore, we next elected to examine protein localization and relative level of protein expression for individual Kir and K2P channels in the ocular hypertensive retina.

Ocular hypertension alters expression of the Na/K-ATPase

To determine the localization of IOP-dependent changes in Na/K-ATPase expression in

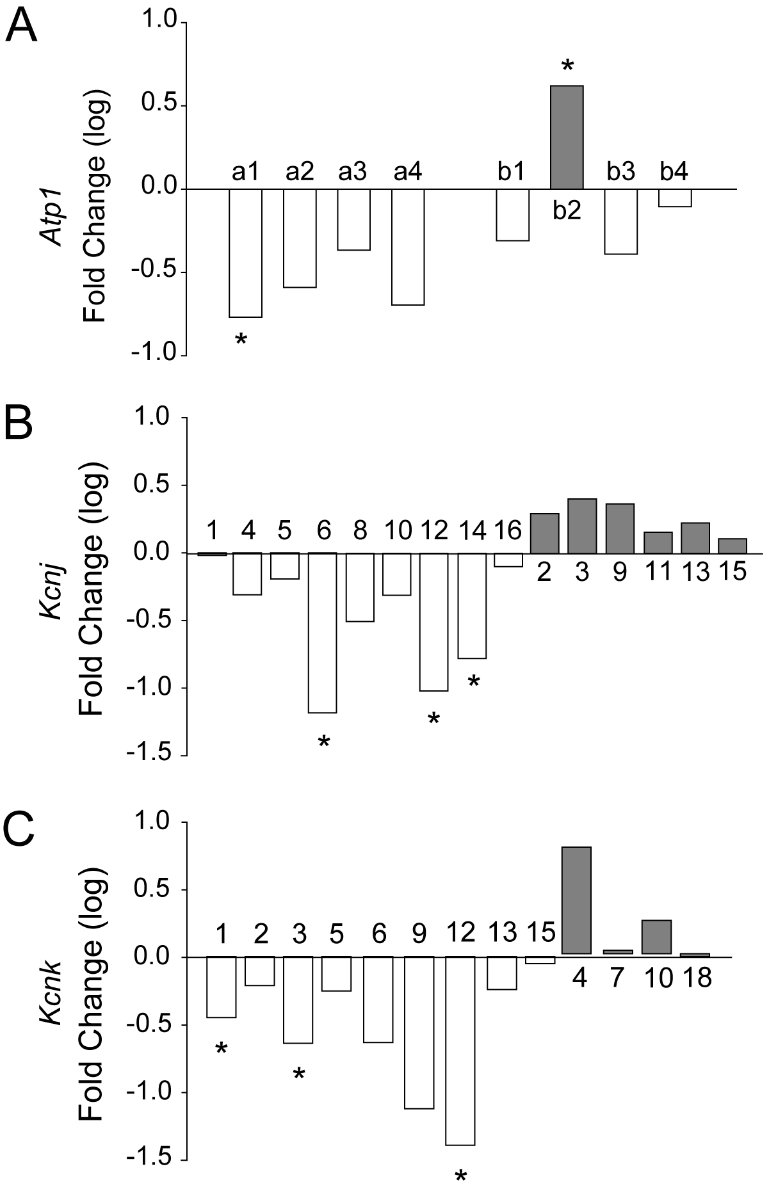

Figure 2.2. Ocular Hypertension Alters RNA Expression of K^+ Channels *In Vivo*. RNA sequencing was performed on whole retina from saline- and microbead-injected eyes. (**A**) Box plots of fold change (log scale) in expression of the *Atp1* gene family between retinas from saline- and microbead-injected mice. Asterisks indicates $p < 0.005$. (**B**) Box plots of fold change (log scale) in expression of the *Kcnj* gene family. Asterisks indicate $p < 0.05$. (**C**) Box plots of fold change (log scale) in expression of the *Kcnk* gene family. Asterisks indicate $p < 0.05$. n(saline)=5 retinas, n(microbead)=5 retinas. [Figure adapted from Fischer et al. (2019) Am J Physiol Cell Physiol[177] and used in accordance with Copyright Clearance Center's RightsLink service]

the retina, we performed immunohistochemical staining for total Na/K-ATPase in retinal sections from naïve, saline-, and microbead-injected mice. Qualitatively, immunolabeling for total Na/K-ATPase (green) was reduced in retina from microbead-injected mice, as compared to both naïve and saline-injected controls (**Figure 2.3A**). This decrease in total Na/K-ATPase immunolabeling was particularly evident in the GCL (**Figure 2.3A**). Quantification of immunolabeling intensity confirmed that elevated IOP in microbead-injected eyes (IOP = 21mmHg+/-1.1mmHg) decreased intensity of total Na/K-ATPase by 38 and 42%, as compared

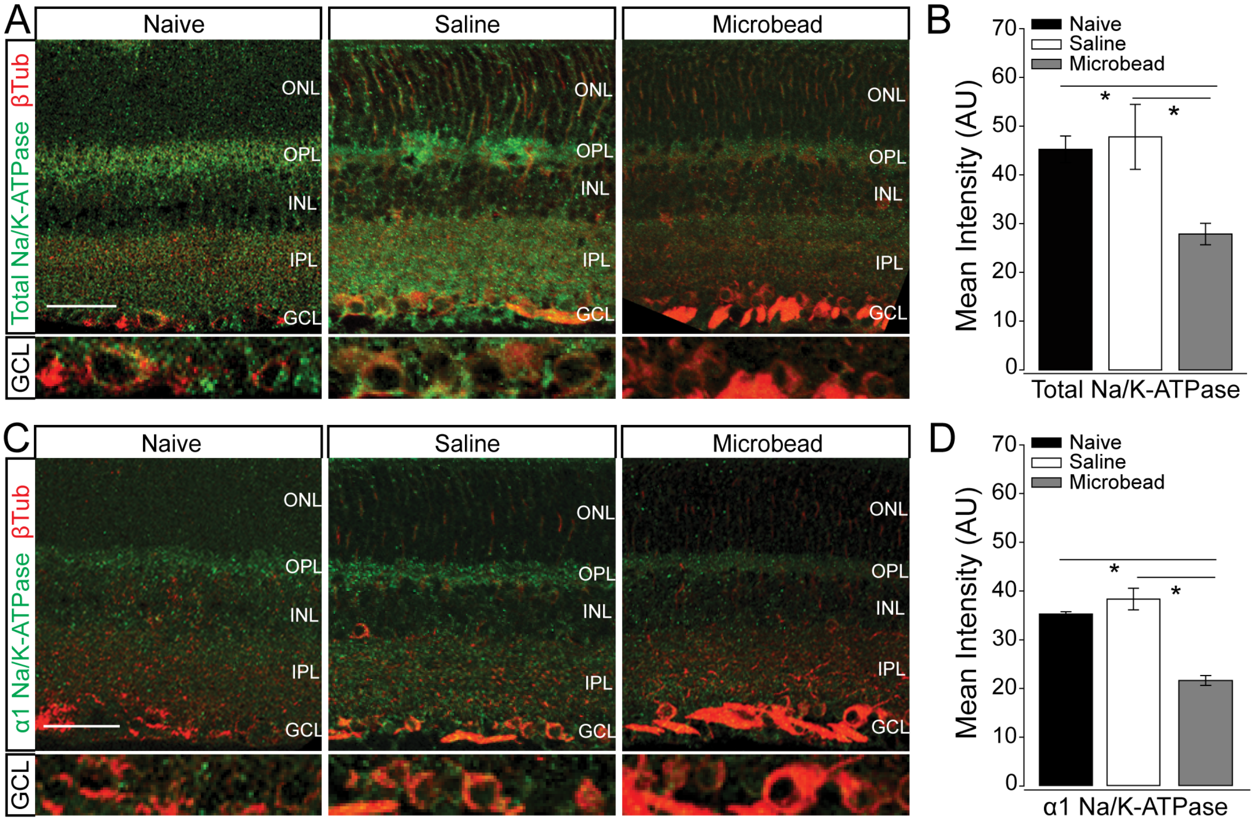

Figure 2.3. Intensity of total and α1 Na/K-ATPase staining in glaucomatous retinal sections. (**A**) Representative confocal micrographs of total Na/K-ATPase (green) and β-Tubulin-III (β-Tub; red) immunolabeling in retinal sections from naïve, saline-, and microbead-injected mice. Bottom panels of each image are a zoom of the ganglion cell layer (GCL). Scale bar = 40 μM. (**B**) Mean intensity of total Na/K-ATPase immunolabeling in retina from naïve, saline-injected, and microbead-injected mice. Asterisk indicates $p < 0.05$ and error bars represent SEM. n(naïve)=8, n(saline)=9, n(microbead)=9. (**C**) Representative confocal micrographs of α1 Na/K-ATPase (green) and β-Tubulin-III (β-Tub; red) immunolabeling in retinal sections from naïve, saline-, and microbead-injected mice. Bottom panels of each image are a zoom of the ganglion cell layer (GCL). Scale bar = 40 μM. (**D**) Mean intensity of α1 Na/K-ATPase immunolabeling in retina sections from naïve, saline-injected, and microbead-injected mice. Asterisk indicates $p < 0.05$ and error bars represent SEM. n(naïve)=4, n(saline)=8, n(microbead)=5. Abbreviations: ONL: outer nuclear layer, OPL: outer plexiform layer, INL: inner nuclear layer, IPL: inner plexiform layer, GCL: ganglion cell layer.

to both naïve (IOP = 14mmHg+/-1mmHg) and saline-injected controls, respectively (**Figure 2.3B**, $p<0.05$).

Since transcriptome analysis revealed decreased expression of the $\alpha1$ subunit of the Na/K-ATPase, we then examined the localization pattern of the $\alpha1$ subunit, specifically, in retina from naïve, saline-injected and microbead-injected mice. Qualitatively, immunolabeling for $\alpha1$ Na/K-ATPase (green) was reduced in retina from microbead-injected mice, as compared to both naïve and saline-injected controls (**Figure 2.3C**), particularly in the GCL (**Figure 2.3C**, bottom panel). Quantification of immunolabeling intensity confirmed that elevated IOP decreased intensity of $\alpha1$ Na/K-ATPase by 39 and 44%, as compared to both naïve and saline-injected controls, respectively (**Figure 2.3D**, $p<0.05$). These data indicate a pressure-induced reduction in expression of the $\alpha1$ subunit of the Na/K-ATPase, particularly in the GCL.

Ocular hypertension alters expression of Kir2.1 and Kir4.1 in retina

Kir2.1 and Kir4.1 are the K^+ channels that are primarily responsible for K^+ siphoning by Müller glia.[151,153] We performed immunolabeling for Kir2.1 and Kir4.1 in retinal sections from saline-injected (IOP = 15mmHg+/-0.9mmHg) and microbead-injected (IOP = 21mmHg+/-1.1mmHg) mice. Qualitatively, immunolabeling for Kir2.1 was increased, while immunolabeling for Kir4.1 was reduced in retina from microbead-injected mice, as compared to saline-injected controls (**Figure 2.4A**). Quantification of immunolabeling intensity confirmed that elevated IOP increased intensity of Kir2.1 by 25% and decreased intensity of Kir4.1 by 32%, as compared to saline-injected controls (**Figure 2.4B**). These data suggest that elevated IOP alters K^+ siphoning machinery in the retina.

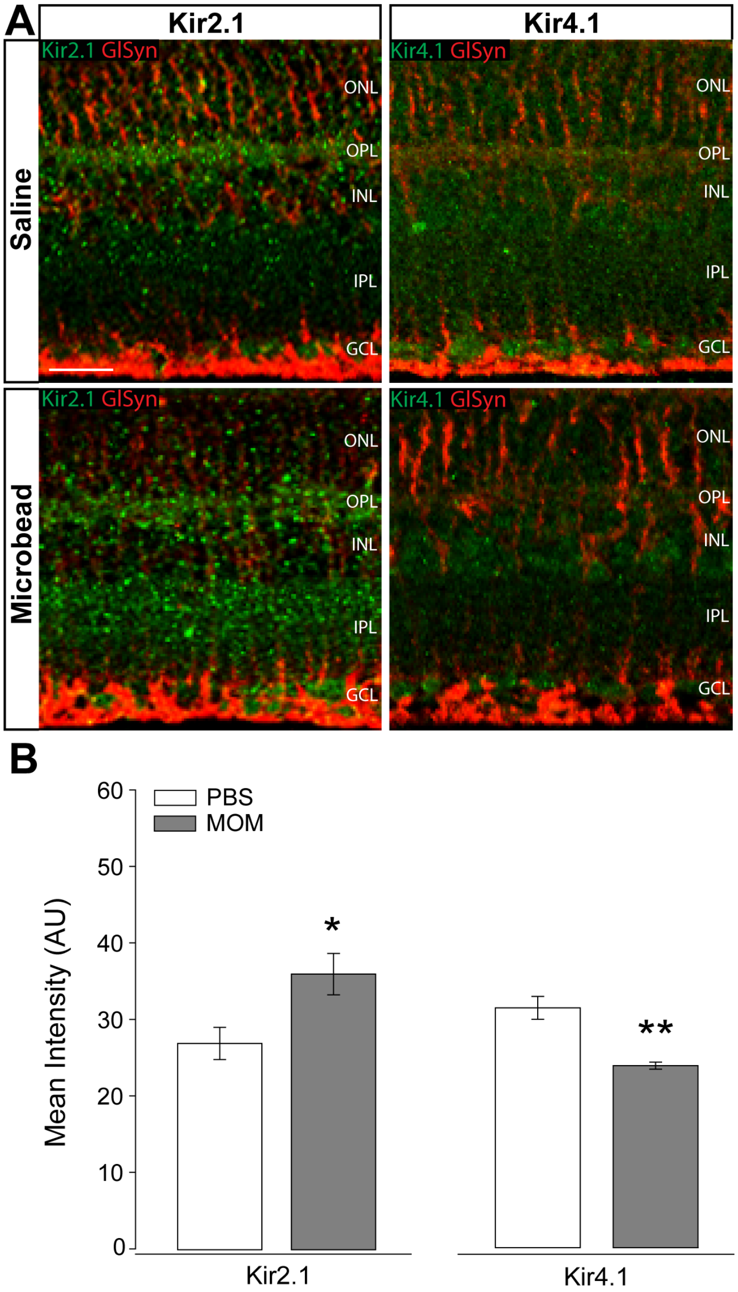

Figure 2.4. Intensity of Kir channel staining in glaucomatous retinal sections. (**A**) Images are representative fluorescent micrographs of retinal sections from saline- or microbead-injected eyes. Immunolabeling of Kir2.1 (green), Kir4.1 (green), and CD44 (red) was performed. (**B**) Bar graphs depict the mean intensity of Kir2.1 and Kir4.1 staining compared between saline and microbead retina. Kir2.1: n(PBS)=7 retina sections, n(MOM)=7; Kir4.1 n(PBS)=6, n(MOM)=7. Images taken at 40x, scale bar=20µm. Asterisks indicate $*p < 0.05$, $**p < 0.005$.
[Figure from Fischer et al. (2019) Am J Physiol Cell Physiol[177] and used in accordance with Copyright Clearance Center's RightsLink service]

Ocular hypertension alters expression of TASK-1, but not TWIK-1, in retina

K2P channels with inward rectifying capabilities, such as TWIK-1 and TASK-1, are also

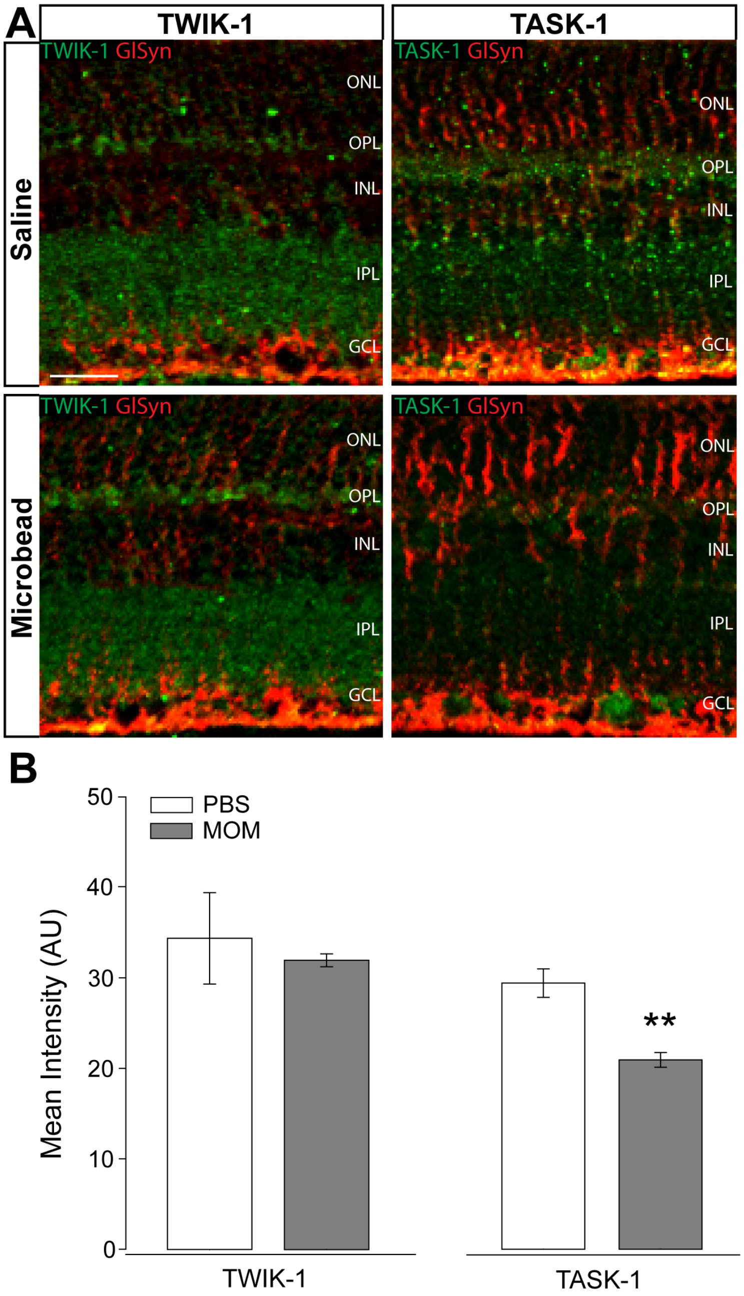

Figure 2.5. Intensity of TWIK-1 and TASK-1 channel staining in glaucomatous retinal sections. (**A**) Images are representative fluorescent micrographs of retinal sections from saline- or microbead-injected eyes. Immunolabeling of TWIK-1 (green), TASK-1 (green), and CD44 (red) was performed. (**B**) Bar graphs depict the mean intensity of TWIK-1 and TASK-1 staining compared between saline and microbead retina. TWIK-1: n(PBS)=6 retina sections, n(MOM)=7; TASK-1: n(PBS)=7, n(MOM)=7. Images taken at 40x, scale bar=20µm. Asterisks indicate $p < 0.005$.
[Figure from Fischer et al. (2019) Am J Physiol Cell Physiol[177] and used in accordance with Copyright Clearance Center's RightsLink service]

responsible for K^+ conductance in Müller glia, and contribute to K^+ siphoning alongside Kir channels.[154] We performed immunolabeling for TWIK-1 and TASK-1 in retinal sections from saline-injected and microbead-injected mice.

Qualitatively, immunolabeling for TWIK-1 did not appear to be significantly altered in retina from microbead-injected mice, as compared to saline-injected controls (**Figure 2.5A**). However, it appeared that immunolabeling for TASK-1 was reduced in retina from microbead-injected mice, as compared to saline-injected controls (**Figure 2.5A**). Quantification of immunolabeling intensity confirmed that elevated IOP did not significantly alter the intensity of TWIK-1, but did decrease intensity of TASK-1 by 40%, as compared to saline-injected controls (**Figure 2.5B**).

Ocular hypertension alters expression of TRESK, but not TREK-2 and TRAAK, in retina

Next, we profiled protein expression of the K2P channels, TREK-2, TRAAK and TRESK. We performed immunolabeling for TREK-2, TRAAK and TRESK in retinal sections from saline-injected and microbead-injected mice. Qualitatively, immunolabeling for TREK-2 and TRAAK did not appear to be significantly altered in retina from microbead-injected mice, as compared to saline-injected controls (**Figure 2.6A**). However, immunolabeling for TRESK appeared to increase in retina from microbead-injected mice, as compared to saline-injected controls (**Figure 2.6A**). Quantification of immunolabeling intensity confirmed that elevated IOP did not significantly alter the intensity of TREK-2 and TRAAK, but did decrease intensity of TRESK by 25%, as compared to saline-injected controls (**Figure 2.6B**). These combined data (**Figures 2.5 and 2.6**) suggest that elevated IOP alters expression of some inwardly rectifying K2P channels in the retina.

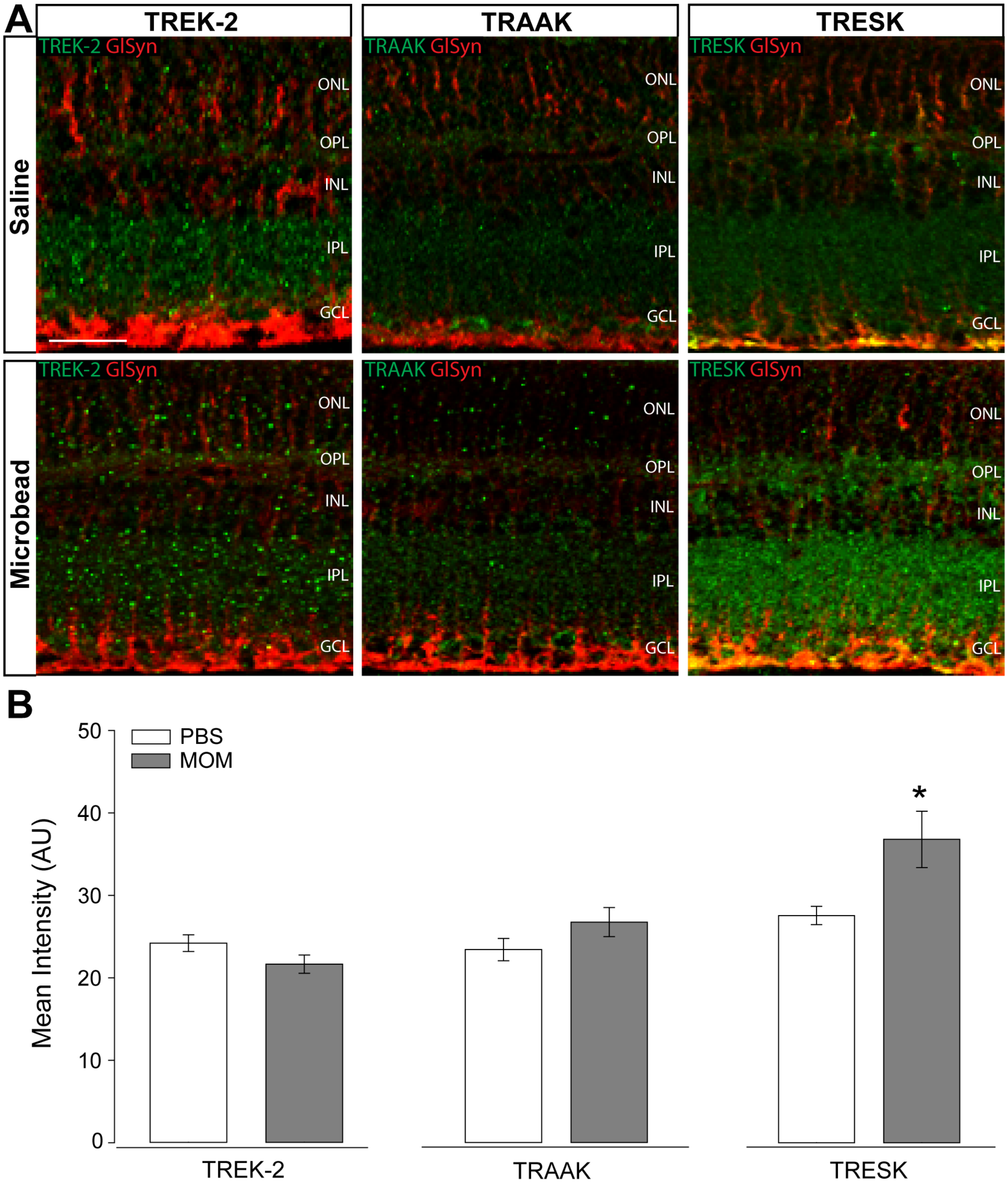

Figure 2.6. Intensity of TREK-2, TRAAK, and TRESK channel staining in glaucomatous retinal sections. (**A**) Images are representative fluorescent micrographs of retinal sections from saline- or microbead-injected eyes. Immunolabeling of TREK-2 (green), TRAAK (green), TRESK (green), and CD44 (red) was performed. (B) Bar graphs depict the mean intensity of TREK-2, TRAAK, and TRESK staining compared between saline and microbead retina. TREK-2: n(PBS)=7 retina sections, n(MOM)=7; TRAAK: n(PBS)=6, n(MOM)=7; TRESK: n(PBS)=6, n(MOM)=6. Images taken at 40x, scale bar=20µm. Asterisks indicate $p < 0.05$.
[Figure from Fischer et al. (2019) Am J Physiol Cell Physiol[177] and used in accordance with Copyright Clearance Center's RightsLink service]

Discussion

Here we sought to: 1) identify relationships between electrophysiological function and axon transport deficits in glaucomatous RGCs and 2) elucidate the pressure-dependent mechanisms underlying any such relationship. Our findings indicate that deficits in axon transport reflect measurable deficiencies in the ability of RGCs to maintain spiking frequency. This physiological phenotype appears to arise from elongation of the repolarization phase of the action potential.

There are two mechanisms in the retina by which electrochemical gradients of ions are established during the repolarization phase of the action potential. The primary means by which RGCs reset the electrochemical gradient of ions is through the action of Na/K-ATPase. A secondary means is through K^+ siphoning by Müller glia. To determine if ocular hypertension directly alters expression and function of K^+ channels in the retina implicated in maintenance of ion homeostasis, we examined changes in the expression of the Na/K-ATPase and Kir and K2P channels with inward-rectifying capabilities in the retina of mice with ocular hypertension.[16]

Whole-cell patch-clamp electrophysiology on RGCs from microbead-induced glaucomatous retina revealed that RGCs with compromised axon transport have a more depolarized resting membrane potential and diminished ability to maintain frequency of induced spiking (**Figure 2.1**). Elevation of the extracellular K^+ concentration resulted in a decrease in both the frequency and amplitude of K^+-induced spiking that was accompanied by a significant increase in the max decay slope (**Figure 2.1**). Increased max decay slope results in a slower repolarization phase of the action potential. Slower repolarization can impair the ability of the cell to continually fire action potentials, and thus explain decreases in spike amplitude and frequency noted in both current- and K^+-induced recording paradigms. This is consistent with previous studies describing decreased light-evoked spiking and depolarization of Vm in RGCs from eyes with microbead-induced ocular hypertension.[47,115,116]

The Na/K-ATPase is primarily responsible for reestablishment of electrochemical gradients of ions during the repolarization phase of the action potential. We found that 4 weeks of elevated IOP reduces gene and protein expression of both total and α1 Na/K-ATPase in retina from microbead-injected eyes (**Figure 2.2-3**). Elevated pressure *in vivo* also results in decreased transcription of a subset of Kir and K2P channels in the retina of microbead occlusion model mice (**Figure 2.2**). Immunohistochemical staining of retinal sections from mice with ocular hypertension additionally revealed altered representation of Kir and K2P channels.(**Figures 2.4-6**). As both mechanisms for maintenance of ion homeostasis show pressure-induced changes in K^+ channel expression, further analysis is required to examine the changes in expression and localization of K^+ channels in RGCs and Müller glia, specifically, as well as any disruption to ion homeostasis.

CHAPTER 3

PRESSURE-DEPENDENT MODULATION OF THE NA/K-ATPASE AND INWARD-RECTIFYING K^+ CHANNELS: IMPLICATIONS FOR CATION HOMEOSTASIS AND K^+ DYNAMICS IN GLAUCOMA[3]

Introduction

The outcomes of the studies from Chapter 2 indicate that deficits in axon transport reflect measurable deficiencies in the ability of RGCs to maintain spiking frequency and that this physiological phenotype appears to arise from elongation of the repolarization phase of the action potential. Repolarization is critically important for the reestablishment of electrochemical gradients of ions between action potentials. Ion homeostasis is maintained in the retina by the actions of the Na/K-ATPase and through K^+ siphoning by Müller glia. Here we sought to elucidate the contribution of the Na/K-ATPase and K^+ siphoning to the repolarization phenotype seen in glaucomatous RGCs.

Pressure-induced changes in expression profiles of the Na/K-ATPase, Kir, and K2P channels were seen in the retina of mice with ocular hypertension. In these studies, we assessed whether similar changes in K^+ channel expression occur in primary cultures of purified RGCs and Müller glia exposed to glaucoma-related stressors[169-173]. We additionally measured outcomes of cell health and K^+ homeostasis in RGC and Müller glia cultures.

Long-term pressure elevation in Müller glia cultures resulted in changes in expression and localization of Kir and K2P channels. Long-term pressure elevation additionally resulted in

---

[3] Portions of this chapter were published as Fischer et al. (2019) American Journal of Physiology Cell Physiology.

significant LDH release, increased extracellular concentrations of K^+, and reduced cation flux. In contrast, short-term pressure elevation only resulted in reduced cation flux. Finally, the pressure-induced decrease in cation influx can be recapitulated by treatment with a cation channel inhibitor. Modulation of K^+ siphoning machinery in Müller glia and altered cation homeostasis may have implications for electrophysiological impairment noted in RGCs of glaucomatous retina.

Both short- and long-term pressure elevation in RGC cultures resulted in changes in expression of the Na/K-ATPase. Long-term pressure elevation additionally resulted in increased extracellular concentrations of K^+ and reduced cation flux. The reduced Na/K-ATPase activity and resulting ion dyshomeostasis in RGCs was far more robust than any changes seen in Müller glia and thus is more likely to be the cause of the early electrophysiological deficits in glaucomatous RGCs. Pharmacological inhibition of the Na/K-ATPase is sufficient to replicate pressure-induced cation influx and repolarization phase phenotypes in healthy RGCs. Together, these data suggest that pressure-induced deficits in axon transport are accompanied by impaired electrophysiology function of RGCs that arises from failure to maintain electrochemical gradients. The potential for ion dyshomeostasis to act as a propagating agent for electrophysiological impairment introduces a novel possibility for etiology of spatial clustering of pathology in neighboring RGCs, with implications for spatial clustering noted in several other neurodegenerative disorders.

Materials and Methods

Isolation of primary, purified retinal ganglion cell cultures

Primary cultures of purified RGCs were prepared as previously described.[169,172,173,178] Briefly, RGCs were purified by immunomagnetic separation, using mouse anti-rat Thy-1.1/Cd90 IgG antibody (5µg/mL, Cat# 554895, BD Biosciences, San Jose, CA) and metallic microbeads conjugated to anti-mouse IgG secondary antibody (Cat# 130-047-102, Miltenyi Biotec, Auburn, CA). RGCs were plated in 8-well chamber slides coated overnight with laminin (0.01 mg/mL; Cat# L6274, Sigma). RGCs were grown in serum-free, Neurobasal A media (Cat# 21103049, Gibco, Carlsbad, CA), containing the following supplements: 2% B27 (Cat# 17504044, Gibco), 1% N2 (Cat# 17502048, Gibco), 2 mM L-glutamine (Cat# G7513, Sigma), 100µM inosine (Cat# 58-63-9, Sigma), 0.1% gentamycin (Cat# 15710-064, Gibco), 50 ng/mL brain-derived nerve growth factor (Cat# PHC7074, Gibco), 20 ng/mL ciliary neurotrophic factor (Cat# PRC7015, Gibco), 10 ng/mL basic fibroblast growth factor (Cat# 13256-029, Gibco). Experiments were performed on RGCs approximately 1 week after plating. The following drugs used for cell culture experiments were dissolved in the culture media and used at designated concentrations: ouabain (20 µM, Cat# O3125, Sigma Aldrich), bisindolylmaleimide I (10 µM, Cat# 176504-36-2, Millipore Sigma, Burlington, MA), and MG-132 (20 µM, Cat# 133407-82-6, Millipore Sigma).

Isolation of primary, purified Müller glia cultures

Cultures of primary, purified Müller glia were prepared as previously described.[169] Briefly, Müller glia were isolated by immunomagnetic separation, using mouse anti-CD44 IgG antibody (16ug/ml, Cat# MA5-16909, Invitrogen, Carlsbad, CA) and metallic microbeads conjugated to anti-mouse IgG secondary antibody (Cat# 130-047-102, Miltenyi Biotec, Auburn, CA). Müller glia were plated in 8-well chamber slides and grown in DMEM/F12 (Cat# 11330-032, Gibco, Carlsbad, CA) containing 1% G5 supplement (Cat# 17503012, Gibco), 0.1% gentamycin (Cat# 15710-064, Gibco), and 10% fetal bovine serum (Cat# 16140071, Gibco). Experiments were performed approximately 1-2 weeks after plating. The drug, fluoxetine, used for thallium flux experiments was dissolved in the culture media and directly applied to cells (100µM, Cat# F132, Sigma-Aldrich, St. Louis, MO).

Elevated hydrostatic pressure in culture to induce glaucoma-related stressors

Cultures of primary, purified RGCs and Müller glia were maintained at ambient or at +70 mmHg hydrostatic pressure, for 4 or 48 hours, as previously described.[169-173] Briefly, a humidified pressure chamber equipped with a regulator and gauge was placed in a 37°C incubator; a mixture of 95% air and 5% CO2 was pumped into the chamber to obtain a pressure of +70 mmHg (9% increase above atmospheric pressure), which was maintained by the regulator. For ambient pressure experiments, cells were kept in a standard incubator.

Apoptosis assay

In RGC and Müller glia cultures exposed to ambient or elevated pressure for 4 or 48 hours, we measured apoptosis with TdT-mediated dUTP-X nick end labeling (TUNEL; Cat# 12156792910, Roche, Basel, Switzerland). Labeling was performed according to manufacturer's specifications and as previously described.[169,172,179,180] Cells were counterstained with mouse anti-β-TubulinIII (2ug/ml, Cat# 801201, BioLegend) to label RGCs or with rat anti-CD44 (6.7ug/ml, Cat# 14-0441, Invitrogen) to label Müller glia for confirmation of cell type and DAPI for quantification of total cell density. To quantify % TUNEL+ cells, 20X images were taken using a Roper Scientific black and white camera (Photometrics, Tucson, AZ) mounted to a Nikon Ti microscope (Nikon Instruments, Melville, NY). 5 images were taken per well, across 4 wells per condition. Total number of β-TubulinIII+/DAPI+ and TUNEL+/β-TubulinIII+/DAPI+ were counted for each image and summed for each well. Data is shown as % TUNEL+ cells relative to the total number of β-TubulinIII+/DAPI+ cells, normalized as the percent change from control (ambient pressure). Total number of CD44+/DAPI+ and TUNEL+/ CD44+/DAPI+ were counted for each image and summed for each well. Data is shown as % TUNEL+ cells relative to the total number of CD44+/DAPI+ cells.

Cytotoxicity assay

In RGC and Müller glia cultures maintained at ambient or elevated pressure for 4 or 48 hours, we measured cell toxicity, which is related to necrotic cell death, using a lactate dehydrogenase (LDH) assay (Cat# G1780, Promega, Madison, WI). The assay was performed according to manufacturer's specifications and as previously described.[172] Briefly, culture supernatant was collected following pressure elevation and immediately frozen at -80°C. The concentration of LDH in culture supernatants was determined by enzymatic reaction and measurement of optical density (OD) at 490nm. All samples were run in triplicate and OD levels were averaged. Background OD levels were obtained from blank media samples and subtracted from OD levels of experimental samples. Data is shown as OD at 490nm with background subtracted.

Immunocytochemistry

We assessed expression and localization patterns of K^+ channel expression using immunocytochemistry.[169-173] Immunocytochemistry experiments were done on RGC and Müller glia cultures exposed to ambient or elevated pressure for 48 hours. Cells were fixed in 4% paraformaldehyde (Cat# 15714-S, Electron Microscopy Sciences, Hatfield, PA) for 15 minutes at room temperature and washed with 1X PBS. Samples were incubated in blocking solution containing 5% normal horse serum (NHS; Life Technologies) and 0.1% Triton-X (Fisher Scientific) in 1X PBS. Samples were incubated in blocking solution containing 5% normal horse serum (NHS; Life Technologies) and 0.1% Triton-X (Fisher Scientific) in 1X PBS. Samples were then incubated overnight at 4°C in primary antibody solution (3% NHS and 0.1% Triton X-100 diluted in 1X PBS) containing: rabbit anti-Total Na/K-ATPase (2ug/ml, Cat# ab58475, Abcam, Cambridge, UK), rabbit anti-α1 Na/K-ATPase (2.85ug/ml, Cat# ANP-001, Alomone, Jerusalem, Israel), mouse anti-β-TubulinIII (2ug/ml, Cat# 801201, BioLegend, London, UK), rabbit anti-Kir2.1 (5ug/ul, Cat# APC-026, Alomone Labs, Jerusalem, Israel), rabbit anti-Kir4.1 (2ug/ml, Cat# APC-035, Alomone Labs), rabbit anti-TRAAK (5ug/ml, Cat# APC-108, Alomone Labs), rabbit anti-TRESK (5ug/ml, Cat# APC-122, Alomone Labs), rabbit anti-TREK2 (5ug/ml, Cat# APC-055, Alomone), rabbit anti-TASK1 (5ug/ml, Cat# APC-024, Alomone), rabbit anti-TWIK1 (5ug/ml, Cat# APC-110, Alomone), and rat anti-CD44 (6.7ug/ml, Cat# 14-0441, Invitrogen). Following 1X PBS washes, samples were incubated for 2 hours at room temperature in a secondary antibody solution containing: 1% NHS, 0.1% Triton X-100 and 647-donkey anti-mouse (7.5ug/ml; Cat# 715-606-150, Jackson ImmunoResearch), 647-donkey anti-rat (7.5ug/ml; Cat# 712-605-153, Jackson ImmunoResearch), or 488-donkey anti-rabbit (7.5ug/ml; Cat# 711-546-152, Jackson ImmunoResearch) in 1X PBS. Samples were counterstained with the nuclear stain DAPI (50ug/ml; Cat# D1306, Life Technologies) and coverslipped in aqueous mounting media (Southern Biotech, Birmingham, AL). Immunolabeling was imaged at 20X, 40X, or 60X using an Olympus FV-1000 inverted confocal microscope (Olympus, Tokyo, Japan). Mean fluorescence intensity was calculated using the FIJI Color Histogram tool (ImageJ).

Quantitative RT-PCR

RNA was isolated from Müller glia cultures exposed to 4 or 48 hours of ambient or elevated pressure, using RNeasy Micro Kit (Cat# 74004, Qiagan, Valencia, CA), according to the manufacturer's instructions. cDNA synthesis was performed with iScript cDNA Synthesis Kit (Cat# 170889, BioRad, Hercules, CA), according to the manufacturer's instructions. PCR was performed with a 7300 Real-Time PCR System (Applied Biosystems, Foster City, CA) using FastStart Universal SYBR Green Master (ROX) Kit (Cat# 04913850001, Roche, Basel, Switzerland) together with 25ng template DNA and the following primer concentrations: *Kcnj6* = 500nM, *Kcnj12* = 500nM, *Kcnj14* = 700nM, *Kcnk1* = 500nM, *Kcnk3* = 800nM, *Kcnk12* = 300nM, *Gapdh* = 500nM, in 50µl final volume. Initial denaturation for 10 min at 95°C was followed by 40 cycles of amplification (95°C for 15 s and 60°C for 60 s) and melting curve analysis for 15 s at 95°C, 30 s at 60°C, and 15 s at 95°C. We used primer sequences utilized in studies found in the literature for the following genes: *Kcnj6*[181], *Kcnj12*[182], *Kcnj14*[183], *Kcnk1*[184], *Kcnk3*[184], *Kcnk12*[185], and *Gapdh*[185]. All products reported correspond to well-defined single peaks in the melting curve. No such peaks were observed in the absence of the template. The results were analyzed using the 7300 System SDS software (Applied Biosystems). C_t (threshold cycle) values were calculated by setting the threshold in the linear phase of the amplification curve. All the samples were run in triplicate and C_t values shown are the mean of the three values, normalized to the control gene, *Gapdh*.

Thallium Flux Imaging

We assessed ion channel activity in live RGC or Müller glia cultures exposed to 4 or 48 hours of ambient or elevated pressure by thallium flux imaging, as previously described.[186] Thallium flux indirectly measures inward ion flux, through the fluorescence intensity of Thallos dye. Briefly, cells were loaded with Thallos-AM dye (0.5 µg/µL, Cat# 0902, TEFlabs, Austin, TX), generously provided by Dave Weaver of Vanderbilt University. Cells were loaded with dye by incubating for 30 minutes at 37°C. Following dye loading, cells were washed with fresh media. Using live cell fluorescence microscopy, the baseline fluorescence of the Thallos dye was recorded for continuously 6-8 seconds (images taken every 1 second). 1mM thallium (TI^+) solution was added to cell culture media and live imaging was performed continuously for 45 seconds (images taken every 1 second). The fluorescence intensity of each cell was calculated for each image using Nikon NIS-Elements software. Data was plotted as normalized fluorescence intensity at each time point.

Inductively Coupled Plasma Mass Spectrometry

We measured the extracellular concentration of K^+ in supernatants from RGC and Müller glia cultures exposed to 4 or 48 hours ambient or elevated pressure using inductively coupled plasma mass spectrometry (ICP-MS). Experiments were performed through the Mass Spectrometry Research Center at Vanderbilt University. Culture supernatants were diluted 1000X with Milli-Q water (Millipore, Milli-Q synthesis advantage A-10, Millipore Corp., Mass., U.S.A) and prepared alongside a calibration curve made utilizing the same water. K^+ standards (Fluka, Sigma-Aldrich, L'Isle-d'Abeau Chesnes, Saint-Quentin Fallavier, France) were serially diluted for the calibration curve, which ranged from 10ppm to 1ppb. Samples and standards were immediately analyzed by ICP-MS on an Agilent model 7700_X (Agilent Technologies, Santa Clara, CA,). Each sample was introduced to the instrument manually and the probe was rinsed in 2% nitric acid (Optima grade, Fisher Scientific Co., Pittsburgh, PA, USA) between each sample. Three blank samples of pure Milli-Q water between introduction of standards and samples confirmed the absence of background K^+. The data were analyzed with an offline data analysis package (Agilent Technologies), where the calibration curve was plotted linearly and both R^2 values, as well as detection limits, were calculated. The calculated concentrations of each sample were multiplied by 1000 to account for the initial dilution factor. The data is shown as average K^+ concentration in parts per million (ppm).

Electrophysiology in Müller glia cultures

Cultured Müller glia were targeted for intracellular recordings. The culture medium was exchanged with an extracellular solution containing (in mM) 140 NaCl, 5 KCl, 2 $CaCl_2$, 2 $MgCl_2$, 10 Hepes, 10 dextrose, adjusted to a pH of 7.4 with NaOH (290 osm). Intracellular recording pipettes were pulled from thick-walled borosilicate glass and filled with (in mM) 130 KCl, 10 NaCl, 0.5 $CaCl_2$, 2 $MgCl_2$, 5 EGTA, 10 Hepes, 3 Na_2-ATP adjusted to pH 7.2 with NaOH (280 osm). Recording pipettes had a resistance between 8-11 MΩ. External and internal solutions were the same as used by Ruiz-Ederra et al.[187] to investigate retinal cultured Müller cell physiology. Electrophysiological recordings were performed at room temperature (23°C). Müller glia were viewed using an upright microscope (Olympus BX51, 40X) under differential interference contrast (DIC), using a CCD (charge-coupled device) camera (Andor). The recording pipette was positioned near a cell, using a micromanipulator, and the potential difference between intracellular and extracellular solutions was subtracted online. The recording pipette was then positioned onto a cell, forming a tight seal (> 1 GΩ) between the recording pipette and cultured RGC. Then, brief negative pressure pulses were applied to break into cells to form a whole-cell configuration (access resistance typically < 50 MΩ) and voltage clamped at -80 mV. We then measured currents produced by brief, 40 ms voltage steps from -150 to +30 mV in +10 mV increments. Current was averaged across cells for each voltage step and compared between conditions. Analog electrical activity was obtained (Multiclamp 700B, Molecular Devices), digitized (sampling rate 50 kHz, Digidata 1550A, Molecular Devices), and analyzed using Clampfit 10.6 (Molecular Devices).

Electrophysiology in whole, intact retina

Mice were housed in accordance with NIH guidelines and maintained on a 12-hour light/dark cycle with free access to food and water. All experiments were approved by the Institutional Animal Care and Use Committee of Vanderbilt University Medical Center. C57Bl/6 mice were obtained from Charles River Laboratories (Wilmington, MA).

Anesthetized animals received bilateral injections of 1.5µL of saline. 48 hours prior to electrophysiology experiments, mice received a bilateral, intravitreal injection of the neural tracer cholera toxin beta subunit to label RGCs. Whole-cell recording was performed, as previously described.[47] Under dim red light (630 nm, 800 µW/cm^2, Ushio FND/FG), animals were euthanized by cervical dislocation, and retinas were dissected out of the orbit. Whole retinas were mounted onto a physiological chamber and perfused with carbogen-saturated Ames' medium, supplemented with 20 mM glucose (pH 7.4, 290 Osm), at a rate of 2 mL/min, heated to 32°C (TC-344C, Warner Instruments). Patch pipettes were fabricated from thick-walled borosilicate glass and heat-pulled (P-2000, Sutter Instruments). Pipettes were loaded with (in mM) 125 K-gluconate, 10 KCl, 10 HEPES, 10 EGTA, 4 Mg-ATP, 1 Na-GTP, and 1 Lucifer Yellow (pH 7.35, 287 Osm), and had a resistance between 4-8 MΩ. We targeted RGCs with large somas (>15 μm in diameter) for whole-cell recording. Whole-cell voltage signals were amplified (Multiclamp 700B, Molecular Devices) and digitized at a sampling rate of 50 kHz (Digidata 1550A, Molecular Devices). Throughout each experiment, access resistance was continually monitored and was less than 30 MΩ.

We performed whole-cell current-clamp (0 pA) recordings from RGCs while applying ouabain (10 or 20 μM, Cat# O3125, Sigma Aldrich, St Louis, MO) via a wide-bore pipette attached to pneumatic microinjection device (PicoSpritzer II, General Valve Corp.). The "puff" pipette was positioned approximately 150-200 μm from the RGC soma and 10 or 20 μM ouabain, which was dissolved in extracellular medium, was administered for 30 ms at 10-12 psi while recording the drug-induced spike activity and membrane potential. After each experiment, the drug was thoroughly washed out with extracellular solution.

Statistical analysis

All statistical tests were conducted with SigmaPlot (Systat Software Inc., San Jose, CA). Experimental groups were compared within time points by student's t-test. Normality (Shapiro-Wilk) and equal variance was also assessed for each comparison. Comparisons between time points within groups were assessed by one-way ANOVA followed by pairwise comparison by either the Tukey or Dunn's method. Significant comparisons marked by brackets and asterisks. For all analyses, $p \leq 0.05$ was considered statistically significant.

Results

Long-term pressure elevation induces apoptosis in RGCs and cytotoxicity in Müller glia

In order to assess the impact of glaucoma-related stressors on the overall health of primary, purified RGCs and Müller glia, we exposed cultures to ambient or +70mmHg hydrostatic pressure for either 4 or 48 hours. We then measured apoptosis and cytotoxicity using TUNEL labeling and an LDH assay, respectively. Consistent with previous studies[172], exposure to elevated pressure for 48 hours induces apoptotic, but not necrotic, death of RGCs, as measured by TUNEL and LDH assays (**Figure 3.1**). However, exposure to only 4 hours of elevated pressure does not induce either apoptotic or necrotic death of RGCs (**Figure 3.1**).

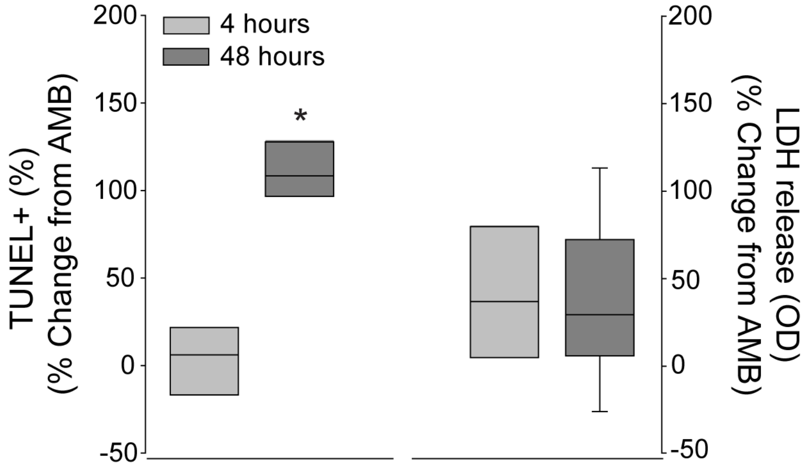

Figure 3.1. Long-term pressure elevation induces apoptosis, but not cytotoxicity in RGCs *in vitro*. (**Left**) Apoptotic death of RGCs exposed to 4 or 48 hours of ambient or elevated pressure, as measured by TUNEL assay. Percentage of TUNEL-positive RGCs following pressure elevation depicted as the percent change compared to ambient pressure. Asterisk indicates $p < 0.05$. n = 4 per condition (combined 5 images at 20x / well). (**Right**) Cytotoxicity (necrotic death) of RGCs exposed to 4 or 48 hours of ambient or elevated pressure, as measured by LDH assay. Amount of LDH release in RGC culture media following pressure elevation depicted as the percent change compared to ambient pressure. n(Amb48)=6, n(Elev48)=9, n(Amb4)=7, n(Elev4)=7.

In Müller glia cultures, DIC imaging was used to analyze cell morphology and revealed no major changes that would be indicative of cell death, such as retraction of processes and swelling or shrinkage of soma, following exposure to either 4 or 48 hours of elevated pressure (**Figure 3.2A**). Accordingly, the percentage of TUNEL+ cells did not change in Müller glia cultures exposed to either 4 or 48 hours of elevated pressure, as compared to those maintained at ambient pressure ($p>0.05$; **Figure 3.2B**). However, the presence of LDH in culture media increased 2-fold in Müller glia cultures exposed to 48 hours of elevated pressure, as compared to

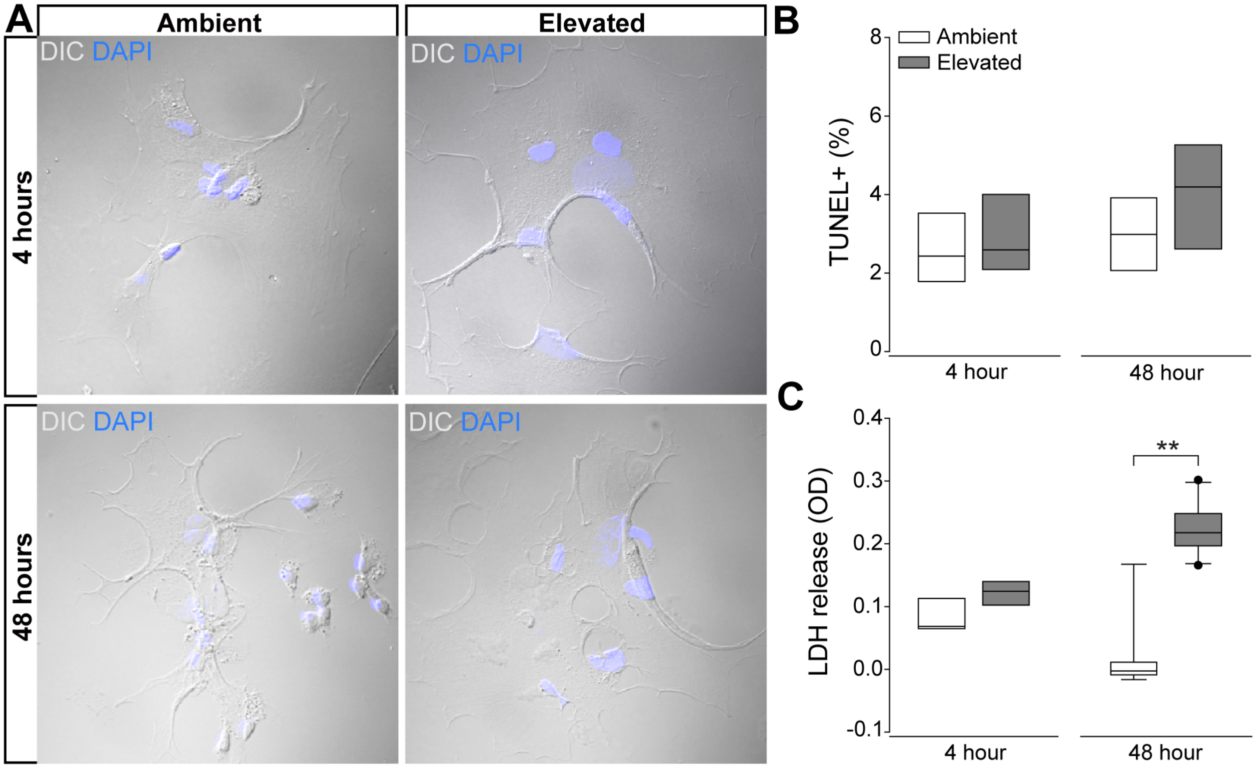

Figure 3.2. Long-term pressure elevation induces cytotoxicity, but not apoptosis in Müller glia *in vitro*. Müller glia cultures were exposed to ambient or elevated pressure for 4 or 48 hours. (**A**) Representative DIC micrographs of Müller glia from each condition. (**B**) Bar graphs depict the percentage of TUNEL-positive Müller glia compared between each condition. n = 4 wells per condition (combined 5 images at 20x / well). (**C**) Bar graphs depict the amount of LDH released in the Müller glia culture media compared between each condition. n(Amb4)=5 wells, n(Elev4)=5, n(Amb48)=15, n(Elev48)=17. Asterisks indicate $p < 0.001$.
[Figure from Fischer et al. (2019) Am J Physiol Cell Physiol[177] and used in accordance with Copyright Clearance Center's RightsLink service]

ambient pressure ($p<0.001$; **Figure 3.2C**). This pressure-induced increase in membrane permeability was not detected after 4 hours of elevated pressure ($p>0.05$; **Figure 3.2C**). Thus, exposure to ≤48 hours of elevated pressure does not induce apoptosis in Müller glia cultures. However, 48 hours of elevated pressure does increase cytotoxicity, as measured by increased membrane permeability, using the LDH assay.

Short- and long-term pressure elevation alters expression of the Na/K-ATPase in RGCs in vitro

In order to confirm cell-specific, pressure-induced changes in Na/K-ATPase expression, we immunolabeled for total and α1 Na/K-ATPase in primary, purified cultures of RGCs. RGC cultures were exposed to ambient or elevated pressure for 4 or 48 hours. At ambient pressure, immunolabeling for both total and α1 Na/K-ATPase was most prevalent in the RGC soma (**top panels; Figure 3.3A,B**). Qualitatively, exposure to both 48 and 4 hours of elevated hydrostatic pressure reduces the intensity of immunolabeling for total and α1 Na/K-ATPase in both the soma and neurites (**bottom panels; Figure 3.3A,B**). Quantification of immunolabeling intensity per cell revealed that 48 hours of elevated hydrostatic pressure decreased total Na/K-ATPase immunolabeling intensity by 45% and α1 Na/K-ATPase by 45%, as compared to 48 hours of ambient pressure (**Figure 3.3C**, $p<0.05$). Similarly, 4 hours of elevated pressure decreased total Na/K-ATPase by 46% and α1 Na/K-ATPase by 35%, as compared to 4 hours of ambient pressure (**Figure 3.3D**, $p<0.05$). These data confirmed that elevated pressure decreases Na/K-ATPase expression specifically in RGCs. Furthermore, significant decreases in Na/K-ATPase expression were seen following only 4 hours of pressure elevation, which occurs prior to the initiation of apoptosis. This suggests that pressure-induced reduction in expression of the Na/K-ATPase occurs initially via modulation of existing Na/K-ATPase protein.

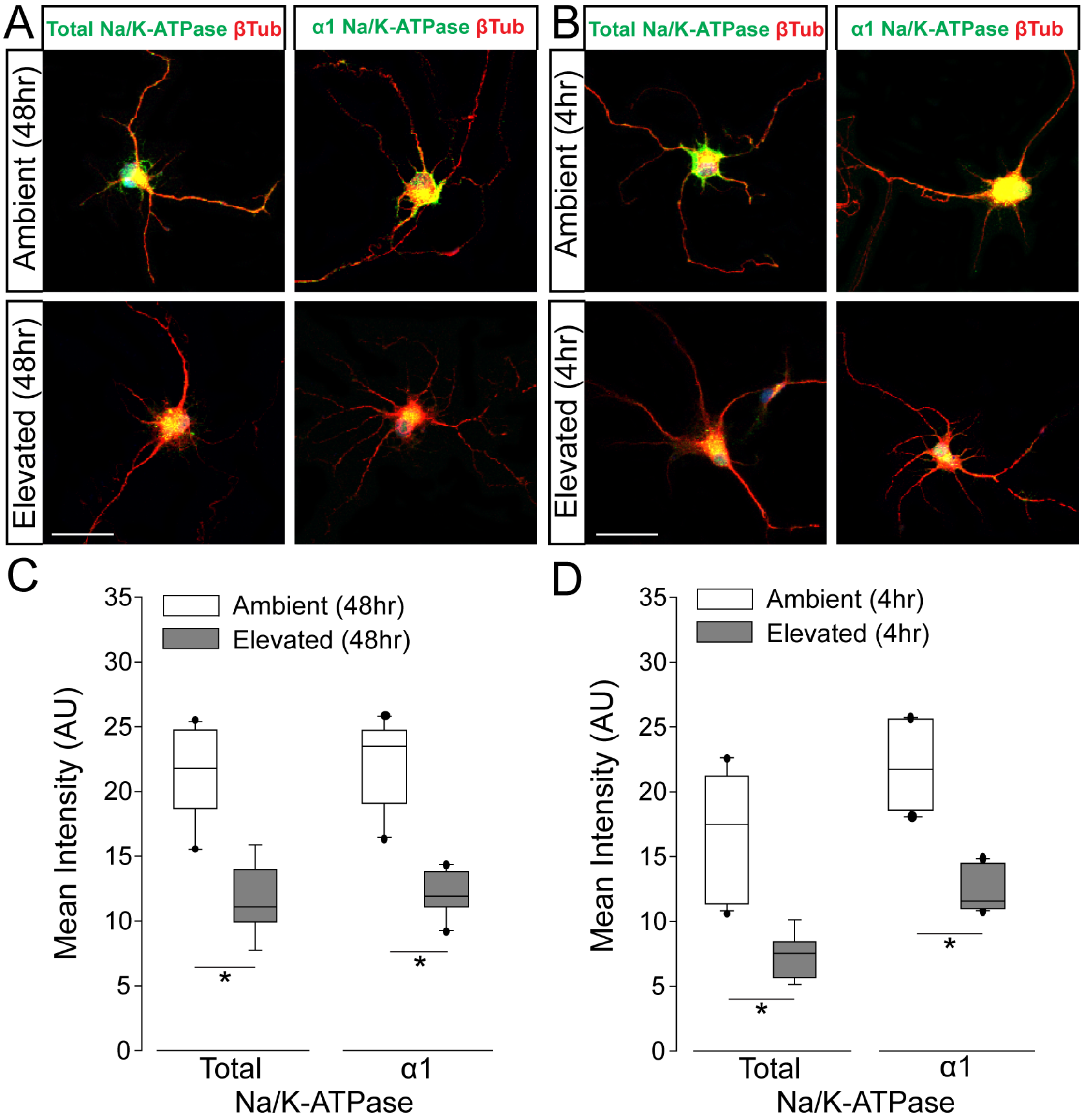

Figure 3.3. Elevated pressure decreases expression of total and α1 Na/K-ATPase in RGCs *in vitro*. (**A**) Representative fluorescent micrographs of total and α1 Na/K-ATPase (green) and β-Tubulin (red) immunolabeling in primary cultures of purified RGCs exposed to ambient or elevated pressure for 48 hours. Scale bar = 40µm. (**B**) Representative fluorescent micrographs of total and α1 Na/K-ATPase (green) and β-Tubulin (red) immunolabeling in primary cultures of purified RGCs exposed to ambient or elevated pressure for 4 hours. Scale bar = 40µm. (**C**) Mean intensity (arbitrary units; AU) of total (left) and α1 (right) Na/K-ATPase staining in RGC cultures following a 48-hour exposure to ambient or elevated hydrostatic pressure. Asterisk indicates $p < 0.05$. Total: n(Amb48)=10, n(Elev48)=9; α1: n(Amb48)=13, n(Elev48)=11. (**D**) Mean intensity (arbitrary units; AU) of total (left) and α1 (right) Na/K-ATPase staining in RGC cultures following a 4-hour exposure to ambient or elevated hydrostatic pressure. Asterisk indicates $p < 0.05$. Total: n(Amb4)=14, n(Elev4)=9; α1: n(Amb4)=10, n(Elev4)=10.

Elevated Pressure Does Not Alter Expression of Kcnk1 and Kcnk3 in Müller glia in vitro

Changes in a single population of cells (i.e. Müller glia) may not be sufficient for detection in the context of whole retina. We therefore utilized primary, purified cultures of Müller glia to examine Müller glia-specific changes in K^+ channel expression. To determine whether decreased transcription of Kir and K2P channels noted in whole retina (**Figure 2.2**) are attributable to Müller glia specifically, we performed qPCR for *Kcnj6, Kcnj12, Kcnj14, Kcnk1, Kcnk3,* and *Kcnk12* on RNA isolated from primary cultures of Müller glia exposed to ambient or elevated hydrostatic pressure for 48 hours. Expression levels for *Kcnj6, Kcnj12, Kcnj14,* and *Kcnk12* were below the detectable range. Low to no expression of these channels was expected based on the literature.[127,156,188,189] *Kcnk1* and *Kcnk3* are expressed in Müller glia; however,

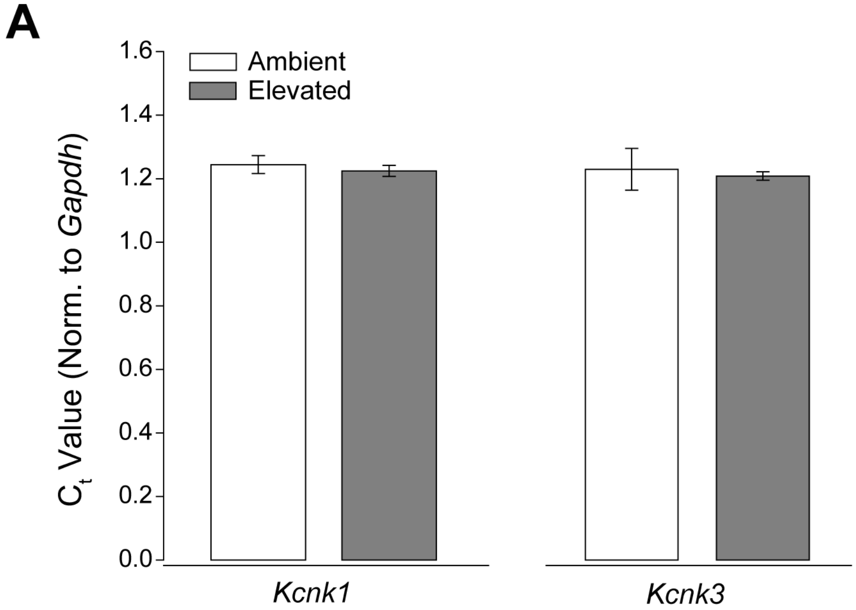

Figure 3.4. Elevated Pressure Does Not Alter Expression of Kcnk1 and Kcnk3 in Müller glia *in vitro*. (**A**) qRT-PCR was performed on RNA isolated from primary, purified cultures of Müller glia exposed to ambient or elevated pressure for 48 hours. Bar graphs of mean threshold cycle (C_t) values normalized to *Gapdh*, compared between ambient and elevated pressure for *Kcnk1* (left) and *Kcnk3* (right). n=3 for all.
[Figure adapted from Fischer et al. (2019) Am J Physiol Cell Physiol[177] and used in accordance with Copyright Clearance Center's RightsLink service]

exposure to elevated pressure does not alter expression levels, compared to ambient pressure controls (**Figure 3.4A**).

Elevated Pressure Alters Expression and Localization of Kir2.1 and Kir4.1 in Müller glia in vitro

To examine Müller cell-specific changes in expression and localization of K^+ channels, we exposed Müller glia cultures to ambient or elevated pressure for 48 hours and performed immunohistochemical analysis for Kir and K2P channels. To begin, we immunolabeled for Kir2.1 and Kir4.1. Both channels exhibited a similar localization pattern in Müller glia exposed to ambient pressure (**Figure 3.5A**). For both, Kir immunolabeling appeared to be ubiquitous with some more concentrated staining within intracellular vesicles (**Figure 3.5A**). These localization patterns are evident in the z-plane view of the images directly below the fluoromicrographs, as well as in the associated plots of fluorescent intensity below the z-plane view. This is consistent with previous studies indicating the presence of sequence motifs in Kir channels that signal export from the ER and the Golgi via adaptor proteins that initiate vesicle formation.[190,191] Ubiquitous labeling is likely attributable, in part, to plasma membrane localization, as Kir channels exist both in the plasma membrane and in vesicles trafficking to the plasma membrane.[191] Qualitatively, elevated pressure appeared to increase Kir2.1 immunolabeling, but decrease Kir4.1 immunolabeling, as compared to ambient pressure (**Figure 3.5A**). For both Kir2.1 and Kir4.1, changes in the intensity of immunolabeling were most evident in staining not associated with vesicles, suggesting that elevated pressure likely alters the cell surface representation for these channels (**Figure 3.5A**). Quantification of immunolabeling intensity confirmed pressure-induced changes in Kir channel representation. Elevated pressure increased

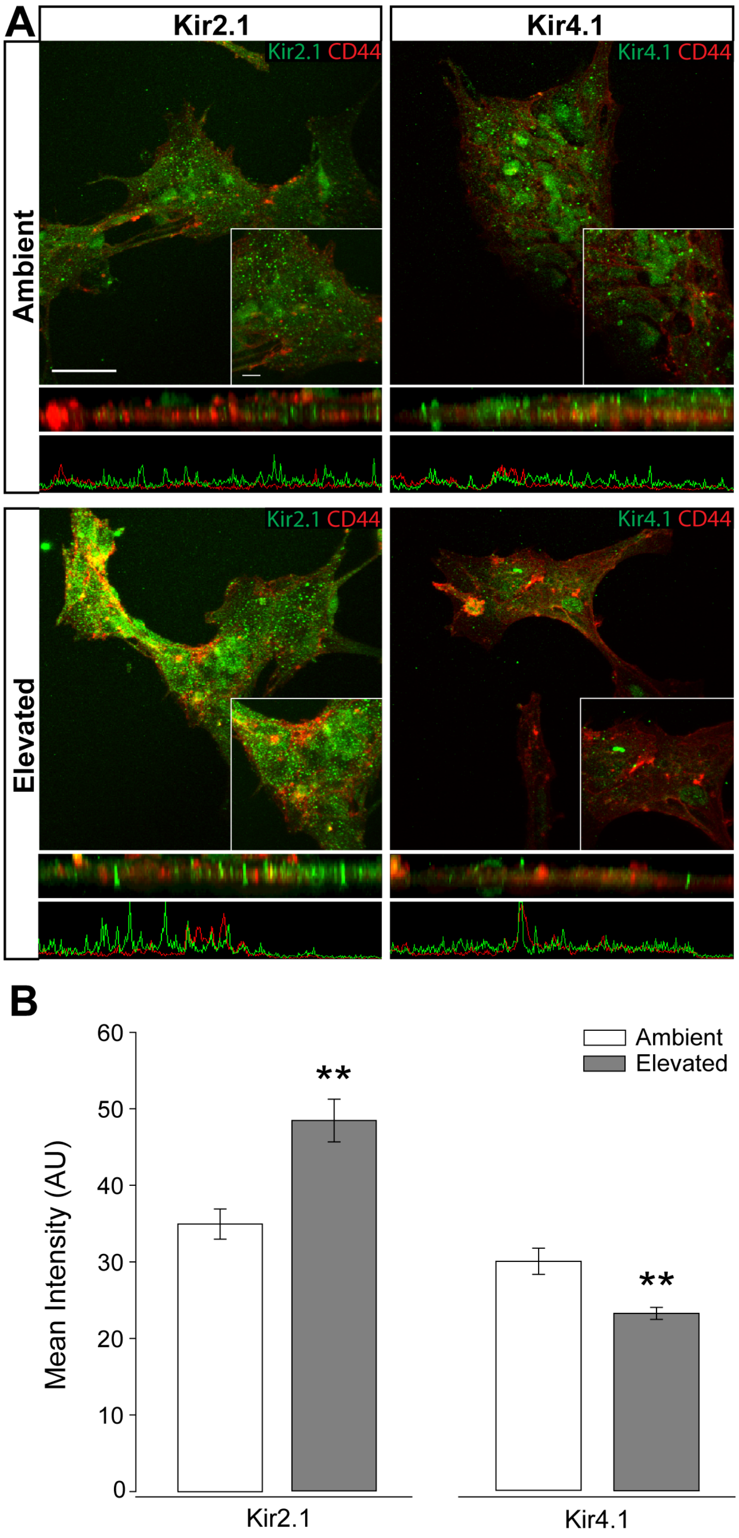

Figure 3.5. Intensity of Kir channel staining in Müller glia *in vitro* following pressure elevation. Müller glia cultures were exposed to ambient or elevated pressure for 48 hours. (A) Representative fluorescent micrographs of Müller glia from each condition. Immunolabeling of Kir2.1 (green), Kir4.1 (green), and CD44 (red) was performed. Panels below the fluoromicrographs depict a z-plane view of the

image, with associated plot of fluorescent intensity. (B) Bar graphs depict the mean intensity of Kir2.1 and Kir4.1 staining compared between ambient and elevated pressure. Kir2.1: n(Amb)=29 cells, n(Elev)=18; Kir4.1 n(Amb)=19, n(Elev)=20. Images taken at 60x, scale bar=40μm. Inset taken at 60x + 2.5x zoom, scale bar=10μm. Asterisks indicate $p < 0.005$.
[Figure from Fischer et al. (2019) Am J Physiol Cell Physiol[177] and used in accordance with Copyright Clearance Center's RightsLink service]

the labeling intensity for Kir2.1 by 28% ($p<0.001$), but decreased the intensity of Kir4.1 labeling by 29% ($p<0.005$), as compared to ambient pressure (**Figure 3.5B**). These data reflect the changes in protein expression profiles observed in retinal sections (**Figure 2.4**) and thus, support pressure-induced changes to the K^+ siphoning machinery in the retina.

Elevated Pressure Alters Expression and Localization of TASK-1, but not TWIK-1, in Müller glia in vitro

Next, we examined Müller glia-specific changes to TWIK-1 and TASK-1 protein expression and localization. Immunolabeling for TWIK-1 and TASK-1 was performed in Müller glia cultures exposed to 48 hours of ambient or elevated pressure. The TWIK-1 immunolabeling in Müller glia maintained at ambient pressure appeared to associate with circular structures (**Figure 3.6A**). These circular structures are also represented in the z-plane view of the images directly below the fluoromicrographs, as well as in the associated plots of fluorescent intensity below the z-plane view. This is consistent with previous findings indicating endosomal localization of TWIK-1 and its interaction with EFA6 on the inner surface of endosomal membranes.[162,192] In contrast, TASK-1 immunolabeling appeared more ubiquitous, with possibly some staining concentrated to vesicles (**Figure 3.6A**). This is consistent with previous findings that TASK-1 interacts with both p11 and syntaxin-8, which are associated with cell surface trafficking and endocytosis.[162,193,194] Elevated pressure did not appear to alter the localization pattern or labeling intensity of TWIK-1 (**Figure 3.6A**). However, the labeling intensity of

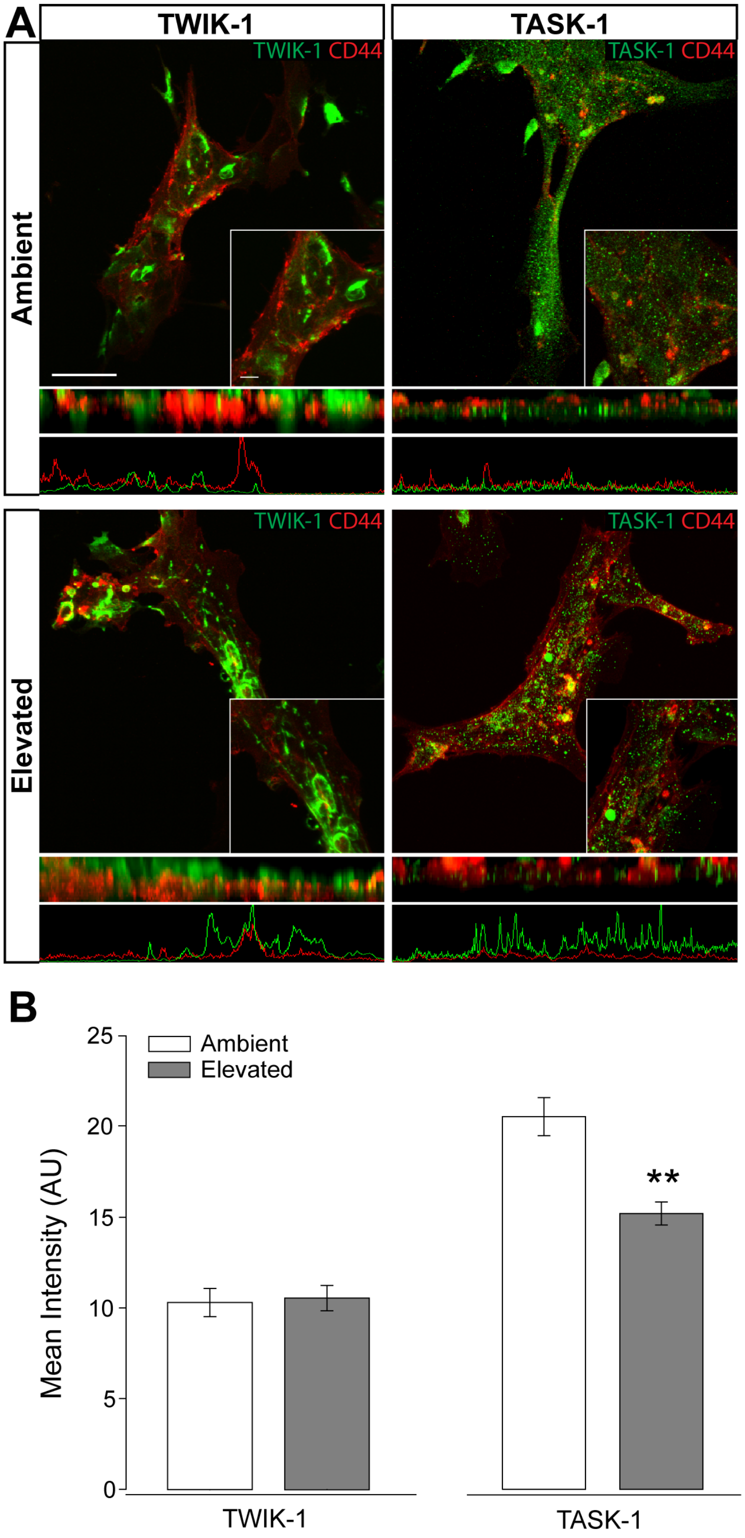

Figure 3.6. Intensity of TWIK-1 and TASK-1 channel staining in Müller glia *in vitro* following pressure elevation. Müller glia cultures were exposed to ambient or elevated pressure for 48 hours. (A) Representative fluorescent micrographs of Müller glia from each condition. Immunolabeling of TWIK-1 (green), TASK-1 (green), and CD44 (red) was performed. Panels below the fluoromicrographs are a z-

plane view of the image, with associated plot of fluorescent intensity. (B) Bar graphs depict the mean intensity of TWIK-1 and TASK-1 staining compared between ambient and elevated pressure. TWIK-1: n(Amb)=22 cells, n(Elev)=13; TASK-1: n(Amb)=21, n(Elev)=22. Images taken at 60x, scale bar=40µm. Inset taken at 60x + 2.5x zoom, scale bar=10µm. Asterisks indicate $p < 0.005$.
[Figure from Fischer et al. (2019) Am J Physiol Cell Physiol[177] and used in accordance with Copyright Clearance Center's RightsLink service]

TASK-1 appeared to decrease, particularly that with a more diffuse labeling pattern (**Figure 3.6A**). Quantification of immunolabeling intensity revealed that elevated pressure decreased TASK-1 by 35%, as compared to ambient pressure ($p<0.001$, **Figure 3.6B**). In contrast, there was no change in the intensity of TWIK-1 immunolabeling between cultures maintained at ambient or elevated pressure (**Figure 3.6B**). These data reflect the changes in protein expression profiles of TWIK-1 and TASK-1 observed in retinal sections (**Figure 2.5**) and indicate preferential regulation of the TASK-1 K2P channels in Müller glia by elevated pressure.

Elevated Pressure Alters Expression and Localization of TRAAK and TRESK, but not TREK-2, in Müller glia in vitro

Finally, we examined Müller glia-specific changes to TRAAK, TRESK, and TREK-2 protein expression and localization. We performed immunolabeling for TREK-2, TRAAK, and TRESK in Müller glia cultures exposed to 48 hours of ambient or elevated pressure. In cultures maintained at ambient pressure, TREK-2 and TRESK immunolabeling exhibited similar patterns of localization that appears to be mostly ubiquitous, with some staining concentrated to vesicles (**top panels; Figure 3.7A**). The differences in localization patterns between channels are clearly evident in the z-plane view of the images directly below the fluoromicrographs, as well as in the associated plots of fluorescent intensity below the z-plane view. This pattern of localization is consistent with the known association between microtubules and TREK-2- and TRESK-containing vesicles.[162,195] Despite similar localization patterns, the intensity of TRESK immunolabeling appeared qualitatively lower than that of TREK-2 (**top panels; Figure 3.7A**). TRAAK immunoreactivity was the lowest of the three and appeared to be concentrated primarily in vesicles (**top panel; Figure 3.7A**). Qualitatively, elevated pressure appeared to increase immunoreactivity for TRAAK and TRESK (**bottom panel; Figure 3.7A**). For TRAAK, this increase in immunoreactivity was also accompanied by a change in localization pattern from primarily vesicular to a combination of vesicular and plasma membrane (**bottom panel; Figure 3.7A**). For TRESK, the increased immunoreactivity appeared mostly associated with microtubule-like structures, which may indicate an increase in the number of TRESK-containing vesicles and/or increased trafficking of this channel (**bottom panel; Figure 3.7A**). Elevated pressure did not appear to drastically alter the intensity or localization of TREK-2 (**bottom panel; Figure 3.7A**). Quantification of immunolabeling intensity confirmed pressure-induced changes in TRAAK and TRESK representation as well as the pressure-insensitivity of TREK-2 representation. Elevated pressure increased the intensity of TRAAK immunolabeling by 24% ($p<0.05$) and of TRESK by 57% ($p<0.001$), as compared to ambient pressure (**Figure 3.7B**). As qualitatively observed, elevated pressure did not significantly alter the intensity of TREK-2 immunolabeling ($p>0.05$, **Figure 3.7B**). These data reflect the changes in protein expression profiles of TREK-1 and TRESK channels observed in retinal sections, but not of TRAAK channels (**Figure 2.6**). This suggests that the retinal milieu may be important for the regulation of these K2P channels in ocular hypertension.

Elevated pressure alters cation flux and K^+ homeostasis in RGCs in vitro

As the Na/K-ATPase is critical for maintenance of ion homeostasis, we next examined whether pressure-induced decreases in Na/K-ATPase expression are accompanied by changes in cation

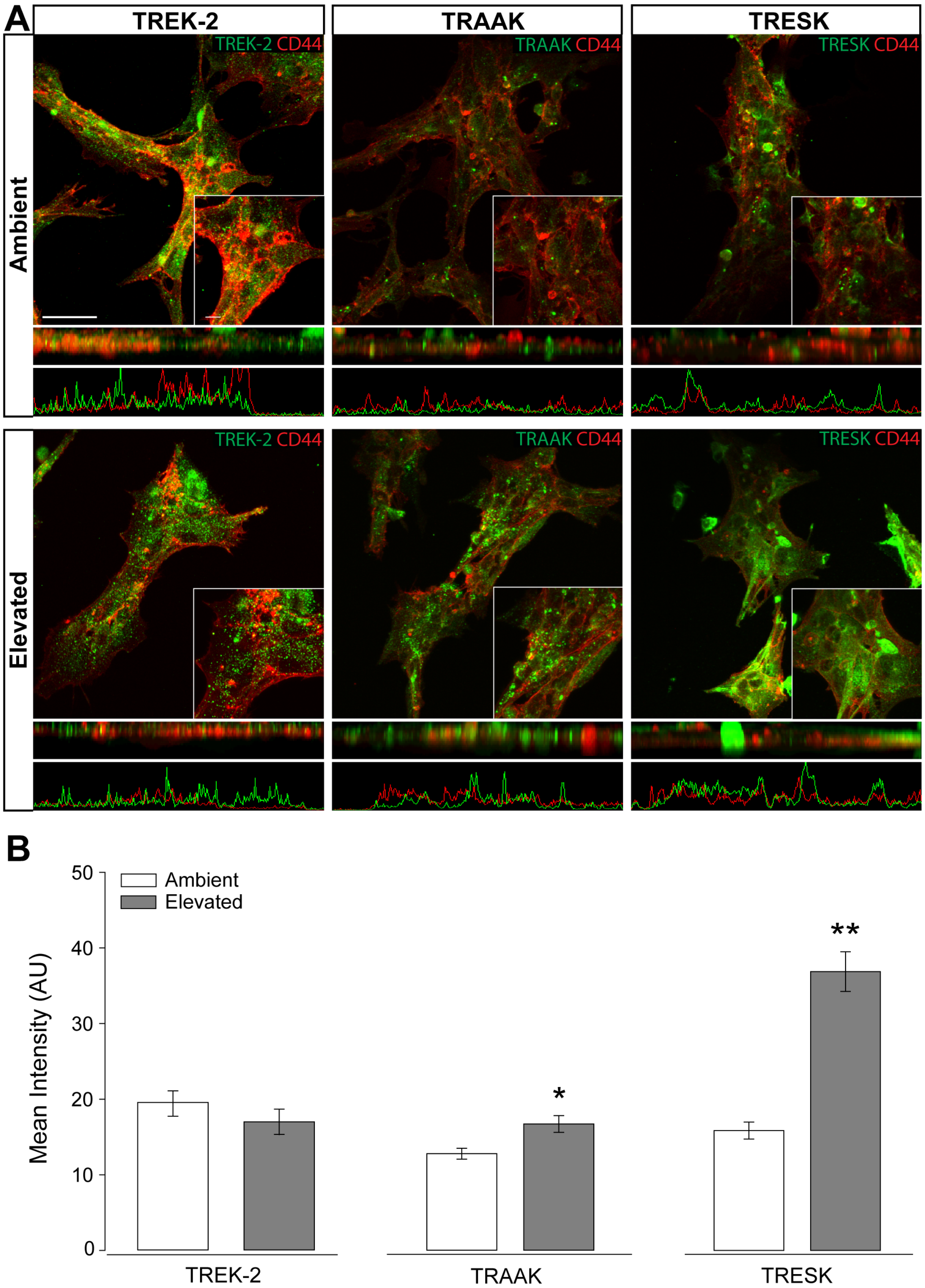

Figure 3.7. Intensity of TREK-2, TRAAK, and TRESK channel staining in Müller glia *in vitro* following pressure elevation. Müller glia cultures were exposed to ambient or elevated pressure for 48 hours. (A) Representative fluorescent micrographs of Müller glia from each condition. Immunolabeling of

TREK-2 (green), TRAAK (green), TRESK (green), and CD44 (red) was performed. Panels below the fluoromicrographs are a z-plane view of the image, with associated plot of fluorescent intensity. (B) Bar graphs depict the mean intensity of TREK-2, TRAAK, and TRESK staining compared between ambient and elevated pressure. TREK-2: n(Amb)=24 cells, n(Elev)=21; TRAAK: n(Amb)=19, n(Elev)=21; TRESK: n(Amb)=12, n(Elev)=22. Images taken at 60x, scale bar=40μm. Inset taken at 60x + 2.5x zoom, scale bar=10μm. Asterisks indicate $*p < 0.05$ and $**p < 0.005$.
[Figure from Fischer et al. (2019) Am J Physiol Cell Physiol[177] and used in accordance with Copyright Clearance Center's RightsLink service]

homeostasis. We quantified inward flux of cations in purified, primary RGCs, using real-time thallium flux imaging.[186,196] RGC cultures were loaded with Thallos dye following either 4 or 48-hour exposure to ambient or elevated pressure. After addition of thallium, fluorescence was imaged in live cells at 1-second intervals for 45 seconds. Qualitatively, fluorescent intensity of Thallos dye appears reduced in RGCs exposed to 4 or 48 hours of elevated pressure, compared to ambient controls (**Figure 3.8A**). We quantified the fluorescent intensity/cell at each one-second-time point between ambient and elevated pressure conditions after both 4 and 48-hour exposures (**Figure 3.8B**). Exposure to 4 hours of elevated pressure decreased thallium flux by 22%, as compared to 4 hours of ambient pressure ($p<0.05$; **Figure 3.8B**). By 48 hours of exposure to elevated pressure, thallium flux decreased further to 33% of that measured in the respective ambient pressure condition ($p<0.05$; **Figure 3.8B**). For RGC cultures maintained at elevated pressure, thallium flux decreased by approximately 19% between 4 and 48 hours of exposure ($p>0.05$; **Figure 3.8B**). Time in culture also slightly reduced (6%) thallium flux in RGCs maintained at ambient pressure ($p>0.05$; **Figure 3.8B**). Together, these data indicate that both short- and long-term pressure elevation reduces inward flux of cations. Furthermore, exposure time to pressure elevation appears to compound the effect, as 48 hours of elevated pressure reduced cation flux more than 4 hours of elevated pressure.

Reduced flux of cations in the cell should lead to a reciprocal increase in $[K^+]_E$. Thus, we exposed RGC cultures to ambient or elevated pressure for either 4 or 48 hours and measured

$[K^+]_E$, using ICP-MS. Exposure to 4 hours of elevated pressure did not significantly alter $[K^+]_E$, as compared to ambient pressure (**Figure 3.8C**). Consistent with our thallium flux imaging, time in culture significantly increased (34%) $[K^+]_E$ in RGCs maintained at ambient pressure ($p<0.05$; **Figure 3.8C**). Exposure to 48 hours of elevated pressure increased $[K^+]_E$ by 18.5%, as compared

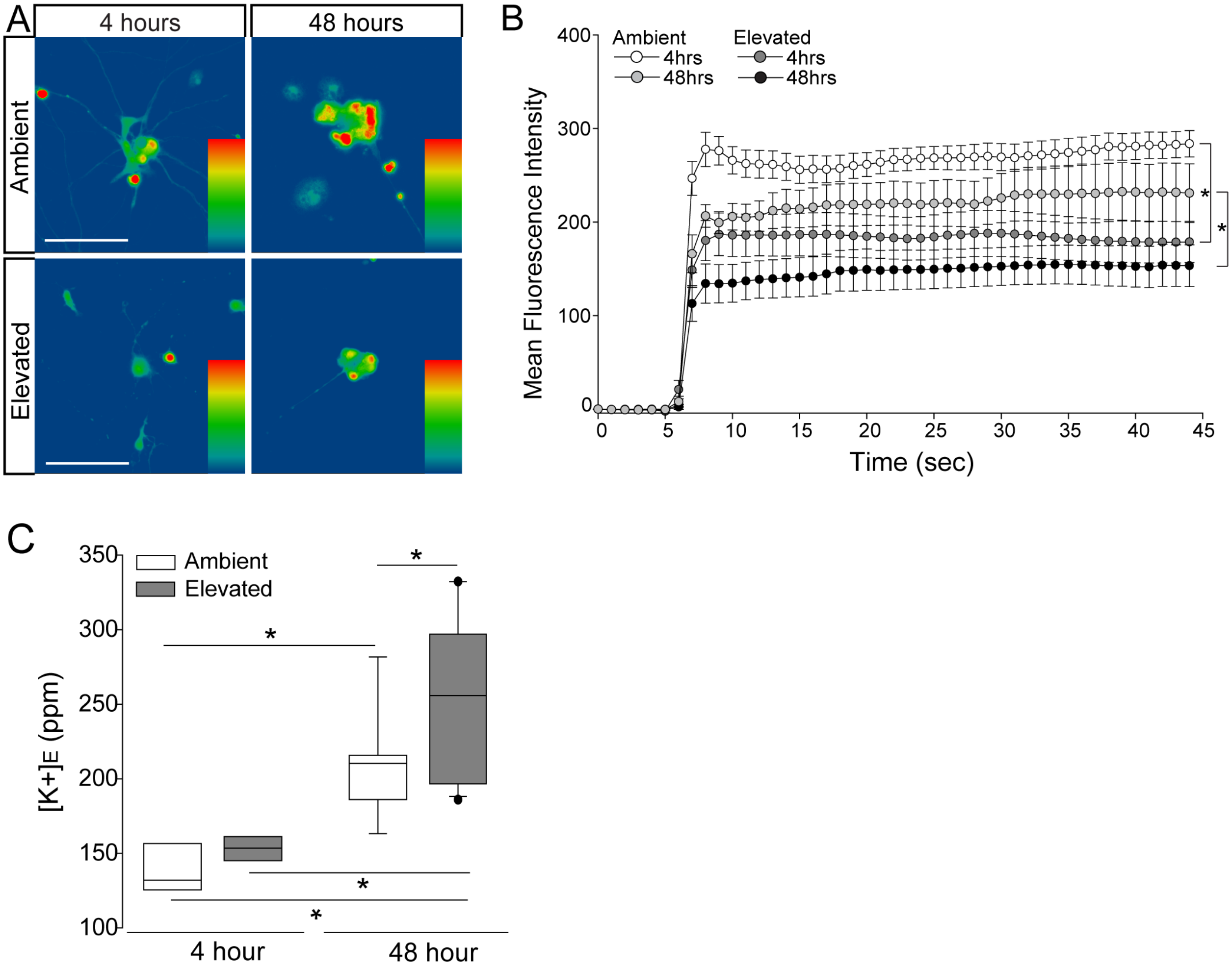

Figure 3.8. Elevated pressure decreases inward cation flux and increases extracellular K^+ concentration in RGCs *in vitro*. (**A**) Representative heat maps showing the fluorescent signal of Thallos dye in RGCs exposed to ambient (top) and elevated (bottom) pressure for 4 (left) or 48 (right) hours. Images were taken after the addition of thallium. Scale bar = 100 µM. (**B**) Line graph displaying the mean fluorescence intensity of Thallos dye over time for RGCs exposed to ambient or elevated pressure for 4 or 48 hours. Asterisk indicates $p < 0.05$ and error bars represent SEM. n(Amb4)=30, n(Elev4)=27; n(Amb48)=6, n(Elev48)=9. (**C**) Extracellular K^+ concentration in RGC culture media following 4 (left) or 48 (right) hours of ambient (white) or elevated (gray) pressure, as measured by inductively coupled plasma mass spectrometry. Asterisk indicates $p < 0.05$. n(Amb48)=9, n(Elev48)=12, n(Amb4)=7, n(Elev4)=7.

to ambient pressure at 48 hours ($p<0.05$; **Figure 3.8C**) and by 41%, as compared to elevated pressure at 4 hours ($p<0.05$, **Figure 3.8C**). These data suggest that long-term pressure-induced decreased in cation flux, like that observed after 48 hours, are necessary to significantly elevate $[K^+]_E$.

Elevated pressure alters cation flux and K^+ homeostasis in Müller glia in vitro

Next, we examined whether glaucoma-related stressors alter the cation flux and homeostasis in Müller glia. Using thallium flux imaging, we quantified inward flux of cations in purified, primary Müller glia cultures exposed to 4 or 48 hours of ambient or elevated pressure. Representative heat maps of the resultant fluorescent signal are depicted in **Figure 3.9A**. At ambient pressure, mean thallium flux decreased by 13% between 4 and 48 hour time points ($p<0.05$; **Figure 3.9B**). Exposure to 4 hours of elevated pressure decreased thallium flux by 30%, as compared to 4 hours of ambient pressure ($p<0.05$; **Figure 3.9B**). By 48 hours of exposure to elevated pressure, thallium flux decreased further to 59% of that measured in the respective ambient pressure condition ($p<0.05$; **Figure 3.9B**). For cultures maintained at elevated pressure, thallium flux decreased by approximately 50% between 4 and 48 hours of exposure ($p<0.05$; **Figure 3.9B**). Together, these data indicate that time in culture alters cation homeostasis by reducing inward cation flux. Exposure to both 4 and 48 hours of elevated pressure further reduced cation flux, where the magnitude of this decrease positively correlated with exposure time.

We then measured the $[K^+]_E$ in the culture media of Müller glia exposed to ambient or elevated pressure for either 4 or 48 hours. Exposure to 4 hours of elevated pressure did not alter $[K^+]_E$, as compared to ambient pressure (**Figure 3.9C**). In contrast, 48 hours of elevated pressure significantly increased $[K^+]_E$ by 12% ($p<0.001$, **Figure 3.9C**), as compared to ambient pressure. At elevated pressure, $[K^+]_E$ increased by 31% between 4 and 48 hours ($p<0.001$ both; **Figure 3.9C**). These data suggest that long-term pressure elevation induces K^+ dyshomeostasis in Müller glia.

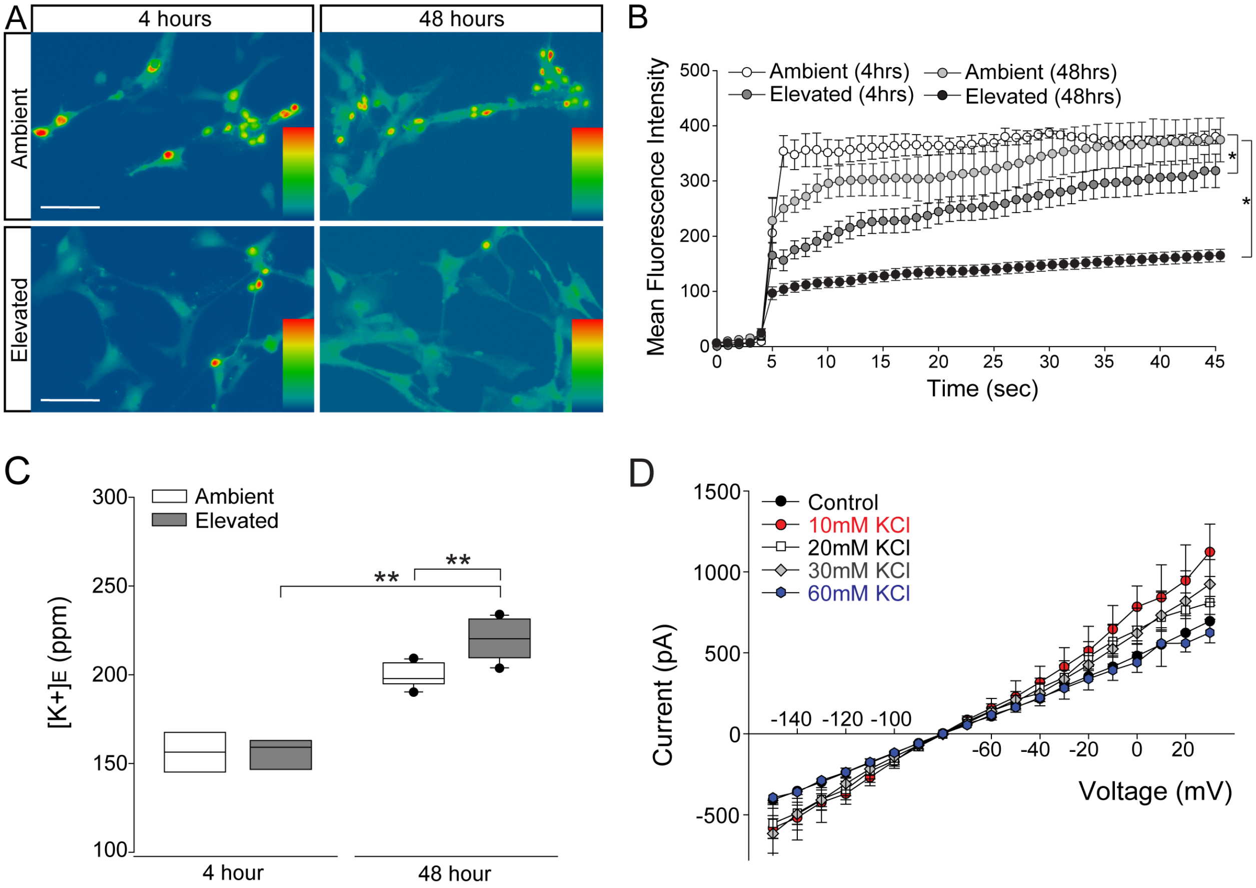

Figure 3.9. Elevated pressure decreases inward cation flux and increases extracellular K^+ concentration in Müller glia *in vitro*. (**A**) Representative heat map showing the fluorescent signal of Thallos dye in Müller glia from each condition. Images were taken after the addition of thallium. (**B**) Line graphs displaying the normalized fluorescence intensity of Thallos dyes over time for each condition. n(Amb4)=5 cells, n(Elev4)=12, n(Amb48)=5, n(Elev48)=18. Asterisks indicate $*p < 0.05$. (**C**) Box plots of the concentration of K^+ ions in the culture media of Müller glia at each condition. n(Amb4)=5 wells, n(Elev4)=4, n(Amb48)=12, n(Elev48)=12. Asterisks indicate $p < 0.001$. (**D**) Müller glia were subjected to a voltage step series from -150 to +30 mV in 10mV increments; current output was measured at each voltage step in control bath, 10, 20, 30, and 60mM [KCl] bath. n(control)=13, n(10)=3, n(20)=9, n(30)=6, n(60)=5; Asterisk indicate $p<0.05$.
[Figure adapted from Fischer et al. (2019) Am J Physiol Cell Physiol[177] and used in accordance with Copyright Clearance Center's RightsLink service]

Despite the evidence for pressure-induced alterations in cation flux and cation dyshomeostasis in Müller glia, elevating the $[K^+]_E$ of healthy Müller glia produced no changes in electrophysiological activity. Voltage clamp mode (10mV/40msec steps; -150 to +30mV) revealed no significant difference in current output from Müller glia in normal, control bath or bath containing 10, 20, 30 or 60mM of KCl ($p>0.05$, **Figure 3.9D**). These data suggest that cation dyshomeostasis is not sufficient to alter the electrophysiological properties of Müller glia.

Inhibition of cation channels alters pressure-induces changes in K^+ flux in Müller glia

To confirm whether the reduced inward cation flux seen in Müller glia exposed to elevated pressure results from altered flux through cation channels, we treated Müller glia cultures with the cation channel inhibitor, fluoxetine (100μM), while exposing them to either ambient or elevated pressure for 4 hours. Fluoxetine is a broad, nonspecific inhibitor of cation channels[197-201], which allows for testing of changes in overall membrane conductance versus membrane leakiness. Fluoxetine also specifically has been shown to inhibit several channels involved in K^+ siphoning, including Kir4.1[202] and TREK[203], which makes it a relevant tool to examine changes in cation influx for these studies. Consistent with **Figure 3.9**, 4 hours of elevated pressure decreased thallium influx by 30% in vehicle-treated cultures, as compared to those maintained at ambient pressure (**Figure 3.10A-C**). At ambient pressure, treatment with fluoxetine decreased thallium influx by 50%, as compared to vehicle treatment at ambient pressure ($p<0.05$; **Figure 3.10B,C**). Treatment with fluoxetine at ambient pressure reduced thallium influx to levels comparable to vehicle treatment at elevated pressure. Treatment with fluoxetine at elevated pressure further decreased thallium influx by 39%, as compared to vehicle treatment at elevated pressure ($p<0.05$; **Figure 3.10B,C**). These data indicate that inhibition of cation channels reduces cation influx in Müller glia cultures to an extent that is similar to pressure elevation.

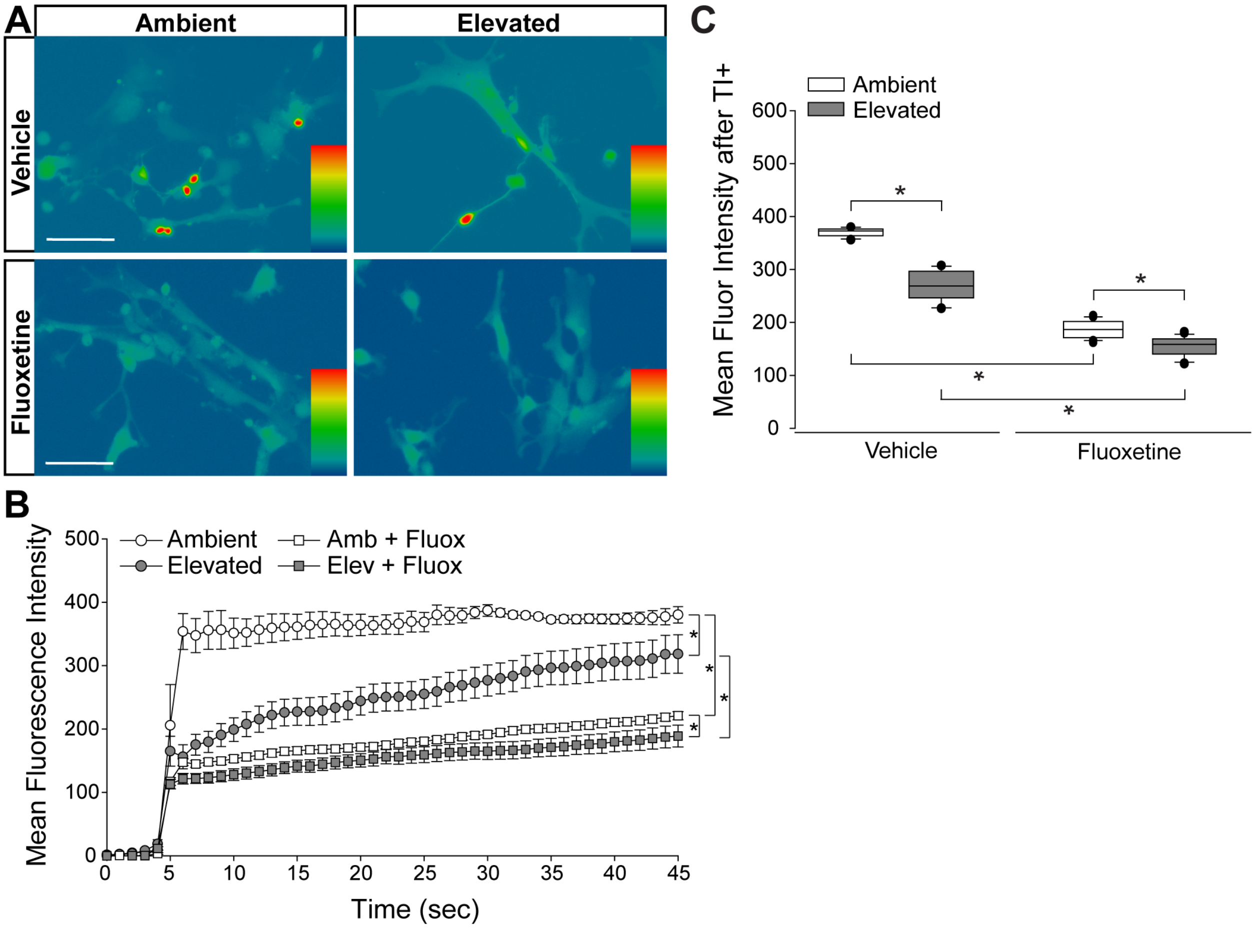

Figure 3.10. Inhibition of cation channel activity in Müller glia by fluoxetine treatment. Müller glia cultures were exposed to ambient or elevated pressure for 4 hours, in presence of vehicle or 100µM fluoxetine. (**A**) Representative heat map showing the fluorescent signal of Thallos dye in Müller glia from each condition. Images were taken after the addition of thallium. (**B**) Line graphs depict the normalized fluorescence intensity of Thallos dyes over time for each condition. Student's t-test was used to analyze statistical significance. (**C**) Box plots depict the average fluorescence intensity following addition of thallium compared between each condition. n(Amb)=5 cells, n(Elev)=12, n(Amb+Fluox)=28, n(Elev+Fluox)=22; Asterisks indicate $p < 0.05$.
[Figure from Fischer et al. (2019) Am J Physiol Cell Physiol[177] and used in accordance with Copyright Clearance Center's RightsLink service]

Inhibition of endocytosis and degradation pathways preserves Na/K-ATPase expression in RGCs following short-term pressure exposure

As shown in Figure 3.3, pressure-induced reduction in expression of the Na/K-ATPase occurs initially via modulation of existing Na/K-ATPase protein. Cell surface representation of the Na/K-ATPase can be modulated by altered the endocytosis and degradation pathways of the protein. To further examine the hypothesis that decreases in Na/K-ATPase expression induced following short-term pressure elevation is mediated at the protein level, we targeted endocytosis and degradation pathways of the Na/K-ATPase with the PKC inhibitor bisindolylmaleimide and the proteasome inhibitor MG-132. In other cell types, bisindolylmaleimide-mediated inhibition of PKC prevents endocytosis of the Na/K-ATPase to increase its representation at the plasma membrane.[140] Similarly, inhibition of proteasome activity by MG-132 increases Na/K-ATPase representation on the plasma membrane by inhibiting its degradation.[140] Thus, we treated primary RGC cultures with 10μM bisindolylmaleimide, 20μM MG-132 or vehicle during exposure to ambient or elevated hydrostatic pressure for 4 hours. We then examined expression and localization of the Na/K-ATPase, using immunocytochemistry. Qualitatively, exposure to 4 hours of elevated hydrostatic pressure reduced the intensity of immunolabeling for total Na/K-ATPase in both the soma and neurites (**Figure 3.11A**). Consistent with **Figure 3.3**, 4 hours of elevated pressure decreased immunolabeling of total Na/K-ATPase by 46%, compared to ambient pressure (**Figure 3.11B**, $p<0.05$). In RGC cultures exposed to elevated pressure, treatment with the PKC inhibitor bisindolylmaleimide significantly increased the immunolabeling intensity of total Na/K-ATPase by 46%, as compared to vehicle treatment (**Figure 3.11B**, $p<0.05$). Inhibition of the proteasome with MG-132 significantly also increased the immunolabeling intensity of total Na/K-ATPase by 46% at elevated pressure, as compared to vehicle treatment (**Figure 3.11B**, $p<0.05$). Neither bisindolylmaleimide nor MG-132 altered total Na/K-ATPase immunolabeling in RGC cultures maintained at ambient pressure, as compared to vehicle treatment (**Figure 3.11B**, $p>0.05$). Similarly, there was no significant difference in immunolabeling intensity between bisindolylmaleimide- and MG-132-treated RGCs at elevated

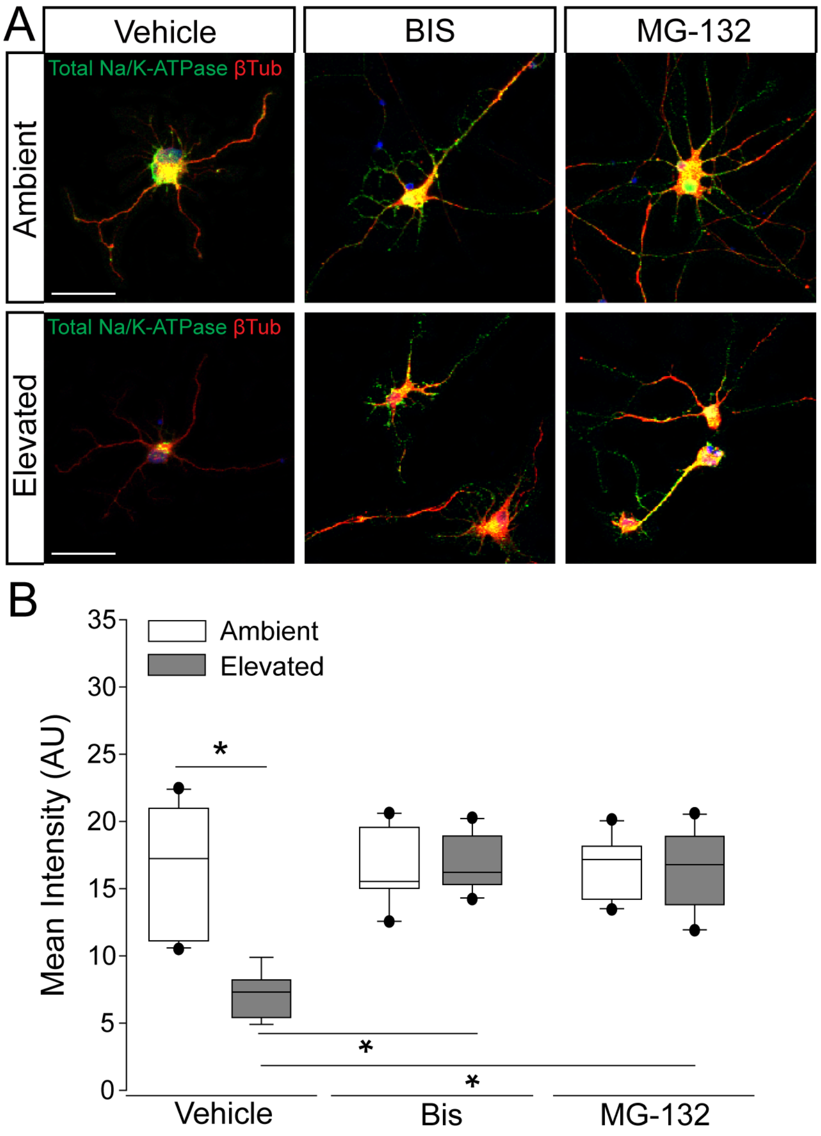

Figure 3.11. Inhibition of endocytosis and degradation pathways preserves Na/K-ATPase expression in RGCs following short-term pressure exposure. (**A**) Representative confocal micrographs of total Na/K-ATPase (green) and β-Tubulin-III (red) immunolabeling in primary, purified RGCs treated with vehicle, 10μM bisindolylmaleimide, or 20μM MG-132 and exposed to ambient or elevated pressure for 4 hours. Scale bar = 40μM. (**B)** Mean intensity (arbitrary units; AU) of total Na/K-ATPase staining per cell in each drug and pressure condition. Asterisk indicates $p < 0.05$. n(Amb)=14, n(Elev)=9; n(Amb+BIS)=11, n(Elev+BIS)=10; n(Amb+MG)=13, n(Elev+MG)=14.

pressure (**Figure 3.11B**, $p > 0.05$). These data suggest that decreased Na/K-ATPase expression caused by short-term pressure elevations is initially caused by breakdown of existing Na/K-ATPase protein. Additionally, inhibition either the endocytosis or degradation pathway can prevent this early pressure-induced reduction in Na/K-ATPase expression.

Inhibition of Na/K-ATPase endocytosis and degradation prevents pressure-induced reduction of inward cation flux

To examine the relationship between pressure-induced decreases in Na/K-ATPase expression and decreased cation influx, we performed thallium flux imaging while concurrently inhibiting endocytosis and degradation of the Na/K-ATPase. We treated RGC cultures with vehicle, 10μM bisindolylmaleimide or 20μM MG-132, while exposing them to either ambient or elevated pressure for 4 hours. As depicted in **Figure 3.11**, inhibition of either Na/K-ATPase endocytosis (bisindolylmaleimide) or degradation (MG-132) is sufficient to retain Na/K-ATPase in the plasma membrane following a 4-hour exposure to elevated pressure. Consistent with **Figure 3.8**, 4 hours of elevated pressure decreased thallium flux by 22% in vehicle-treated cultures, as compared those maintained at ambient pressure ($p < 0.05$; **Figure 3.12A-C**). At ambient pressure, neither bisindolylmaleimide nor MG-132 altered thallium flux, as compared to vehicle ($p > 0.05$; **Figure 3.12A-C**). At elevated pressure, bisindolylmaleimide increased thallium influx by 64%, as compared to vehicle treatment at elevated pressure ($p < 0.05$; **Figure 3.12A,B**). This increase returned thallium influx to levels comparable to vehicle treatment at ambient pressure ($p > 0.05$; **Figure 3.12A,B**). Similarly, treatment with MG-132 increased thallium flux by 78% at elevated pressure, as compared to vehicle-treated cultures exposed to elevated pressure ($p < 0.05$; **Figure 3.12A,C**). Interestingly, this increased thallium flux was 39% greater

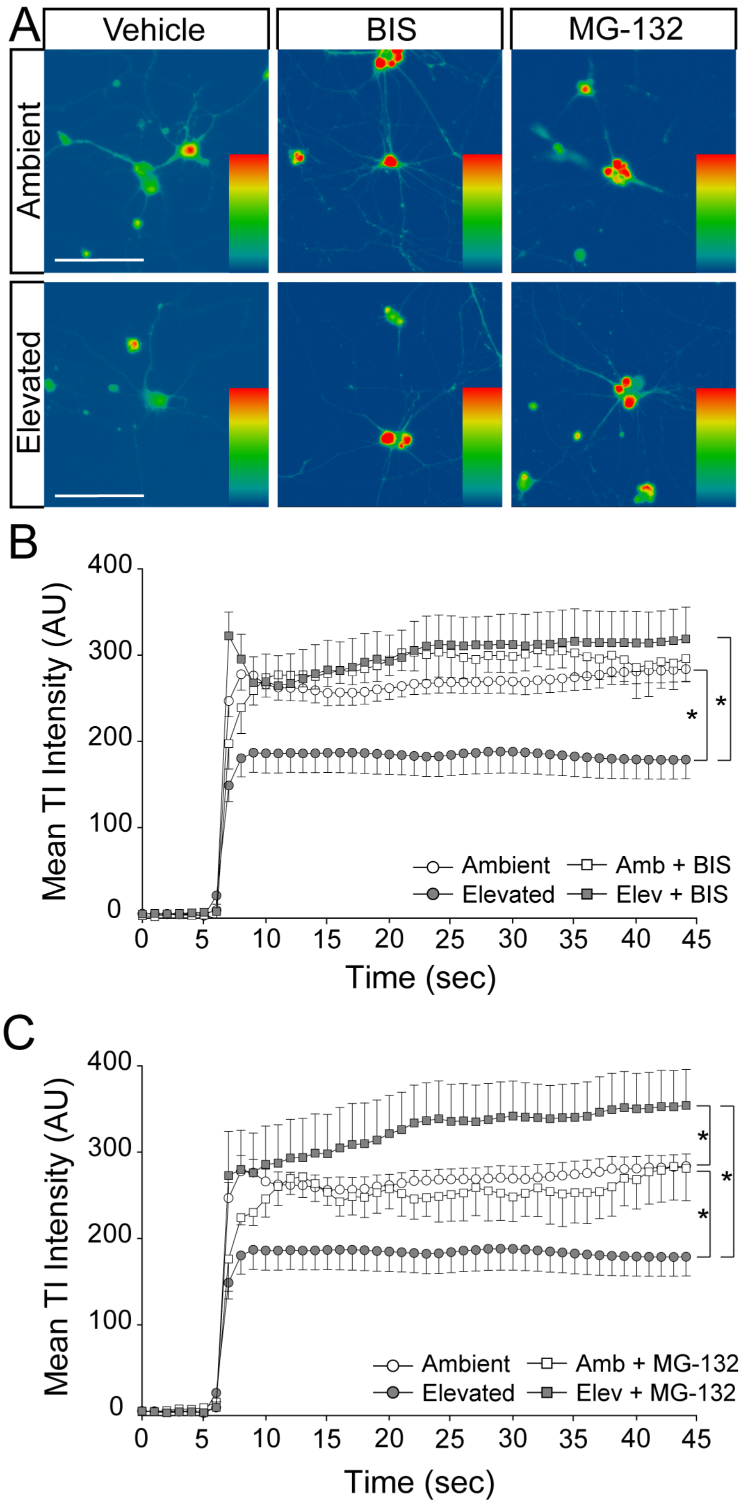

Figure 3.12. Inhibition of Na/K-ATPase endocytosis and degradation prevents pressure-induced reduction of inward cation flux. (**A**) Representative heat maps showing the fluorescent signal of Thallos dye in RGCs exposed to ambient and elevated pressure for 4 hours plus treatment with vehicle, 10µM bisindolylmaleimide, or 20µM MG-132. Images were taken after the addition of thallium. Scale bar = 100µM. (**B**) Line graph displaying the mean fluorescence intensity of Thallos dyes over time for RGCs

exposed to ambient or elevated pressure for 4 hours plus treatment with vehicle or bisindolylmaleimide. Asterisk indicates $p < 0.05$ and error bars represent SEM. n(Amb)=30, n(Elev)=27, n(Amb+BIS)=7, n(Elev+BIS)=16. (**C**) Line graph displaying the mean fluorescence intensity of Thallos dyes over time for RGCs exposed to ambient or elevated pressure for 4 hours plus treatment with vehicle or MG-132. Asterisk indicates $p < 0.05$ and error bars represent SEM. n(Amb)=30, n(Elev)=27, n(Amb+MG132)=3, n(Elev+MG132)=13.

than that observed with vehicle treatment at ambient pressure ($p<0.05$; **Figure 3.12A,C**). These data suggest that retention of the Na/K-ATPase at the plasma membrane, by inhibiting either endocytosis or degradation, is sufficient to prevent pressure-induced decreases in cation influx.

Na/K-ATPase inhibition reproduces cation dyshomeostasis and repolarization deficits

If pressure-induced changes in Na/K-ATPase expression underlie cation dyshomeostasis and electrophysiological deficits in RGCs, inhibition of Na/K-ATPase activity alone should mimic these pressure-induced phenotypes. Therefore, we examined inward cation flux and electrophysiological function in response to treatment with ouabain, a pharmacological inhibitor of the Na/K-ATPase.

We exposed RGC cultures to ambient or elevated pressure for 4 hours in the presence or absence (vehicle) of 20μM ouabain and measured cation influx by thallium flux imaging. This concentration of ouabain is known to inhibit Na/K-ATPase activity in neurons from rat brain.[204,205] Consistent with **Figures 3.8 and 3.12**, exposure to 4 hours of elevated pressure decreased thallium flux by 22% in vehicle-treated cultures, as compared to those at ambient pressure ($p<0.05$; **Figure 3.13A,B**). Treatment with ouabain similarly decreased thallium flux by 26% in cultures maintained at ambient pressure, as compared to vehicle-treated cultures ($p<0.05$; **Figure 3.13A,B**). At elevated pressure, ouabain treatment decreased thallium influx by 33%, compared to vehicle-treated cultures at ambient pressure ($p<0.05$; **Figure 3.13A,B**). This decrease was equivalent to that induced by elevated pressure alone ($p>0.05$; **Figure 3.13A,B**).

These data indicate that inhibition of Na/K-ATPase activity is sufficient to recapitulate pressure-induced decreased in cation influx. Additionally, inhibiting Na/K-ATPase activity during pressure elevation does not result in further reductions in cation influx, likely due to decreased representation of Na/K-ATPase on the plasma membrane, i.e. fewer targets for ouabain.

Next, we examined the effects of short-term Na/K-ATPase inhibition on RGC physiology *ex vivo*. Using whole-cell patch-clamp physiology in intact retina, we measured the frequency and amplitude of spontaneous activity in RGCs following puff administration of 10 or 20 μM ouabain. To allow direct comparison with electrophysiological data in **Figure 2.1**, we utilized retina 4 weeks after bilateral saline injection. Ouabain induced a slight, non-significant increase in the spike frequency of RGCs at both 10 and 20μM concentrations ($p>0.05$; **Figure 3.13C**). Ouabain did not alter the peak amplitude of spikes at either concentration, as compared to vehicle treatment ($p>0.05$; **Figure 3.13D**). Similarly, there was no significant difference in the max rise slope (depolarization phase) between vehicle and ouabain treatment ($p>0.05$; **Figure 3.13E**). Administration of 10μM ouabain did not alter the max decay slope (repolarization phase) in RGCs, as compared to vehicle treatment ($p>0.05$: **Figure 3.13F**). In contrast, 20μM ouabain increased the max decay slope by 37 and 44%, as compared to vehicle and 10μM ouabain, respectively ($p<0.05$ for both; **Figure 3.13F**). This increase in the max decay slope is similar in magnitude to that noted after 4 weeks of elevated IOP in the microbead occlusion model (**Figure 2.1**). These data suggest that healthy RGCs are able to compensate for brief inhibition of Na/K-ATPase activity and maintain spiking frequency and amplitude. However, more robust inhibition of Na/K-ATPase activity (20μM ouabain) reproduces delay in the repolarization phase similar to that observed with IOP elevation (**Figure 2.1 and 3.13**).

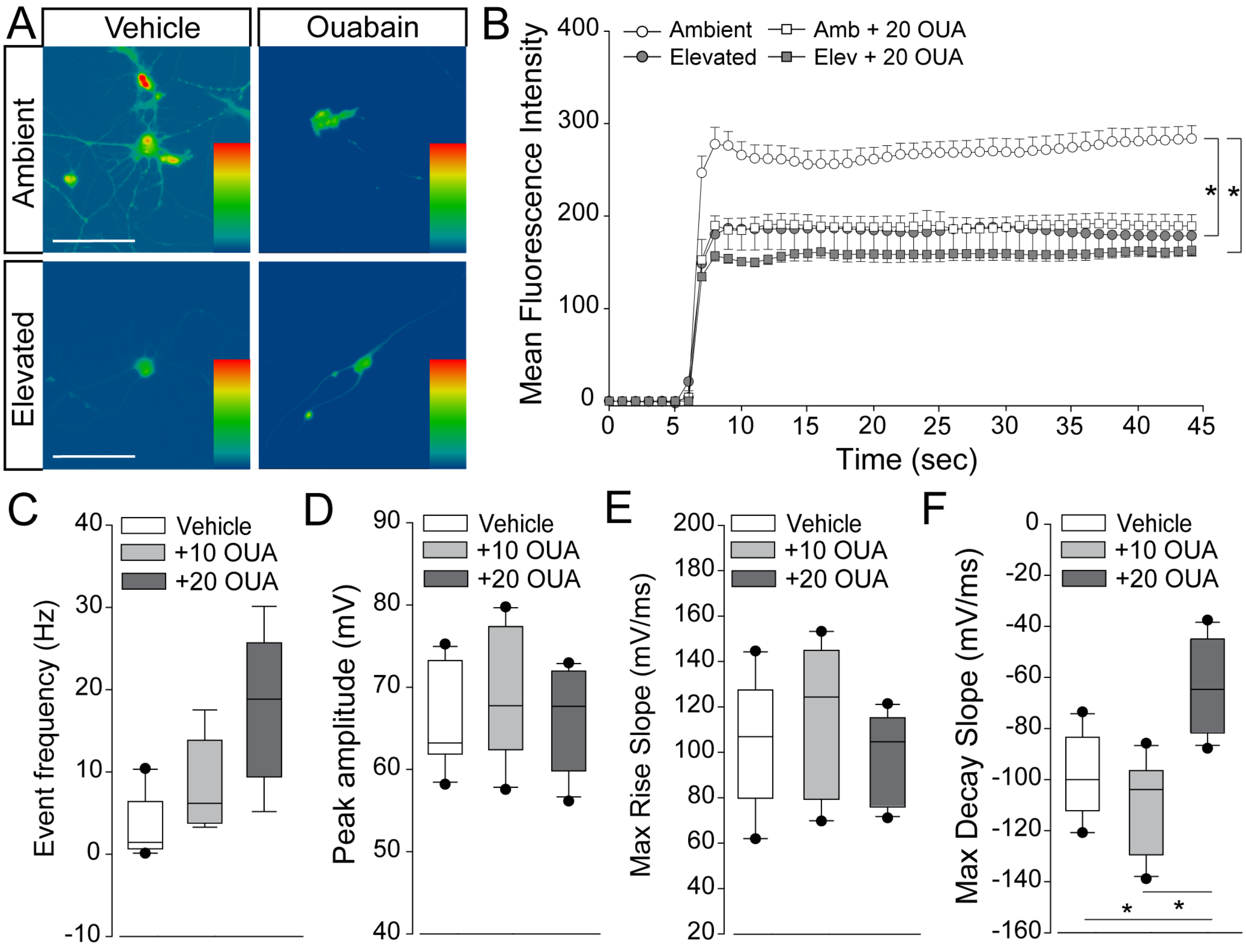

Figure 3.13. Na/K-ATPase inhibition reproduces cation dyshomeostasis and repolarization deficits. (**A**) Representative heat maps depicting the fluorescent signal of Thallos dye in RGCs exposed to ambient and elevated pressure for 4 hours in the presence of vehicle or 20µm ouabain or vehicle. Scale bar = 100µM. (**B**) Line graph displaying the mean fluorescence intensity of Thallos dyes over time for RGCs exposed to ambient or elevated pressure for 4 hours in the presence of vehicle or 20µm ouabain. Asterisk indicates $p < 0.05$ and error bars represent SEM. n(Amb)=30, n(ELEV)=27, n(Amb+OUA)=5, n(ELEV+OUA)=6. (**C-F**) Whole cell patch-clamp physiology in RGCs from retina of saline-injected eyes following puff administration of vehicle, 10µM, or 20µM ouabain. Asterisk indicates $p < 0.05$. (**C**) Frequency of spontaneous spiking depicted as mean event frequency (Hz) across cells for each condition. n(vehicle)=12, n(10)=9, n(20)=9. (**D**) Peak amplitude of spontaneous spiking depicted as mean peak amplitude (mV) across cells for each condition. n(vehicle)=11, n(10)=10, n(20)=11. (**E**) Max rise slope of spontaneous spiking depicted as mean max rise slope (mV/ms) across cells for each condition. n(vehicle)=14, n(10)=10, n(20)=11. (**F**) Max decay slope of spontaneous spiking depicted as mean max decay slope (mV/ms) across cells for each condition. n(vehicle)=10, n(10)=7, n(20)=11.

Discussion

Pressure-induced changes in expression profiles of the Na/K-ATPase, Kir, and K2P channels were seen in the retina of mice with ocular hypertension. In this chapter, we examined pressure-induced changes in expression and localization of K^+ channels in RGCs and Müller glia, specifically. We additionally measured outcomes of cell health and K^+ homeostasis in RGC and Müller glia cultures.

Upon assessing the pressure-induced changes in expression of Kir and K2P channels, we found that certain genes that displayed altered expression through transcriptome analysis in whole retina did not show a significant change in expression in primary, purified Müller glia cultures (**Figure 3.4**). Further analysis of Müller glia-specific changes to Kir and K2P channels showed pressure-induced alterations in expression and localization in Müller glia cultures (**Figures 3.5-7**).

When assessing the combined results from Chapters 2 and 3, our transcriptome analysis and immunohistochemical studies revealed pressure-induced changes in the expression and localization of both Kir and K2P K^+ channels. Elevated pressure in decreased the representation of Kir4.1 and TASK-1, while increasing representation of Kir2.1, TRAAK and TRESK. Elevated pressured also reduced transcription of TWIK-1 (*Kcnk1*). Studies have shown that TWIK-1 and TASK-1 are acid-sensitive K2P channels and exhibit dynamic ion selectivity.[162,190] Additionally, under acidic extracellular conditions, TWIK-1 and TASK-1 become permeable to extracellular Na^+.[190] Thus, these pressure-induced reductions of these channels on the plasma membrane could contribute to the increase in extracellular K^+ concentrations.

RNA sequencing of whole retina in MOM mice revealed significant downregulation of the Kir3.2, Kir2.2 and Kir2.4 and THIK-2, TASK-1 and TWIK-1. Studies show that Kir3.2 is predominantly expressed by RGCs, where it localizes to the plasma membrane, dendrites and axons.[188] Additionally, as expression was undetectable through qRT-PCR in Müller glia cultures, it is likely that downregulation of Kir3.2 in our *in vivo* glaucoma model arises from modulation in RGCs rather than Müller glia. Expression and localization Kir2.2 and Kir2.4 in retina is less clear. A study of glial cells in guinea pig retina identified mRNA expression of both Kir2.2 and Kir2.4.[189] However, Kir2.2 protein expression was undetectable by immunohistochemistry in murine retina in a later study.[127] Our transcriptome analysis indicates that both Kir2.2 and Kir2.4 channels are constitutively transcribed in murine retina and this expression is sensitive to elevated IOP. As expression of both of these channels was undetectable through qRT-PCR in Müller glia cultures, it is likely that they are expressed primarily in RGCs, or another cell type in the retina.

As outlined in the Chapter 1, TWIK-1 is expressed by both Müller glia and RGCs, while TASK-1 is predominantly expressed by RGCs, but also expressed at lower levels in Müller glia.[156] Our data is consistent with this study, indicating expression of both channels in whole retina, as well as in Müller glia cultures. Our transcriptome analysis identified constitutive THIK-2 expression in retina that was substantially downregulated by elevated IOP. In a study of K2P channel expression in retina, THIK-2 was not detectable by qPCR profiling, consistent with our results in Müller glia cultures, but not in whole retina.[156] These conflicting results are likely attributable to methodological differences in detection and require further investigation. It is important to note that TASK-1, TWIK-1, and THIK-2 channels are all known to heterodimerize with other channels from their sub-families.[162] Thus, the functional outcome of changes in K^+ channel expression are likely diverse and dependent on cell type-specific expression. Despite any discrepancies in modulation of K2P channels by elevated pressure *in vitro* and *in vivo*, both model approaches revealed that K2P channels with dynamic ion selectivity are modulated by elevated pressure.[162] Overall, our *in vivo* findings suggest that ocular hypertension alters the expression profile of K^+ channels implicated in K^+ siphoning, suggesting that ion homeostasis may be chronically altered in glaucoma.

We also examined the impact of elevated pressure on overall health and ion homeostasis of Müller glia. In primary, purified cultures of Müller glia, we evaluated early and sustained responses to pressure *in vitro* with two exposure paradigms - 4 hours and 48 hours. 48 hours of elevated pressure produced significant LDH release (**Figure 3.2**), increased extracellular concentrations of K^+ and reduced inward cation flux (**Figure 3.9**). Of these pressure-induced changes, only the reduction in inward cation flux was also noted at the 4-hour time point (**Figure 3.9**). Furthermore, inhibition of cation channels at ambient pressure reduced inward cation flux to levels comparable to 4 hours of elevated pressure (**Figure 3.10**). However, increasing the extracellular $[K^+]$ did not produce any changes in electrophysiological activity in healthy Müller glia (**Figure 3.9**).

Several studies have shown that elevated pressure *in vitro* and *in vivo* leads to apoptosis of RGCs (**Figure 3.1**).[172,173] However, pressure-induced increases in cytotoxicity in Müller glia is a novel finding. During apoptosis, intracellular contents are contained and removed by phagocytes to avoid eliciting inflammation in the neighboring cells.[206] However, increased permeability of the membrane, like that observed with cytotoxicity, can release intercellular contents that have inflammatory and potentially, detrimental effects on surrounding cells.[206] As discussed in the previous chapter, cytotoxic responses from one cell can affect the health and viability of neighboring cells and perpetuate inflammatory and pathological processes.[92]

We found that long-term pressure elevation induced cation dyshomeostasis in Müller glia, resulting in increases in the extracellular concentration of K^+. This cation dyshomeostasis could be caused by release of ions through a compromised plasma membrane, like that indicated by LDH release, or an active process resulting in reduced ion influx. Our live cell, thallium flux imaging revealed reduced inward cation flux at both 4 and 48-hour time points. While time in culture slightly reduces cation channel activity (ambient pressure 4 versus 48 hours), exposure to elevated pressure over time dramatically reduces channel activity (elevated pressure 4 versus 48 hours). In summary, changes in cation flux are detectable after only 4 hours of elevated pressure, while elevations in LDH release and $[K^+]_E$ are not seen until 48 hours of elevated pressure. This indicates that modulation of cation channel activity precedes plasma membrane compromise, and suggests that reduced inward flux of cations is an early component of the Müller glia response to elevated pressure.

For neurons to perform their physiological function, proper ion concentration gradients must be maintained. In the retina, Müller glia assist in the establishment of ion concentrations gradients by siphoning excess K^+ from the extracellular milieu.[127-129,146,151,152] Our findings indicate that elevated pressure alters cation homeostasis and cation channel flux in Müller glia *in vitro*. This is accompanied by changes in expression and localization of Kir and K2P channels with inward-rectifying capabilities. Downregulation of Kir and K2P channels are also seen in the Microbead Model of glaucoma. These data support the hypothesis that disrupting ion homeostasis could impact proper establishment of ion concentration gradients and that prolonged disruption of these gradients could contribute to altered physiological activity of RGCs in glaucomatous retina.[47,115,207]

While the pressure-induced changes in K^+ channel expression and cation homeostasis are promising in Müller glia, a more robust phenotype was found in pressure-induced changes in Na/K-ATPase expression and activity in RGCs. *In vitro* studies confirmed that elevated pressure reduces protein expression of both total and α1 Na/K-ATPase in RGCs, specifically (**Figure**

3.3). Interestingly, this pressure-induced decrease was evident at both 4 and 48 hours of exposure, suggesting that the initial decrease in Na/K-ATPase expression is not mediated by genetic downregulation. As outlined in Chapter 1, Na/K-ATPase expression can be regulated in part by altering the representation of the protein at the plasma membrane through a constitutive rate of endocytosis and degradation.[143] As such, we found that inhibition of endocytosis or degradation were both sufficient to retain expression of total Na/K-ATPase after a 4-hour exposure to elevated pressure (**Figure 3.11**). These data confirmed that elevated pressure induces an early reduction in available Na/K-ATPase via activation of endocytosis and degradation pathways.

Phosphorylation of the Na/K-ATPase by PKC or p38 kinase initiates the endocytosis pathway.[140-143] Following endocytosis, the Na/K-ATPase is degraded by the proteasome.[140,141] One possible mechanism for how elevated pressure induces activation of these pathways is through intracellular Ca^{2+} signaling. PKC is activated by diacylglycerol and intracellular Ca^{2+}.[208] One of the earliest events in RGC degeneration during glaucoma is intracellular Ca^{2+} dysregulation.[3,178] Increased intracellular Ca^{2+} levels, via TRPV1 signaling, are found in primary, purified RGC cultures after exposure to only 1 hour of elevated pressure.[173] Early activation of intracellular Ca^{2+} signaling in response to elevated pressure could activate PKC signaling in RGCs, resulting in activation of the Na/K-ATPase endocytosis pathway. Another possible mechanism is through p38 kinase-mediated endocytosis. Activation of p38 MAPK is evident in multiple mouse models of glaucoma and treatment with a selective inhibitor of the p38 MAPK catalytic domain (Ro3206145) prevents axon transport deficits as well as structural degeneration of RGC axons.[209-211]

To examine the effect of pressure-induced reduction in Na/K-ATPase expression on ion homeostasis, we performed thallium flux imaging in cultured RGCs to measure inward cation flux. We found that both 4 and 48 hours of elevated pressure decreases thallium influx in RGCs *in vitro* (**Figure 3.8**). This decrease in cation influx resulted in an increase in extracellular K^+ concentration after 48 hours of pressure elevation, measured by ICP-MS (**Figure 3.8**). As 48 hours of pressure elevation did not induce cytotoxicity in RGCs *in vitro*, it is unlikely that this increase in extracellular K^+ is due simply to increased permeability of the membrane (**Figure 3.1**). This was confirmed by pharmacological studies to increase representation of Na/K-ATPase at the plasma membrane to increase its overall activity, which resulted in maintenance of cation influx at ambient levels in RGCs exposed to elevated pressure (**Figure 3.12**). Therefore, our data suggests that early pressure-induced cation dyshomeostasis occurs via reduced inward cation flux due to reduced Na/K-ATPase activity via endocytosis and degradation. While prolonged exposure to elevated pressure results in downregulation of the Na/K-ATPase transcription to produce chronic cation dyshomeostasis (**Figure 2.2-3**).

Our loss-of-function studies with the Na/K-ATPase inhibitor ouabain further confirmed the mechanistic relationship between Na/K-ATPase activity and pressure-induced deficits in cation homeostasis and RGC electrophysiology. Inhibition of Na/K-ATPase decreases thallium influx in RGCs maintained at ambient pressure to levels observed following 4 hours of pressure elevation (**Figure 3.13**). During patch-clamp electrophysiology, healthy RGCs were largely able to counter puff administration of ouabain (**Figure 3.13**). However, 20μM ouabain increased the max decay slope to a level similar to that of RGCs in retina from microbead-injected eyes (**Figures 2.1 and 3.13**). These data suggest that even brief inhibition of Na/K-ATPase in healthy retina can reproduce the repolarization phase phenotype observed in glaucomatous retina.

Importantly, the electrophysiological deficits we observed were apparent after 4 weeks of microbead-induced IOP elevation. At this time point, RGCs exhibit axon transport deficits with fairly moderate structural degeneration of axons in the optic nerve.[96,165,168] Altered RGC physiological function arising from ion dyshomeostasis could be a significant part of the transition from functional deficits to irreversible, structural loss of RGC axons in the optic nerve. As maintaining proper physiological activity is crucial for neuron survival, these deficits could be a first step towards eventual cell death.[212] Our data clearly demonstrate a link between compromised axon transport, impaired physiological activity, and Na/K-ATPase-mediated deficiencies in electrochemical homeostasis. However, it is unclear whether pressure-induced reduction in Na/K-ATPase activity is a potential cause, or a response to, RGC compromise. As outlined in detail in Chapter 1, K^+ dyshomeostasis in the retina has the potential to act as a propagating agent for electrophysiological impairment and represents a possible etiological factor of spatial clustering of RGC pathology and vision loss.

CHAPTER 4

GRAPHENE: A TOOL TO STUDY SPATIOTEMPORAL PROGRESSION OF RGC DEGENERATION[4]

Introduction

As demonstrated in the previous chapters, K^+ dyshomeostasis in the retina has the potential to act as a propagating agent for electrophysiological impairment and represents a possible etiological factor of spatial clustering of RGC pathology and vision loss. Future directions for these studies will be to determine whether Na/K-ATPase-mediated disruption of K^+ homeostasis contributes to topographical spread of axonopathy by propagating electrophysiological impairment between neighboring RGCs. We plan to map glaucoma-related changes in electrical activity across the retina to discern the pattern of these changes relative to the pattern of axon transport deficits. In collaboration with a team of engineers, we have developed a novel and custom graphene-based microfluidic device that would allow for recording, mapping and manipulation of electrical activities from both large populations of neurons across the retina, as well as simultaneous individual neuron recordings.

The unique properties of graphene provide some advantages for biosensing over traditional electrophysiological techniques, such as patch-clamp and MEA. Graphene is a single layer of carbon atoms, assembled in a honeycomb lattice with extraordinary electronic and optical properties. This device combines a layer of graphene film over gold electrodes, with scanning photocurrent microscopy to detect electrical activity within the retina. As a two-

---

[4] Portions of this chapter were published as Fischer et al. (2018) Advanced Healthcare Materials and Zhang et al. (2016) Nanoscale.

dimensional material, graphene exposes its whole structure to the environment, making it extremely sensitive to local electrochemical environment changes. Electrical activity between cells in the retina can modulate the electrical properties of the graphene to produce photocurrent signals. We can record these photocurrent signals at basal levels and in response to a stimulus, such as light or K^+, as a means of measuring the electrical activity of RGCs in the retina. **Figure 4.1A** shows a retina with CTB-labeled RGCs in red. Strong photocurrent responses can be detected from the graphene underneath the ONH, suggesting that the electrical activity of the ONH is sufficient to alter the local electrical properties of graphene (**Figure 4.1B,C**).

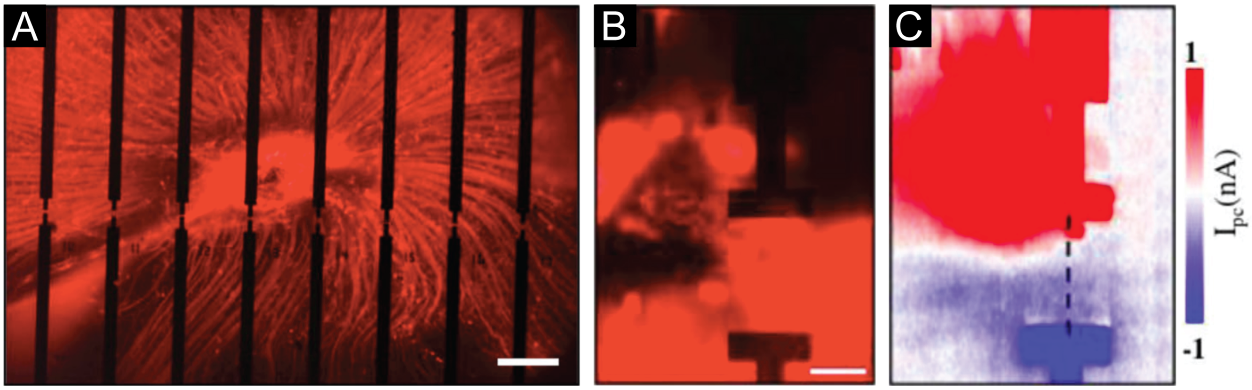

Figure 4.1. Graphene photocurrent recordings from retina. (**A**) Fluorescence image of a CTB-labeled retina on top of graphene transistors. There are 54 separated electrodes in an electrode array, where the edge-to-edge distances between two electrodes in the horizontal direction is 180µm and between upper and lower electrodes are 20µm, 40µm, and 60µm, respectively. A graphene film is placed on top of all electrodes. Here, 16 opaque electrodes near the ONH are imaged. Scale bar = 200µm. (**B**) Fluorescence and (**C**) scanning photocurrent images CTB-labeled retina on top of a graphene transistor over the ONH. Scale bar = 30µm.
[Figure adapted from Zhang et al. (2016) Nanoscale[213] and used in accordance with Copyright Clearance Center's RightsLink service.]

To map electrophysiological changes in RGCs to axon transport facility, CTB labeled retina from microbead-injected eyes will be mounted onto the graphene platform. Imaging CTB uptake allows us to discern where there are clusters of degenerating RGCs. Within areas of high or low CTB uptake, we can then stimulate and detect electrophysiological activity across two modalities: 1) high resolution (sub-micrometer) using local graphene optoelectronic probes, and

2) broader resolution (100-200μm) across the entire retina through 2D mapping of graphene transistor arrays. This graphene platform has been chosen over traditional electrophysiological assays because of its ability to provide the spatial resolution needed to record from individual neurons, as well as larger populations of neurons across the retina. Additionally, with the microfluidic component of the device, the retina can be kept alive on the device for several days, allowing for the temporal resolution to perform recordings over multiple days. Therefore, these experiments will provide real-time spatial and temporal mapping of ion flux, and thus, electrical activity of individual cells, as well as the entire intact retina.

While great progress has been made on many fronts, fundamental questions pertaining to biomedical applications of graphene still remain unanswered. One critical issue for biomedical devices is how graphene influences the behavior of living cells or tissues, which is still not well understood despite the general acceptance that graphene is biocompatible.[214-221] For example, based on its transparent nature and super-high electron mobility, graphene has been proposed as a sensing element that could be utilized in many novel assays in electrophysiology.[222,223] To function optimally in this capacity, direct contact between cellular processes and graphene is required and this contact would ideally minimally impact interactions between cells and their environment. For examples, when utilizing neuronal cultures, the culture substrate is of primary importance for cell survival, differentiation and functionality; the needs of a specific neuronal subtype or cell line dictate the optimal culture substrate.[224-229] Common matrix substrates for neuronal cultures include poly-l-lysine (PLL), poly-d-lysine (PDL) and laminin, which are coated on glass prior to cell plating.

Envisioning the great potential of graphene for sensing in neurobiological applications, a few groups have conducted studies to examine *in vitro* viability of primary neuronal cultures or human neuroblastoma cell lines on graphene substrates.[214-216,218-221] To date, both direct culture on bare graphene that is adhered to thin glass slides[215-217,219,220] and on graphene coated with matrix substrates[214,221] have been reported. The comparison of outcomes of these studies is done while keeping in mind the fact that different cell types were used (i.e. neuroblastoma cell lines, primary cells from different developmental stages and areas of the nervous system) and preparation of graphene substrates may also vary in different assays. Cell culture on bare graphene allows for direct interactions between the cells and graphene. Studies suggest that neurons can be grown on bare graphene adhered to glass, but are conflicted on whether graphene influences cell viability and vitality.[214,216,217,219,230] Studies that combine graphene and matrix substrates utilize platforms in which graphene is sandwiched between a thin glass slide and a layer of matrix substrate, with cells plated on top of the matrix substrate. While this approach does achieve a combinatorial substrate of graphene and organic matrix, direct contact between cellular processes and graphene is prevented. Although the outcomes of these studies are also conflicting, most suggest that the presence of graphene underneath organic matrix substrates does not adversely impact cell adhesion, viability or vitality.[214,221]

While direct contact between cells and graphene is not a requirement for some neurobiological applications, direct contact between cells and graphene is often mandatory for biosensing applications.[218] Therefore, it is important to clarify whether graphene impedes the ability of neurons to interact with biological elements in their environment that exist prior to graphene deposition. We performed a systematic study to determine whether applying graphene on top of organic matrix substrates masks interactions between these matrix substrates and primary cultures of purified neurons. We fabricated six different cultures platforms for primary retinal ganglion cells (RGCs) that were comprised of matrix substrates known to have low, medium and high efficacy for these neurons. Three of the culture platforms included a layer of graphene placed on top of the matrix substrate. With the use of these platforms, we determined whether graphene overlay and the direct contact between RGCs and the graphene layer alters substrate efficacy, as measured by several important indices of cell viability and vitality, including receptor-mediated endocytosis and neurite outgrowth. We further assessed the specific potential for graphene to serve as a biosensor in electrophysiological assays by measuring substrate and graphene effects on cation channel activity. Results indicate that graphene overlay does not impede the interactions between RGCs and underlying substrate matrix, such that the positive or negative effects of culture substrates are retained. This likely arises from the ability of graphene, with its atomic thickness, to conform to the structure of each substrate matrix. However, direct contact between RGCs results in increased cation channel activity, regardless of substrate. This is accompanied by a decrease in the number of voltage-gated sodium and potassium channels at the plasma membrane. Increased activity appears to serve as a compensatory mechanism for the change in ion channel representation, resulting in similar biophysical properties to RGCs cultured on substrate-only platforms.

Overall, our data indicate that graphene is biocompatible with the simplest and most sensitive biological model: primary cell culture. This bodes well for its biocompatibility with more complex systems, such as an *ex vivo* retina. Additionally, these studies suggest that when the proper baselines are established, graphene is a promising biosensing material for applications in neuroscience, such as electrophysiological assays. The unique properties of graphene provide some advantages for biosensing over traditional electrophysiological techniques, such as patch-clamp and multielectrode array (MEA). A graphene platform could allow for recording, mapping and manipulation of electrical activities of large populations of neurons across the retina, as well as simultaneous individual neuron recordings.

Materials and Methods

Graphene synthesis

Copper foils (Alfa Aesar 0.025mm, 99.8% pure) with a grain size of ~100μm were cut into strips 8 mm wide. Then, a 5% nitric acid (10 min) bath was used to eliminate contamination. A copper strip was loaded onto a quartz boat, which was transferred to a horizontal furnace system. After the system was pumped down to 10 mTorr, the copper strip was annealed at 1000°C with 100sccm H_2 for 1 hour. A mixed gas of 80sccm H_2 and 20sccm CH_4 was then introduced into the furnace for the growth of graphene at 1000°C for 30 minutes.

Substrate preparation

Metal markers were patterned on coverslips via photolithography, and deposited with 5nm Cr and 40nm Au by thermal evaporation. 8x8mm squares were then cut from a graphene/copper-strip. After spin coating with an ultrathin polymethyl methacrylate (PMMA) layer, a wet etching process was performed to remove the copper foil by copper etchant. The PMMA/graphene film was transferred to the coverslips that were pre-coated with laminin or PDL. Film was left to dry overnight. Once dry, acetone, isopropyl alcohol and deionized water baths were used to remove the PMMA layer and clean the substrates. Finally, Raman spectroscopy was utilized to identify the thickness and quality of graphene with a 532nm excitation laser.

Isolation of primary, purified retinal ganglion cell cultures

Primary cultures of purified RGCs were prepared as previously described (Chapter 3).[169,172,173,178] Experiments were performed on RGCs approximately 1 week after plating.

Cell survival assay

To determine the extent of cell death in RGC cultures plated on different substrates, with or without graphene overlay, a LIVE/DEAD™ Viability/Cytotoxicity Kit for mammalian cells was utilized (Cat# L3224, ThermoFisher). The LIVE/DEAD assay utilizes calcein-AM to label cells with active intracellular enzyme activity and ethidium homodimer-1 (EthD-1) to label cells with a compromised plasma membrane. Cells were incubated in a phosphate-buffered saline solution containing 6μM calcein-AM and 4μM EthD-1 for 15 minutes at 37°C. Then, fluorescent microscopy was used to image live cells following calcein-AM and EthD-1 staining. In subsequent fluoromicrographs, calcein+, EthD-1+, and calcein+/EthD-1+ RGCs were counted and the density (cells/mm^2) of calcein+ and EthD-1+ RGCs (n = 13, glass; 10-11, laminin; 5-9, PDL) was calculated and compared between the three substrates with and without graphene.

Receptor-mediated endocytosis assay

To measure receptor-mediated endocytosis in RGCs, we utilized the neural tracer CTB (1 μg/μL CTB-594, Cat# C34777; 1 μg/μL CTB-488, Cat# C34775, ThermoFisher). 2μl of CTB was added to each well (24-well plate, ~800ul media per well) and incubated for approximately 24 hours at 37°C. Live cell fluorescent microscopy was used to image uptake and transport of CTB in RGCs. In subsequent fluoromicrographs, CTB+ RGCs were counted and the cell density was quantified by calculating the number of cells per mm^2. The quantification of CTB+ cell density (n = 7, glass; 9-12, laminin; 5-10, PDL) was compared between the three substrates with and without graphene.

Neurite outgrowth assay

RGC cultures were labeled with calcein, as described above. Neurite complexity was measured in calcein+ RGCs by overlaying fluoromicrographs with a 25x25µm grid mask and counting the number of times each neurite intersected with the grid. The quantification of number of intersections (n = 5-6, glass; 5-6, laminin; 6-18, PDL) was compared between the three substrates with and without graphene. The length of individual neurites was also measured.

Ion channel activity assay

Thallium flux imaging was performed as previously described (Chapter 3). Using live cell fluorescence microscopy, the baseline fluorescence of the Thallos dye was recorded for continuously 30 seconds (images taken every 10 seconds). 2mM thallium (TI^+) solution was then added to cell culture media and live imaging was performed continuously for the 5 minutes (images taken every 10 seconds). Fluorescence intensity was calculated for each image using Nikon NIS-Elements software. To determine the change in fluorescence intensity of the thallos dye after TI^+ was added, the peak intensity after TI^+ was divided by the baseline intensity to generate Δfluorescence. Δfluorescence was compared between the three substrates with and without graphene (n = 6-9, glass; 5, laminin; 4-7, PDL).

Electrophysiology

RGCs with circular somas and neurite processes extending from the cell body were targeted for intracellular recordings. The culture medium was exchanged with an extracellular solution containing (in mM) 140 NaCl, 5 KCl, 2 $CaCl_2$, 2 $MgCl_2$, 10 Hepes, 10 dextrose, adjusted to a pH of 7.4 with NaOH (290 osm). Intracellular recording pipettes were pulled from thick-walled borosilicate glass and filled with (in mM) 130 KCl, 10 NaCl, 0.5 $CaCl_2$, 2 $MgCl_2$, 5 EGTA, 10 Hepes, 3 Na_2-ATP adjusted to pH 7.2 with NaOH (280 osm). Recording pipettes had a resistance between 8-11 MΩ. Electrophysiological recordings were performed at room temperature ($23^{o}C$). RGCs were viewed using an upright microscope (Olympus BX51, 40X) under differential interference contrast (DIC), using a CCD (charge-coupled device) camera (Andor). The recording pipette was positioned onto an RGC, forming a tight seal (> 1 GΩ) between the recording pipette and cultured RGC. Then, brief negative pressure pulses were applied to break into cells to form a whole-cell configuration (access resistance typically < 50 MΩ) and voltage clamped at -80 mV. To assess basic electrical activity from cultured RGCs, we measured currents produced by brief, 40 ms voltage steps from -80 to +30 mV in +10 mV increments. Changes in input current were subtracted from the response to the test potential by averaging six hyperpolarizing pulses after the test potential (P/6 protocol). We measured peak inward and outward currents generated during each test potential.

Statistical analysis

Statistical analysis was conducted with SigmaPlot Version 13 (Systat Software Inc, San Jose, CA). Data were assessed for normality by Shapiro-Wilkes test and for equal variance by Brown-Forsythe test. All data passed normality test ($p > 0.05$ for all). For comparisons within the substrate-only and graphene-integrated platforms that passed equal variance testing ($p > 0.05$), statistical significance was assessed by a one-way analysis of variance (ANOVA) with post-hoc correction and pairwise comparison by Holm-Sidak Method. For comparisons within the substrate-only and graphene-integrated platforms that failed equal variance testing ($p < 0.05$), statistical significance was assessed by a Kruskal-Wallis one-way ANOVA on ranks with post-hoc correction and pairwise comparison by Dunn's Method. Statistical comparisons between the graphene-integrated platforms and their respective substrate-only platforms were conducted with a T-test. For all statistical comparisons, $p \leq 0.05$ was considered statistically significant.

Results

Matrix substrates and standard culture conditions do not affect the quality of graphene

To test whether graphene overlay has any impact on the interactions of neurons with underlying biological elements, we performed our studies with primary cultures of RGCs. As demonstrated by significant previous literature[224-229], laminin is the preferred substrate for primary RGC cultures. Anecdotally, bare glass and PDL are generally considered sub-optimal, with PDL being preferable to bare glass. While these substrates have not been officially compared for efficacy, field standards for primary RGC cultures indicate that these three substrates represent a continuum of efficacy for the establishment of viable and vital RGCs. As such, we designed six different culture platforms, using these three substrates. We produced three substrate-only platforms: the first was a glass coverslip, the second was a glass coverslip coated with laminin and the third with PDL. We then adopted three graphene-integrated versions of the substrate-only platforms, with graphene overlaid on top of the substrate (**Figure 4.2A**). As depicted in **Figure 4.2A**, RGCs were in direct contact with graphene in the graphene-integrated platforms. All cultures, regardless of platform, were maintained in optimal growth media for RGCs, as previously described.[172,173]

RGCs on top of graphene were labeled with CTB conjugated to Alexa 488 fluorophore (**Figure 4.2B**; top panel). To make sure that these cells were cultured on graphene, we examined the graphene using Raman spectroscopy following cell plating and exposure to standard culture conditions for one week. As shown in the second panel of **Figure 4.2B**, the 2D (~2681 cm^{-1}) peak exhibited a symmetric shape and the 2D-to-G (~1583 cm^{-1}) intensity ratio was about 2, which indicates that the graphene had a monolayer structure. To characterize the continuity of the graphene, we extracted and plotted intensity ratio mapping of the characteristic graphene Raman 2D-G intensity ratio. This spatial mapping revealed continuous distribution of graphene underneath RGCs with glass, laminin and PDL substrates (**Figure 4.2B**; third panel). These data indicate that successful transfer of graphene on laminin and PDL matrix is feasible and graphene remains intact following cell plating and exposure to the environmental conditions of cell culture. Finally, direct contact with neurons does not disrupt the graphene layer, regardless of underlying substrate.

Matrix substrate, but not graphene overlay, impacts RGC density

We next measured RGC survival as a function of culture substrate and determined the impact of graphene overlay on the survival baselines for each of these substrates. RGC survival was determined by plasma membrane integrity and the presence of intracellular enzyme activity, using a Viability/Cytotoxicity assay (LIVE/DEAD™ Kit, ThermoFisher). We labeled RGC cultures one week after plating with calcein-AM (green) and ethidium homodimer-1 (EthD-1, red) to measure intracellular enzyme activity and plasma membrane integrity, respectively. Cells

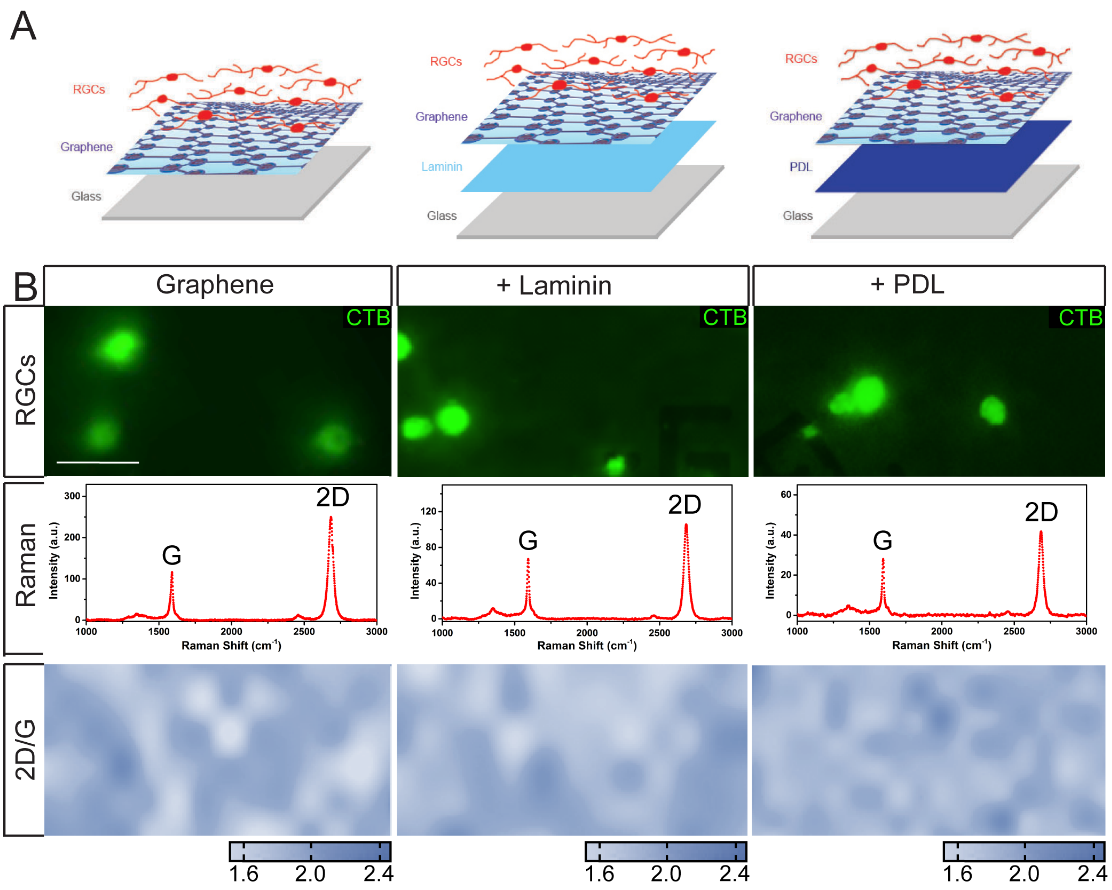

Figure 4.2. Matrix substrates and standard culture conditions on the quality of graphene overlay. (**A**) Schematics of the graphene-integrated devices. Glass coverslips were coated with laminin or PDL. Graphene was then placed on top of laminin or PDL coating. RGCs were plated directly on top of graphene. (**B**; top panel) Images are representative fluorescent micrographs of RGCs cultured graphene alone (left), laminin (middle) or PDL (right) with graphene overlay. RGCs were labeled with CTB conjugated to Alexa Fluor-488 (green). (**B**; second panel) Quality of the graphene alone, or on laminin or PDL, was assessed by Raman spectra and intensity ratio mapping of 2D and G peaks (**B**; third panel). Scale bar=10μm; Images taken at 40x.
[Figure from Fischer et al. (2018) Adv Healthc Mater[186] and used in accordance with Copyright Clearance Center's RightsLink service.]

that label calcein+ only are designated as "live" or "viable" cells, whereas cells that label EthD-1+ only are designated as "dead" cells.[231,232] Cells that label positive for both calcein and EthD-1 are designated as "compromised" due to a disrupted plasma membrane that allowed EthD-1 to enter, but still retain active intracellular enzyme activity to convert calcein-AM to calcein.

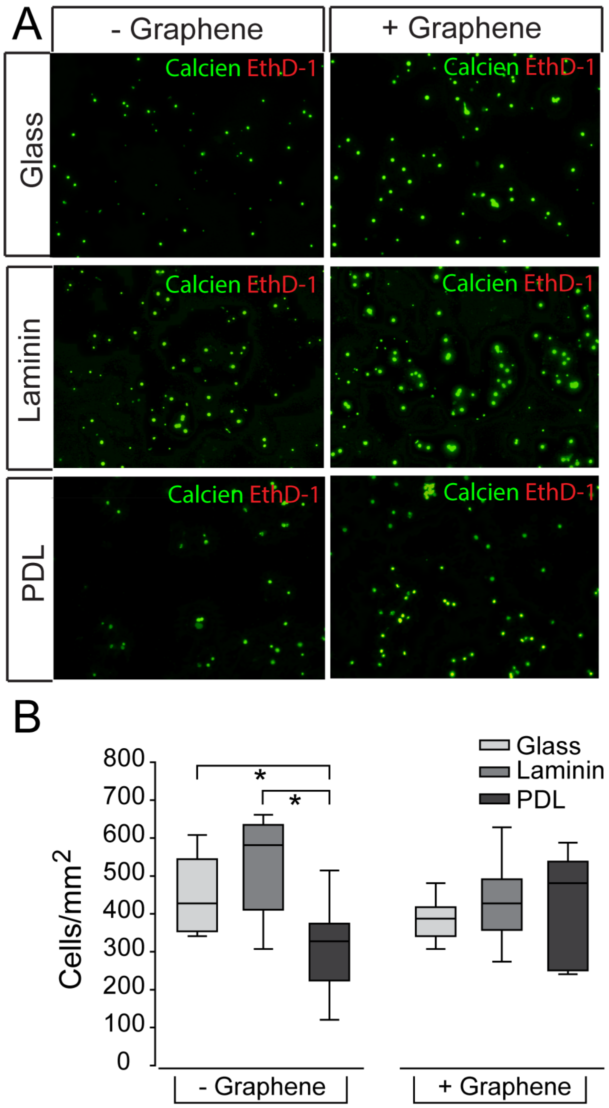

Figure 4.3. RGC culture density on culture substrates with graphene overlay. (**A**) Images are representative fluorescent micrographs of RGCs cultured on glass (top), laminin (middle), or PDL (bottom) with (+) or without (-) graphene overlay. RGCs were labeled with calcein (green) and ethidium homodimer-1 (red). Scale bar=100μm. (B) Box plots depict total cell density (y-axis; cells/mm^2) in each culture platform. Asterisks indicate $p < 0.05$.
[Figure from Fischer et al. (2018) Adv Healthc Mater[186] and used in accordance with Copyright Clearance Center's RightsLink service.]

For cultures plated on bare glass as well as both matrix substrates, a majority of RGCs were calcein+ (green) with minimal co-labeling with EthD-1 (yellow) (**Figure 4.3A**). This baseline level of cell compromise was consistent with previous studies.[172] EthD-1+ only cells (red) were essentially not detected at this one-week time point in any of our culture platforms

(**Figure 4.3A**). Quantification of calcein and EthD-1 labeling revealed that graphene overlay did not alter RGC density, as compared to their respective substrate-only platforms ($p > 0.05$; **Figure 4.3B**). Importantly, comparison between platforms with and without graphene overlay indicates that graphene does not alter cell viability and the overall health of the cells in these two groups is similar. Additionally, we found that the density of RGCs was 31% and 41% lower in the PDL platform, as compared to bare glass and laminin platforms, respectively ($p < 0.05$ for both; **Figure 4.3B**).

Matrix substrate, but not graphene overlay impacts receptor-mediated endocytosis of CTB in RGCs

To determine whether graphene overlay altered the ability of RGCs to execute a more complex cellular function, we first assessed receptor-mediated endocytosis across our culture platforms, using the active uptake, active transport tracer CTB. This tracer is commonly used to measure axon transport and connectivity in RGCs.[13,94,110,165,233] CTB binds to the GM1 ganglioside receptor and enters RGCs via caveolin-1-mediated endocytosis.[165,233] Following endocytosis, CTB is trafficked to RGC terminals via the microtubule network.[13,110] The active cellular processes required for uptake and transport of CTB makes it an ideal marker of not only viability, but also cell vitality.

In our studies, one week after plating in our six culture platforms, RGCs were treated with CTB conjugated to Alexa Fluor-594 (red) for 24 hours. CTB uptake and transport was visualized by live cell fluorescent imaging. All culture platforms contained CTB+ RGCs, which exhibited CTB in both the soma and along neurites (**Figure 4.4A**). Quantification of CTB+ RGC density shows that the density of CTB+ RGCs in graphene-integrated platforms did not differ statistically from their respective substrate-only platforms ($p > 0.05$ for all; **Figure 4.4B**). We therefore conclude that RGCs in the graphene-integrated platforms exhibited similar vitality to those in their respective substrate-only platforms, indicating that graphene overlay did not alter the measured efficacy of glass, laminin or PDL substrates.

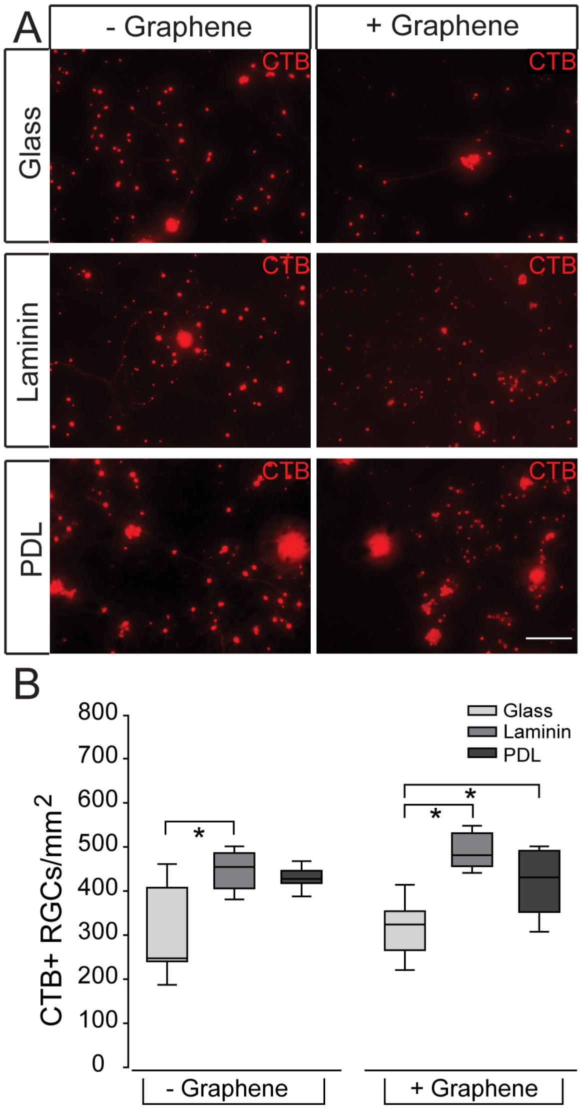

Figure 4.4. Receptor-mediated endocytosis of CTB in RGCs on culture substrates with graphene overlay. (**A**) Images are representative fluorescent micrographs of RGCs cultured on glass (top), laminin (middle), or PDL (bottom) with (+) or without (-) graphene overlay. RGCs were labeled with CTB conjugated to Alexa Fluor-594 (red). Scale bar=100µm. (**B**) Box plots depict CTB+ cell density (y-axis; cells/mm^2) in each culture platform. Asterisks indicate $p<0.05$.
[Figure from Fischer et al. (2018) Adv Healthc Mater[186] and used in accordance with Copyright Clearance Center's RightsLink service.]

We found that the laminin-only platform contained 32% more CTB+ RGCs than the bare glass platform ($p < 0.05$; **Figure 4.4B**). The PDL-only platform contained a median density of CTB+ RGCs that was between bare glass and laminin platforms ($p > 0.05$; **Figure 4.4B**). For the graphene-integrated platforms, graphene overlay on bare glass contained 35% and 25% lower density of CTB+ RGCs than graphene overlay on laminin and PDL, respectively ($p < 0.05$ for both; **Figure 4.4B**). These data suggest that while PDL substrate yields the lowest absolute density of RGCs (**Figure 4.3**), the vitality of these RGCs, as measured by receptor-mediated endocytosis, is higher than that achieved with a bare glass substrate.

Matrix substrate, but not graphene overlay impacts RGC neurite outgrowth

We then assessed neurite outgrowth as another important indicator of neuronal vitality *in vitro* to assess whether graphene overlay affects the cell function. To measure neurite outgrowth, we quantified the complexity of RGC neurites with live cell imaging in cultures labeled with either calcein-AM or CTB (**Figure 4.5A**). Neurite complexity was measured by counting the number of times calcein+/CTB+ neurites intersected the lines of a 25 μm x 25 μm grid mask placed on each image. Additionally, we measured the length of individual neurites in each culture platform.

The quantification results revealed that the number of intersections was 2-fold higher in the laminin platform and 1.5-fold higher in bare glass platform than in the PDL platform ($p < 0.05$ for both; **Figure 4.5B**). Importantly, RGCs cultured on the graphene-integrated laminin platform also exhibited the most neurite outgrowth, with ~1.5-fold more intersections than graphene-integrated glass and PDL platforms ($p < 0.05$ for both; **Figure 4.5B**). Quantification of the mean neurite length showed a similar significant difference between cultures grown on

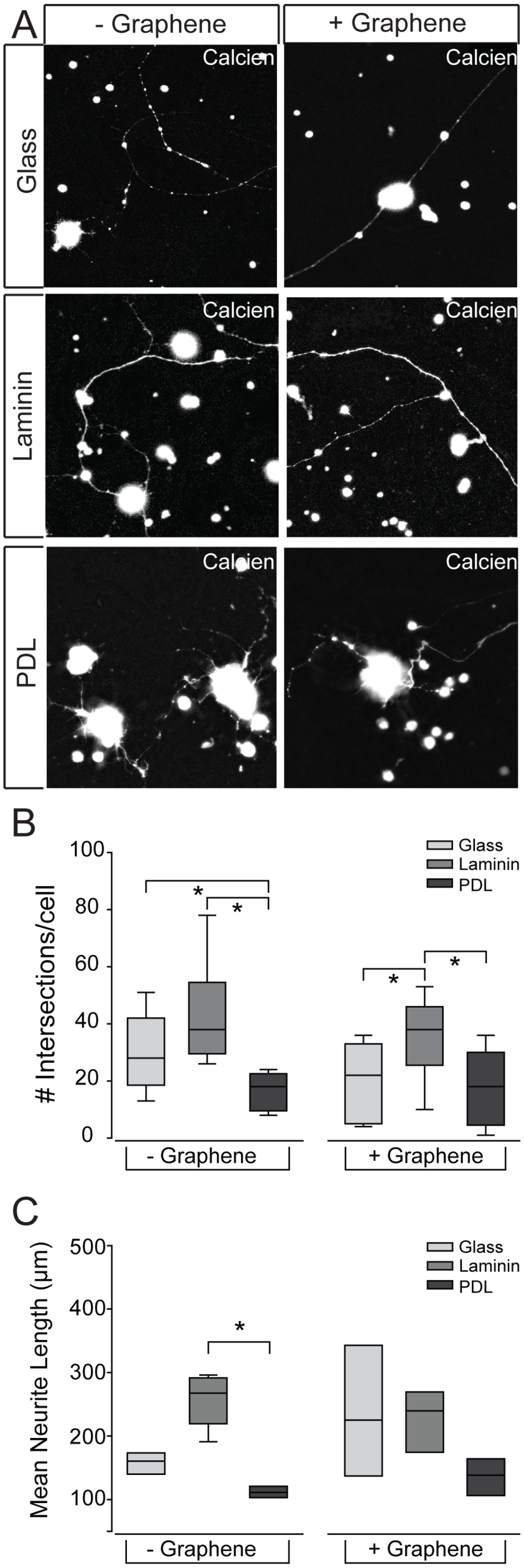

Figure 4.5. RGC neurite outgrowth on culture substrates with graphene overlay. (**A**) Images are representative fluorescent micrographs of RGCs cultured on glass (top), laminin (middle), or PDL (bottom) with (+) or without (-) graphene overlay. RGCs were labeled with calcein (white). Scale

bar=100μm. (**B**) Box plots depict the number of intersections per cell (y-axis) in each culture platform. Intersections were counted as the number of times any neurite crossed a line in the 25x25μm grid that was overlaid on fluoromicrographs of 20x magnification. (**C**) Box plots depict the mean neurite length (μm) in each culture platform. Asterisks indicate $p<0.05$.
[Figure adapted from Fischer et al. (2018) Adv Healthc Mater[186] and used in accordance with Copyright Clearance Center's RightsLink service.]

laminin and PDL ($p < 0.05$; **Figure 4.5C**), but did not show any difference in neurite length between cultures on the graphene-integrated platforms. Overall, there is no significant difference in neurite outgrowth between graphene-integrated platforms and their respective substrate-only platforms ($p > 0.05$; **Figure 4.5B,C**), indicating that graphene overlay does not alter efficacy of glass, laminin or PDL substrates. As to the effects of different matrix substrates, **Figure 4.5B and 4.5C** suggests that PDL matrix impedes neurite outgrowth in RGCs, while laminin matrix promotes neurite outgrowth. Bare glass exhibits median efficacy as a substrate for neurite outgrowth that is similar to laminin in substrate-only devices and similar to PDL in graphene-integrated devices.

Matrix substrate and graphene overlay impact cation channel activity in RGCs

To more specifically assess the potential application of graphene as a biosensor for electrophysiological assays, which require direct contact between neuronal processes and graphene, we measured the effect of graphene overlay on cation channel activity in RGCs across our three culture substrates. Ion channel activity is essential to neuronal function, particularly neurotransmission, and is the basis for electrophysiological assays.

One week after plating cells in our six culture platforms, we performed real-time, thallium flux imaging.[196] The representative images in **Figure 4.6A** depict baseline fluorescence of Thallos dye (left panels) and fluorescence after the addition of thallium (right panels). For illustration purposes, heat maps of the fluorescence signal for individual cells are depicted in panel insets (**Figure 4.6A**). We quantified cation channel activity as the change in fluorescent intensity of thallium between baseline and peak measurements (peak/baseline intensity) for individual RGCs (**Figure 4.6B**). RGCs cultured on bare glass and laminin matrix platforms exhibited similar levels of cation channel activity, as indicated by thallium flux ($p > 0.05$; **Figure 4.6B**). In contrast, RGCs cultured on the PDL matrix platform exhibited approximately 19-23% less cation channel activity than both glass and laminin substrates ($p < 0.05$; **Figure 4.6B**). Similarly, RGCs cultured on the graphene-integrated PDL platform exhibited 24% and 42% less thallium flux than RGCs cultured on graphene-integrated glass and laminin platforms, respectively ($p < 0.05$; **Figure 4.6B**). Like the substrate-only platforms, the graphene-integrated glass and laminin platforms exhibited similar levels of cation channel activity ($p > 0.05$; **Figure 4.6B**).

Importantly, RGCs cultured on each of the graphene-integrated platforms exhibited greater cation channel activity than their respective substrate-only platforms ($p < 0.05$ for all; **Figure 4.6B**). This increase in thallium flux ranged from 6% - 37% (**Figure 4.6B**). These data indicate that PDL matrix impairs cation channel activity in RGCs. Additionally, these data suggest that graphene overlay increases overall cation channel activity, regardless of substrate and does not change the relative efficacy of glass, laminin and PDL, which suggests that despite overall enhancement of cation channel activity, graphene overlay does not obscure the cation channel phenotype induced by the culture substrate.

Graphene overlay does not alter the biophysical interaction between voltage-gated sodium and potassium channels in cultured RGCs

To further inform the changes in ion channel activity seen from the thallium flux studies,

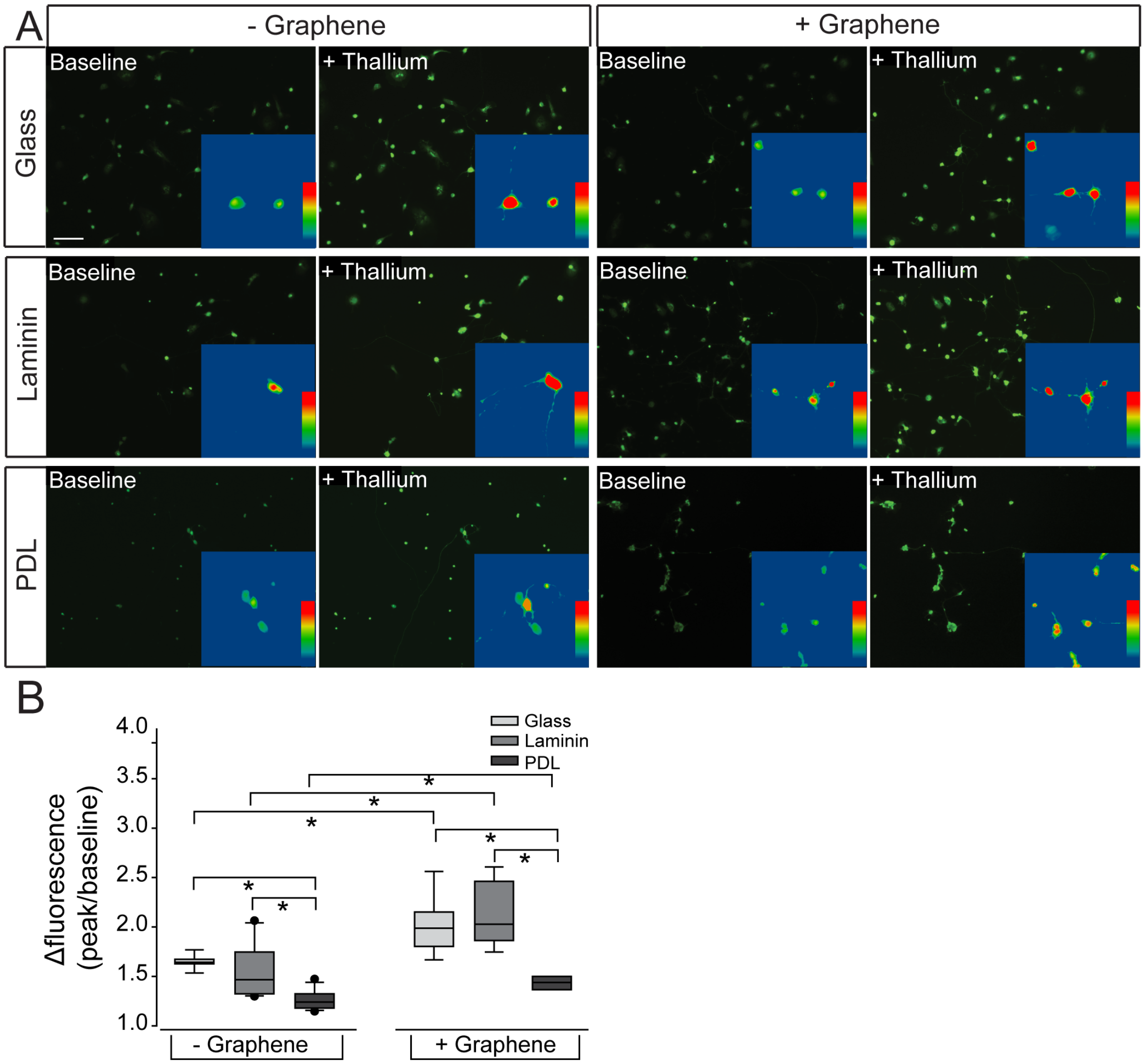

Figure 4.6. Cation channel activity in RGCs on culture substrates with graphene overlay. (**A**) Images are representative fluorescent micrographs of RGCs cultured on glass (top), laminin (middle), or PDL (bottom) platforms with (+) or without (-) graphene overlay. RGCs were loaded with the cell-permeable dye Thallos (green). Images were taken at baseline and after addition of thallium, which binds to and increases the fluorescent intensity of Thallos dye. Scale bar=100μm. Insert: zoom of an individual cell within the larger image analyzed with a heat map showing the fluorescent signal of Thallos dye. (**B**) Box plots depict the change in the fluorescent intensity of each cell (peak intensity/baseline intensity). [Figure from Fischer et al. (2018) Adv Healthc Mater[186] and used in accordance with Copyright Clearance Center's RightsLink service.]

we performed whole-cell, patch-clamp recordings on RGCs on laminin and graphene-integrated laminin platforms to measure inward and outward current activity of the cells. Since the effect of graphene overlay on cation channel activity was similar regardless of substrate and cell integrity is paramount for whole-cell patch clamp, we chose to only culture and record from cells on the preferred cultured substrate for RGCs, laminin. RGCs cultured on both laminin and graphene-integrated laminin platforms showed similar morphology (**Figure 4.7A, 4.7B**).

RGCs on both laminin and graphene-integrated laminin platforms produced transient inward currents followed by prolonged outward currents to depolarizing test potentials (**Figure 4.7C, 4.7D**). RGCs on both laminin and graphene-integrated laminin platforms activated inward current statistically different from zero at -60mV (**Figure 4.7E**). RGCs on laminin platforms showed increased inward currents up to -20mV followed by decreased inward currents from -10 to 30mV, which is likely due to an interaction between inactivating voltage-gated Na^+ channels and activation of voltage-gated K^+ channels at these higher test potentials. RGCs on both laminin and graphene-integrated laminin platforms showed increased inward currents from -60 to -30mV followed by a decrease in inward current for remaining test potentials. RGCs on graphene-integrated laminin platforms showed a modest but statistically significant decrease in inward currents for test potentials between -30 to -20mV as compared to laminin only substrate (*, $p \leq 0.025$). Both RGCs on laminin and graphene-integrated laminin platforms showed outward current activation at -30mV, and outward current generally increased as test potential increased. However, RGCs on graphene-integrated laminin platforms showed a statistically significant decrease in peak outward current between 10 to 30mV (#, $p \leq 0.015$). Reduced inward and outward currents for RGCs cultured on graphene-integrated platforms suggest a decrease in the number of functional voltage-gated sodium and potassium channels.

To understand if graphene impacts the biophysical characteristics of these channels mediating inward and outward currents, we normalized peak inward and outward current values

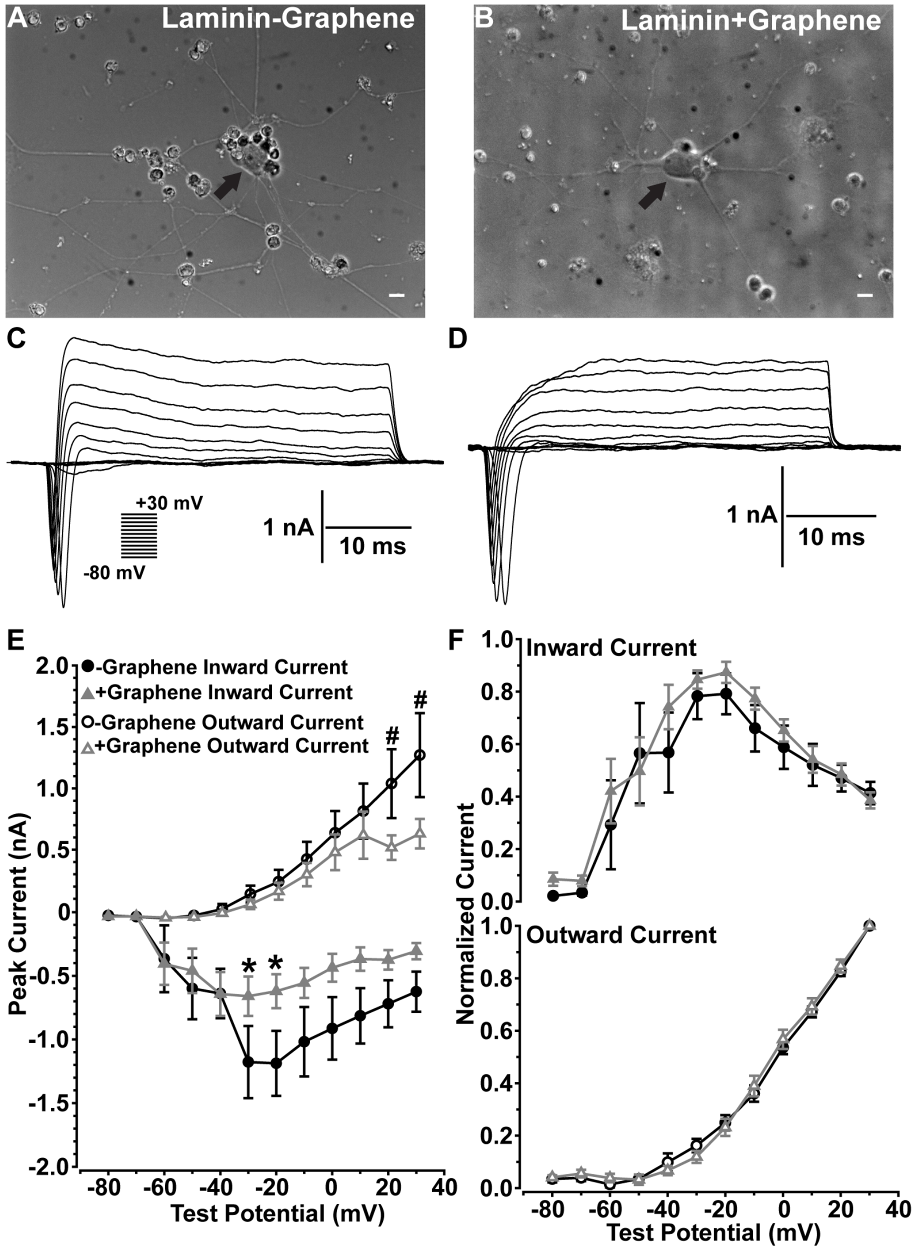

Figure 4.7. Inward and outward current activity of RGCs cultured on graphene. RGCs cultured on laminin platforms without (-, **A**) or with (+, **B**) graphene overlay showed large cell bodies (arrows) with widespread neurite processes. Scale bars = 20μm. RGCs cultured on laminin platforms without (-, **C**) or with (+, **D**) graphene overlay produced transient inward currents followed by prolonged outward currents to depolarizing test potentials. (**E**) Line graphs of peak inward and outward currents. (**F**) Line graphs depict normalized inward and outward currents. (n = 7, -Graphene; n = 10, +Graphene; $*p \leq 0.025$; $\#p \leq 0.015$).

[Figure from Fischer et al. (2018) Adv Healthc Mater[186] and used in accordance with Copyright Clearance Center's RightsLink service.]

produced at each test potential. We found no significant difference between inward and outward current profiles (**Figure 4.7F**) of RGCs on laminin or graphene-integrated laminin platforms, suggesting the reduced number of voltage-gated Na^+ and K^+ channels in RGCs plated on graphene does not influence the biophysical interaction between voltage-gated Na^+ and K^+ channels governing action potential initiation and membrane repolarization.

Discussion

These studies address a critical issue for neurobiological applications of graphene; how graphene influences the behavior of living neurons. This idea is still not well understood despite the general acceptance that graphene is biocompatible.[214-221] We examine the effect of graphene through comparing the outcomes of viability, vitality and electrophysiological function in primary cultures of RGCs on each of three common substrates (glass, laminin and PDL) with and without graphene overlay. Our results confirm that culture substrate influences the health of primary neurons in culture; laminin substrate yielded the most robust RGC cultures, as anticipated. Based on anecdotal evidence, we expected PDL matrix to yield more robust RGC cultures than bare glass. However, our data suggest that the efficacy of bare glass and PDL matrix as substrates for RGC cultures depends on the outcome examined. For three of the four outcomes we examined, the bare glass platform yielded more robust RGC cultures than the PDL matrix platform. This suggests that interactions between RGCs and PDL matrix could negatively influence RGC viability, vitality and function.

For all viability and vitality assays examined, graphene-integrated platforms exhibited the same pattern of RGC phenotypes as the substrate-only platforms. This indicates that direct contact between RGCs and graphene, a monolayer atomic structure, does not impede interactions between RGCs and underlying substrate matrix, such that the positive or negative effects of culture substrates are retained. It is likely that the atomically thin graphene conforms to the structure of underlying matrix and as such, mechanical interaction between cells and extracellular matrix are still allowed.

Interestingly, we observed that graphene enhances cation channel activity, as demonstrated by an increase in the magnitude of thallium influx. Other studies examining the physiology of neurons cultured on graphene have found a potentiation of neurotransmission through increased presynaptic vesicle number, release probability, and turnover rate.[234] Graphene producing an increase in presynaptic neurotransmission could lead to increased postsynaptic cation channel activity, which is consistent with our thallium flux results on graphene-integrated platforms.

Our electrophysiological recordings showed reduced inward and outward currents for RGCs cultured on graphene-integrated platforms. This indicates a decrease in the number of functional voltage-gated sodium and potassium channels. This reduction in cation channel expression could arise from many cellular processes, such as transcription, translation, protein trafficking and membrane structure.[234] Despite differences in ion channel representation, analysis of overall inward and outward current profiles revealed no significant difference between RGCs cultured on substrate-only or graphene-integrated platforms, indicating that graphene overlay does not alter the overall biophysical properties of RGCs. This is supported by previous studies showing that neurons cultured on graphene substrates do not show significantly altered electrophysiological properties, compared to neurons cultured on traditional culture substrates.[217] Increased cation channel activity, like that noted in our thallium flux assay, could serve as a compensatory mechanism to maintain the biophysical properties of RGCs, despite graphene-mediated reductions in the number of functional voltage-gated sodium and potassium channels.

Overall, our data suggest that while graphene does not alter the physiological phenotype of RGCs, it does alter the way in which this phenotype is achieved. Although further studies are required to elucidate the cause of changes in ion channel expression and the underlying mechanism for increased cation channel activity, the identification of these graphene-dependent changes is important for interpretation of electrophysiological assays utilizing graphene as the biosensor. Our data indicates that, when the proper baselines are established, graphene is a promising biosensing material for applications in neuroscience, such as electrophysiological assays.

CHAPTER 5

SUMMARY

Purpose of Studies

The objective of these studies was to identify extracellular events that could underlie the spatiotemporal progression from functional deficits to structural RGC degeneration in glaucoma. Studies by others and us in animal models indicate that axon transport deficits in RGCs during glaucoma are accompanied by electrophysiological impairment. Preliminary data from our laboratory indicated there is decreased expression of the Na/K-ATPase in glaucomatous retina and decreased ion flux through K^+ channels in RGCs *in vitro* following exposure to glaucoma-related stressors. This led us to our *central hypothesis* that disruption of K^+ homeostasis underlies electrophysiological impairment of RGCs during glaucoma via changes in the expression and activity of the Na/K-ATPase. This hypothesis was addressed using these two specific aims:

Aim 1. Determine the nature of the electrophysiological deficits in RGCs during glaucoma.

Aim 2. Determine the mechanism responsible for K^+ dyshomeostasis during glaucoma and implications for RGC physiology.

Outcomes of Studies

Through these studies, we sought to examine the electrophysiological impairment seen in the glaucomatous retina by investigating the potential relationship between electrophysiological properties and axon transport facility in glaucomatous RGCs. Additionally, we wanted to elucidate the pressure-dependent mechanisms underlying any such relationship. We specifically investigated ion homeostasis and the role of the Na/K-ATPase and K^+ siphoning in maintenance of ion concentration gradients in the retina.

Electrophysiological studies revealed that deficits in axon transport seen in RGCs from microbead-injected eyes coincide with a more depolarized resting membrane potential and diminished ability to maintain frequency of induced spiking. Elevation of the extracellular K^+ concentration resulted in a decrease in both the frequency and amplitude of K^+-induced spiking that was accompanied by a significant increase in the max decay slope. Therefore, this electrophysiological phenotype appears to arise from elongation of the repolarization phase of the action potential.

Repolarization is a critical phase of the action potential, where the cell needs to reestablish the electrochemical gradients of ions. There are two primary mechanisms by which ion concentration gradients are maintained in the retina: 1) the Na/K-ATPase in RGCs and 2) K^+ siphoning by Müller glia. To determine if ocular hypertension directly alters expression and function of K^+ channels in the retina implicated in maintenance of ion homeostasis, we examined changes in the expression of the Na/K-ATPase and Kir and K2P channels with inward-rectifying capabilities in the retina of mice with ocular hypertension. We found that 4 weeks of elevated IOP reduces gene and protein expression of both total and α1 Na/K-ATPase in retina from microbead-injected eyes. Elevated pressure *in vivo* results in decreased transcription of a subset of Kir and K2P channels in the retina of MOM mice. Additionally, immunohistochemical staining of retinal sections from microbead mice revealed altered representation of Kir and K2P channels.

As pressure-induced changes in expression profiles of the Na/K-ATPase, Kir, and K2P channels were all seen in the retina of mice with ocular hypertension, we next sought to examine whether glaucoma-related stressors directly alter expression and localization of K^+ channels in Müller glia and RGCs, individually. Additionally, we measured outcomes of cell health, ion homeostasis, and ion flux in Müller glia and RGC cultures. Long-term pressure elevation in Müller glia cultures resulted in changes in expression and localization of these Kir and K2P channels. Long-term pressure elevation in Müller glia *in vitro* additionally results in significant LDH release, increased extracellular concentration of K^+, and reduced cation flux. In contrast, short-term pressure elevation only resulted in reduced cation flux. However, increasing the extracellular K^+ concentration did not produce any changes in electrophysiological activity in healthy Müller glia. Finally, the pressure-induced decrease in cation influx can be recapitulated by treatment with a cation channel inhibitor at ambient pressure. Our findings have implications for the response by Müller glia to a glaucoma-related stressor, such as elevated pressure. Additionally, modulation of K^+ siphoning machinery in Müller glia and altered cation homeostasis has implications for electrophysiological impairment noted in RGCs of glaucomatous retina.

In vitro studies in RGCs confirmed that short- and long-term pressure elevation reduces protein expression of both total and α1 Na/K-ATPase. Furthermore, elevated pressure in RGCs induces an early reduction in available Na/K-ATPase via activation of endocytosis and degradation pathways, as inhibition of endocytosis or degradation were both sufficient to retain expression of total Na/K-ATPase after a 4-hour exposure to elevated pressure. Pressure-induced reductions in Na/K-ATPase activity results in reduced cation influx in RGCs and leads to cation dyshomeostasis. Our data suggests that early pressure-induced cation dyshomeostasis occurs via reduced inward cation flux due to reduced Na/K-ATPase activity via endocytosis and degradation. Increasing representation of Na/K-ATPase at the plasma membrane to increase its overall activity resulted in maintenance of cation influx at ambient levels in RGCs exposed to elevated pressure. In contrast, prolonged exposure to elevated pressure results in downregulation of Na/K-ATPase transcription to produce chronic cation dyshomeostasis. In healthy RGCs, pharmacological inhibition of the Na/K-ATPase reproduces both cation influx and repolarization phase phenotypes observed with elevated pressure. Together, these data suggest that pressure-induced deficits in axon transport are accompanied by impaired electrophysiological function of RGCs that arises from failure to maintain electrochemical gradients.

Impairment of electrochemical gradients has the potential to impact not only the RGC exhibiting the deficit, but also surrounding RGCs, which must also maintain electrochemical gradients to properly function. Our findings raise the interesting possibility for a “snowball” effect, where prolonged disruption of electrochemical gradients in a small cluster of RGCs could lead to cation dyshomeostasis that impairs the electrochemical gradients of RGCs surrounding that cluster and so on. Thus, the electrophysiological phenotypes and mechanisms described here may be relevant for topographic spread of neurodegeneration in glaucoma. To further examine this hypothesis, we sought to map glaucoma-related changes in electrical activity across the retina to discern the pattern of these changes relative to the pattern of axon transport deficits. To do this, we began investigating the use of graphene to measure electrophysiological properties of RGCs in the retina and as a tool to study the spatiotemporal progression of RGC degeneration. Graphene is a promising biosensing material for applications in neuroscience, such as electrophysiological assays. The unique properties of graphene provide some advantages for biosensing over traditional electrophysiological techniques, such as patch-clamp and MEA. A graphene platform could allow for recording, mapping and manipulation of electrical activities of large populations of neurons across the retina, as well as simultaneous individual neuron recordings. This would be optimal for mapping glaucoma-related changes in electrical activity to axon transport facility across the glaucomatous retina. Direct contact between cells and graphene is not a requirement for some neurobiological applications such as neuroprosthetics. However, direct contact between cells and graphene is often mandatory for biosensing applications. Therefore, it was important to clarify whether graphene impedes the ability of neurons to interact with biological elements in their environment that exist prior to graphene deposition.

We performed a systematic study to determine whether applying graphene on top of organic matrix substrates masks interactions between these matrix substrates and primary cultures of purified neurons. We fabricated six different platforms for primary cultures of retinal ganglion cells (RGCs) that were comprised of matrix substrates known to have low, medium and high efficacy for these neurons. Three of the culture platforms included a layer of graphene placed on top of the matrix substrate. Using these platforms, we determined whether graphene overlay and the resultant direct contact between RGCs and the graphene layer alters substrate efficacy, as measured by several important indices of cell viability and vitality, including receptor-mediated endocytosis and neurite outgrowth. We further assessed the specific potential for graphene to serve as a biosensor in electrophysiological assays by measuring substrate and graphene effects on cation channel activity. Results indicate that graphene overlay does not impede interactions between RGCs and underlying substrate matrix, such that the positive or negative effects of culture substrates are retained. However, direct contact between RGCs results in increased cation channel activity, regardless of substrate. This is accompanied by a reduction in the number of functional voltage-gated sodium and potassium channels. Increased activity appears to serve as a compensatory mechanism for the change in ion channel representation, resulting in similar biophysical properties to RGCs cultured on substrate-only platforms.

Overall, our data suggest that while graphene does not alter the biophysical phenotype of RGCs, it does alter the way in which this phenotype is achieved. The identification of these graphene-dependent changes is important for interpretation of electrophysiological assays utilizing graphene as the biosensor. Our data indicates that, when the proper baselines are established, graphene is a promising biosensing material for *in vitro* applications in neuroscience, such as electrophysiological assays.

Potential mechanism behind outcomes of altered K^+ homeostasis in glaucoma and spatiotemporal progression of glaucoma pathology

The electrophysiological deficits we observed in glaucomatous RGCs were apparent after 4 weeks of microbead-induced IOP elevation. At this time point, RGCs exhibit axon transport deficits with fairly moderate structural degeneration of axons in the optic nerve.[96,165,168] Altered RGC physiological function arising from ion dyshomeostasis could be a significant part of the transition from functional deficits to irreversible, structural loss of RGC axons in the optic nerve. As maintaining proper physiological activity is crucial for neuron survival, these deficits could be a first step towards eventual cell death.[212] This stage of disease progression is particularly important, as the period of time between onset of functional deficits and the physical degeneration of RGCs represents a potential therapeutic window to interrupt axonopathy prior to irreversible, structural loss.

Several studies have shown that deficits in axon transport do not occur uniformly throughout the glaucomatous retina and that RGC axonopathy occurs in clusters of neighboring cells.[48,50,65,95,112] It is therefore highly likely that any electrophysiological deficits accompanying axon transport deficits in the retina also occur in a topographic manner. The potential for ion dyshomeostasis to act as a propagating agent for electrophysiological impairment introduces a novel possibility for etiology of spatial clustering of RGC pathology and vision loss.

Impairment of electrochemical gradients has the potential to serve as an external cue to propagate physiological dysfunction, and ultimately, degeneration, between RGCs. The combination of pressure-induced alterations in K^+ siphoning machinery in Müller glia and decreased expression of the Na/K-ATPase in RGCs could produce significant disruption of the ion concentration gradients in the glaucomatous retina. Disturbance of K^+ and Na^+ gradients produces elevated K^+ in the immediate extracellular milieu, which presents a challenge for RGCs in the maintenance of their electrochemical gradient. When compounded by IOP-related stress, this could readily produce impairment in spiking ability within these cells. This, in turn, would lead to broader disturbances in K^+ and Na^+ gradients impacting additional surrounding RGCs and so on. Furthermore, this mechanism could be relevant for neurodegenerative diseases broadly that also present with spatial spreading of degeneration.

Future Directions

Our studies suggest that ocular hypertension shifts the expression profile of K^+ channels implicated in K^+ siphoning in Müller glia. However, certain genes that displayed altered expression through transcriptome analysis in whole retina did not show a significant change in expression in primary, purified Müller glia cultures. Our transcriptome analysis identified significant downregulation of *Kcnj6*, *Kcnj12, Kcnj14*, *Kcnk1*, and *Kcnk12* in retina from microbead-injected eyes, but qPCR analysis of these genes in cultured Müller glia revealed a lack of expression or no change in expression following exposure to elevated pressure. Additional experiments on the expression of these genes in other cell types in the retina could elucidate the impact of pressure-induced downregulation of these genes in the retina. For example, qPCR analysis for the *Kcnj* and *Kcnk* genes families on RNA isolated from primary, purified cultures of RGCs, astrocytes, or other cell types known to express these channels that have been exposed to ambient or elevated pressure.

Several studies have shown that elevated pressure *in vitro* and *in vivo* leads to apoptosis of RGCs.[172,173] We found that 48 hours of elevated pressure increases cytotoxicity, but not apoptosis, in Müller glia cultures. This pressure-induced increase in LDH release, and therefore cytotoxicity, in Müller glia is a novel finding. Future directions for these studies should investigate the nature, source and significance of Müller glia cytotoxicity in response to glaucoma-related stressors. Experiments could be performed to examine potential causes of pressure-induced membrane permeability in Müller glia, such as oxidative stress, by inhibiting these mechanisms during pressure elevation and measuring LDH release into the culture media. Increased permeability of the membrane, like that observed with cytotoxicity, can release intercellular contents that have inflammatory and potentially, detrimental effects on surrounding cells.[206] As discussed in the Chapter 1, cytotoxic responses from one cell can affect the health and viability of neighboring cells and perpetuate inflammatory and pathological processes.[92] The significance of Müller glia cytotoxicity on other cells in the retina could be examined by co-culturing Müller glia and RGCs and measuring the levels of apoptosis in RGCs following pressure elevation.

Future studies could evaluate the contribution of Müller glia-regulated ion homeostasis to glaucoma-related changes in RGC physiology. These experiments could involve inhibition of K^+

channels in Müller glia, such as Kir4.1 and Kir2.1, during electrophysiological recordings in whole retina. Whole-cell patch-clamp recordings from RGCs while inhibiting K^+ siphoning machinery in Müller glia would provide information on whether disrupted K^+ siphoning by Müller glia contributes to altered physiological activity of RGCs during glaucoma.

Exposure to elevated pressure in cultured RGCs induces an early reduction in available Na/K-ATPase via activation of endocytosis and degradation pathways. Phosphorylation of the Na/K-ATPase by PKC initiates the endocytosis pathway.[140-143] Following endocytosis, the Na/K-ATPase is degraded by the proteasome.[140,141] One possible mechanism for how elevated pressure induces activation of these pathways is through intracellular Ca^{2+} signaling. PKC is activated by diacylglycerol and intracellular Ca^{2+}.[208] One of the earliest events in RGC degeneration during glaucoma is intracellular Ca^{2+} dysregulation.[3,178] Increased intracellular Ca^{2+} levels, via TRPV1 signaling, are found in primary, purified RGC cultures after exposure to only 1 hour of elevated pressure.[173] Early activation of intracellular Ca^{2+} signaling in response to elevated pressure could activate PKC singling in RGCs, resulting in activation of the Na/K-ATPase endocytosis pathway. This potential mechanism could be tested by inhibiting the TRPV1 channel during pressure elevation in RGC cultures and measuring Na/K-ATPase expression via immunohistochemistry and cation influx via thallium flux imaging.

Early pressure-induced cation dyshomeostasis occurs because of reduced inward cation flux due to reduced Na/K-ATPase activity via endocytosis and degradation. Retention of the Na/K-ATPase at the plasma membrane, by inhibiting either endocytosis or degradation, is sufficient to prevent pressure-induced decreases in cation influx. The electrophysiological deficits seen in glaucomatous RGCs appear to arise from elongation of the repolarization phase of the action potential, which is in part mediated by activity of the Na/K-ATPase. Altered cation influx and repolarization phase phenotypes seen in glaucomatous RGCs can be reproduced in healthy RGCs by pharmacologically inhibiting the Na/K-ATPase. It would therefore be interesting to examine whether increasing Na/K-ATPase activity, by inhibiting endocytosis or degradation, during pressure elevation could counteract repolarization phase phenotypes observed in glaucomatous RGCs. This could be examined by treating RGC cultures with bisindolylmaleimide or MG-132, while exposing them to either ambient or elevated pressure for 4 hours, and then performing whole-cell patch-clamp electrophysiological recordings to measure spiking frequency and amplitude, as well as action potential dynamics.

Our data clearly demonstrate a link between compromised axon transport, impaired physiological activity, and Na/K-ATPase-mediated deficiencies in electrochemical homeostasis. However, it is unclear whether pressure-induced reduction in Na/K-ATPase activity is a potential cause, or a response to, RGC compromise. As outlined in previous chapters, K^+ dyshomeostasis in the retina has the potential to act as a propagating agent for electrophysiological impairment and represents a possible etiological factor of spatial clustering of RGC pathology and vision loss. Future studies will aim to determine whether Na/K-ATPase-mediated disruption of K^+ homeostasis 1) leads to electrophysiological impairment that spreads to neighboring RGCs and 2) contributes to topographical spread of axonopathy and vision loss in the retina.

Experiments to test this hypothesis would involve long-term perturbation of K^+ homeostasis in the Microbead Occlusion Model with AAV-mediated gene therapy or pharmacological approaches to target the Na/K-ATPase. We would then determine whether changes in K^+ homeostasis leads to electrophysiological impairment by examining outcome measures of RGC physiology. Using the graphene-based microfluidic device outlined in Chapter 4, we could map glaucoma-related changes in electrical activity across the retina to discern the pattern of these changes relative to the pattern of axon transport deficits. These experiments would provide real-time spatial and temporal mapping of ion flux, and thus, electrical activity of individual cells, as well as the entire intact retina. Next, we would determine whether changes in K^+ homeostasis leads to alterations in the spatiotemporal progression of axon transport deficits, through CTB tracing, as well as axon degeneration, through measurement of optic nerve morphology and axon density with histological techniques. Finally, we would determine whether changes in K^+ homeostasis are associated with diminished visual function, with the use of flash visual evoked potentials and optokinetic reflex tests.

Conclusions

Altogether, these data indicate that ion dyshomeostasis contributes to electrophysiological deficits seen in glaucomatous RGCs, and may play a role in the spatiotemporal progression of RGC axonopathy during glaucoma. Pressure-induced changes in expression profiles of Kir and K2P channels were seen in mice with ocular hypertension, as well as in Müller glia cultures exposed to pressure elevation. Pressure elevation in Müller glia cultures additionally resulted in cytotoxicity, altered ion homeostasis, and reduced cation flux. Our findings have implications for the response by Müller glia to a glaucoma-related stressor, such as elevated pressure. Additionally, modulation of K^+ siphoning machinery in Müller glia and altered cation homeostasis has implications for electrophysiological impairment noted in RGCs of glaucomatous retina. These electrophysiological deficits in glaucomatous RGCs include reduced ability to maintain induced-spiking frequency and an elongation of the repolarization phase of the action potential. We identify reduced Na/K-ATPase activity and resulting ion dyshomeostasis as the cause of these early electrophysiological deficits.

Pharmacological inhibition of the Na/K-ATPase is sufficient to replicate pressure-induced cation influx and repolarization phase phenotypes in healthy RGCs. As a whole, these results suggest that pressure-induced deficits in axon transport are accompanied by impaired electrophysiology function of RGCs that arises from failure to maintain electrochemical gradients. Therefore, there is potential for ion dyshomeostasis to act as a propagating agent for electrophysiological impairment in neighboring RGCs. Together, our findings have significant implications for our understanding of spatial clustering of pathology in RGCs during glaucoma, as well as spatial clustering noted in several other neurodegenerative disorders.

REFERENCES

1 Quigley, H. A. & Broman, A. T. The number of people with glaucoma worldwide in 2010 and 2020. *Br J Ophthalmol* **90**, 262-267, doi:10.1136/bjo.2005.081224 (2006).

2 Quigley, H. A. & Vitale, S. Models of Open-Angle Glaucoma Prevelance and Incidence in the United States. *IOVS* **38**, 83-91 (1997).

3 Calkins, D. J. Critical pathogenic events underlying progression of neurodegeneration in glaucoma. *Prog Retin Eye Res* **31**, 702-719, doi:10.1016/j.preteyeres.2012.07.001 (2012).

4 Quigley, H. A. Early detection of glaucomatous damage. II. Changes in the appearance of the optic disk. *Surv Ophthalmol* **30**, 111, 117-126 (1985).

5 Hood, D. C. & Kardon, R. H. A framework for comparing structural and functional measures of glaucomatous damage. *Prog Retin Eye Res* **26**, 688-710, doi:10.1016/j.preteyeres.2007.08.001 (2007).

6 Bourne, R. R. The optic nerve head in glaucoma. *Community Eye Health* **25**, 55-57 (2012).

7 Yaqub, M. Visual fields interpretation in glaucoma: a focus on static automated perimetry. *Community Eye Health* **25**, 1-8 (2012).

8 Levin, L. A. Relevance of the site of injury of glaucoma to neuroprotective strategies. *Surv Ophthalmol* **45 Suppl 3**, S243-249; discussion S273-246 (2001).

9 Burgoyne, C. F., Downs, J. C., Bellezza, A. J., Suh, J. K. & Hart, R. T. The optic nerve head as a biomechanical structure: a new paradigm for understanding the role of IOP-related stress and strain in the pathophysiology of glaucomatous optic nerve head damage. *Prog Retin Eye Res* **24**, 39-73, doi:10.1016/j.preteyeres.2004.06.001 (2005).

10 Hollands, H. *et al.* Do findings on routine examination identify patients at risk for primary open-angle glaucoma? The rational clinical examination systematic review. *JAMA* **309**, 2035-2042, doi:10.1001/jama.2013.5099 (2013).

11 Shields, M. B. Normal-tension glaucoma: is it different from primary open-angle glaucoma? *Curr Opin Ophthalmol* **19**, 85-88, doi:10.1097/ICU.0b013e3282f3919b (2008).

12 Weinreb, R. N., Aung, T. & Medeiros, F. A. The pathophysiology and treatment of glaucoma: a review. *JAMA* **311**, 1901-1911, doi:10.1001/jama.2014.3192 (2014).

13 Crish, S. D. & Calkins, D. J. Neurodegeneration in glaucoma: progression and calcium-dependent intracellular mechanisms. *Neuroscience* **176**, 1-11, doi:10.1016/j.neuroscience.2010.12.036 (2011).

14 Freddo, T. F. & Gong, H. Etiology of Iop Elevation in Primary Open Angle Glaucoma. *Optom Glaucoma Soc E J* **4** (2009).

15 Iester, M., De Feo, F. & Douglas, G. R. Visual field loss morphology in high- and normal-tension glaucoma. *J Ophthalmol* **2012**, 327326, doi:10.1155/2012/327326 (2012).

16 Sappington, R. M., Carlson, B. J., Crish, S. D. & Calkins, D. J. The microbead occlusion model: a paradigm for induced ocular hypertension in rats and mice. *Invest Ophthalmol Vis Sci* **51**, 207-216, doi:10.1167/iovs.09-3947 (2010).

17 Salmon, J. F. Predisposing factors for chronic angle-closure glaucoma. *Prog Retin Eye Res* **18**, 121-132 (1999).

18 Nongpiur, M. E., Ku, J. Y. & Aung, T. Angle closure glaucoma: a mechanistic review. *Curr Opin Ophthalmol* **22**, 96-101, doi:10.1097/ICU.0b013e32834372b9 (2011).

19 Heijl, A. *et al.* Reduction of intraocular pressure and glaucoma progression: results from the Early Manifest Glaucoma Trial. *Arch Ophthalmol* **120**, 1268-1279 (2002).

20 Albon, J., Karwatowski, W. S., Avery, N., Easty, D. L. & Duance, V. C. Changes in the collagenous matrix of the aging human lamina cribrosa. *Br J Ophthalmol* **79**, 368-375 (1995).

21 Anderson, M. G. *et al.* Mutations in genes encoding melanosomal proteins cause pigmentary glaucoma in DBA/2J mice. *Nat Genet* **30**, 81-85, doi:10.1038/ng794 (2002).

22 John, S. W. *et al.* Essential iris atrophy, pigment dispersion, and glaucoma in DBA/2J mice. *Invest Ophthalmol Vis Sci* **39**, 951-962 (1998).

23 Libby, R. T. *et al.* Inherited glaucoma in DBA/2J mice: pertinent disease features for studying the neurodegeneration. *Vis Neurosci* **22**, 637-648, doi:10.1017/S0952523805225130 (2005).

24 Bouhenni, R. A., Dunmire, J., Sewell, A. & Edward, D. P. Animal models of glaucoma. *J Biomed Biotechnol* **2012**, 692609, doi:10.1155/2012/692609 (2012).

25 Johnson, T. V. & Tomarev, S. I. Rodent models of glaucoma. *Brain Res Bull* **81**, 349-358, doi:10.1016/j.brainresbull.2009.04.004 (2010).

26 Levkovitch-Verbin, H. *et al.* Translimbal laser photocoagulation to the trabecular meshwork as a model of glaucoma in rats. *Invest Ophthalmol Vis Sci* **43**, 402-410 (2002).

27 Ito, Y. A., Belforte, N., Cueva Vargas, J. L. & Di Polo, A. A Magnetic Microbead Occlusion Model to Induce Ocular Hypertension-Dependent Glaucoma in Mice. *J Vis Exp*, e53731, doi:10.3791/53731 (2016).

28 Garcia-Valenzuela, E., Shareef, S., Walsh, J. & Sharma, S. C. Programmed cell death of retinal ganglion cells during experimental glaucoma. *Exp Eye Res* **61**, 33-44 (1995).

29 Morrison, J. C. *et al.* A rat model of chronic pressure-induced optic nerve damage. *Exp Eye Res* **64**, 85-96, doi:10.1006/exer.1996.0184 (1997).

30 WoldeMussie, E., Ruiz, G., Wijono, M. & Wheeler, L. A. Neuroprotection of retinal ganglion cells by brimonidine in rats with laser-induced chronic ocular hypertension. *Invest Ophthalmol Vis Sci* **42**, 2849-2855 (2001).

31 Bond, W. S. *et al.* Virus-mediated EpoR76E Therapy Slows Optic Nerve Axonopathy in Experimental Glaucoma. *Mol Ther*, doi:10.1038/mt.2015.198 (2015).

32 Della Santina, L., Inman, D. M., Lupien, C. B., Horner, P. J. & Wong, R. O. Differential progression of structural and functional alterations in distinct retinal ganglion cell types in a mouse model of glaucoma. *J Neurosci* **33**, 17444-17457, doi:10.1523/JNEUROSCI.5461-12.2013 (2013).

33 Ward, N. J., Ho, K. W., Lambert, W. S., Weitlauf, C. & Calkins, D. J. Absence of transient receptor potential vanilloid-1 accelerates stress-induced axonopathy in the optic projection. *J Neurosci* **34**, 3161-3170, doi:10.1523/JNEUROSCI.4089-13.2014 (2014).

34 Goldblum, D. & Mittag, T. Prospects for relevant glaucoma models with retinal ganglion cell damage in the rodent eye. *Vision Res* **42**, 471-478 (2002).

35 Pang, I. H. & Clark, A. F. Rodent models for glaucoma retinopathy and optic neuropathy. *J Glaucoma* **16**, 483-505, doi:10.1097/IJG.0b013e3181405d4f (2007).

36 Chang, B. *et al.* Interacting loci cause severe iris atrophy and glaucoma in DBA/2J mice. *Nat Genet* **21**, 405-409, doi:10.1038/7741 (1999).

37 Ritch, R. Exfoliation syndrome: more than meets the eye. *Acta Ophthalmol Scand* **80**, 465-467 (2002).

38 Inman, D. M., Sappington, R., Horner, P. J. & Calkins, D. J. Quantitative correlation of optic nerve pathology with ocular pressure and corneal thickness in the DBA/2 mouse model of glaucoma. *IOVS* **47**, 986-996 (2006).

39 Chevalier-Larsen, E. & Holzbaur, E. L. Axonal transport and neurodegenerative disease. *Biochim Biophys Acta* **1762**, 1094-1108, doi:10.1016/j.bbadis.2006.04.002 (2006).

40 De Vos, K. J., Grierson, A. J., Ackerley, S. & Miller, C. C. Role of axonal transport in neurodegenerative diseases. *Annu Rev Neurosci* **31**, 151-173, doi:10.1146/annurev.neuro.31.061307.090711 (2008).

41 Millecamps, S. & Julien, J. P. Axonal transport deficits and neurodegenerative diseases. *Nat Rev Neurosci* **14**, 161-176, doi:10.1038/nrn3380 (2013).

42 Roy, S., Zhang, B., Lee, V. M. & Trojanowski, J. Q. Axonal transport defects: a common theme in neurodegenerative diseases. *Acta Neuropathol* **109**, 5-13, doi:10.1007/s00401-004-0952-x (2005).

43 Braak, H., Ghebremedhin, E., Rub, U., Bratzke, H. & Del Tredici, K. Stages in the development of Parkinson's disease-related pathology. *Cell Tissue Res* **318**, 121-134, doi:10.1007/s00441-004-0956-9 (2004).

44 Ebneth, A. *et al.* Overexpression of tau protein inhibits kinesin-dependent trafficking of vesicles, mitochondria, and endoplasmic reticulum: implications for Alzheimer's disease. *J Cell Biol* **143**, 777-794 (1998).

45 Lee, S., Sato, Y. & Nixon, R. A. Lysosomal proteolysis inhibition selectively disrupts axonal transport of degradative organelles and causes an Alzheimer's-like axonal dystrophy. *J Neurosci* **31**, 7817-7830, doi:10.1523/JNEUROSCI.6412-10.2011 (2011).

46 El-Danaf, R. N. & Huberman, A. D. Characteristic patterns of dendritic remodeling in early-stage glaucoma: evidence from genetically identified retinal ganglion cell types. *J Neurosci* **35**, 2329-2343, doi:10.1523/JNEUROSCI.1419-14.2015 (2015).

47 Risner, M. L., Pasini, S., Cooper, M. L., Lambert, W. S. & Calkins, D. J. Axogenic mechanism enhances retinal ganglion cell excitability during early progression in glaucoma. *Proc Natl Acad Sci U S A* **115**, E2393-E2402, doi:10.1073/pnas.1714888115 (2018).

48 Jakobs, T. C., Libby, R. T., Ben, Y., John, S. W. & Masland, R. H. Retinal ganglion cell degeneration is topological but not cell type specific in DBA/2J mice. *J Cell Biol* **171**, 313-325, doi:10.1083/jcb.200506099 (2005).

49 Stevens, B. *et al.* The classical complement cascade mediates CNS synapse elimination. *Cell* **131**, 1164-1178, doi:10.1016/j.cell.2007.10.036 (2007).

50 Crish, S. D., Sappington, R. M., Inman, D. M., Horner, P. J. & Calkins, D. J. Distal axonopathy with structural persistence in glaucomatous neurodegeneration. *Proc Natl Acad Sci U S A* **107**, 5196-5201, doi:10.1073/pnas.0913141107 (2010).

51 Maday, S., Twelvetrees, A. E., Moughamian, A. J. & Holzbaur, E. L. Axonal transport: cargo-specific mechanisms of motility and regulation. *Neuron* **84**, 292-309, doi:10.1016/j.neuron.2014.10.019 (2014).

52 DiStefano, P. S. *et al.* The neurotrophins BDNF, NT-3, and NGF display distinct patterns of retrograde axonal transport in peripheral and central neurons. *Neuron* **8**, 983-993 (1992).

53 Saxton, W. M. & Hollenbeck, P. J. The axonal transport of mitochondria. *J Cell Sci* **125**, 2095-2104, doi:10.1242/jcs.053850 (2012).
54 Buckingham, B. P. *et al.* Progressive ganglion cell degeneration precedes neuronal loss in a mouse model of glaucoma. *J Neurosci* **28**, 2735-2744, doi:10.1523/JNEUROSCI.4443-07.2008 (2008).
55 Wilson, G. N., Smith, M. A., Inman, D. M., Dengler-Crish, C. M. & Crish, S. D. Early Cytoskeletal Protein Modifications Precede Overt Structural Degeneration in the DBA/2J Mouse Model of Glaucoma. *Front Neurosci* **10**, 494, doi:10.3389/fnins.2016.00494 (2016).
56 Lye-Barthel, M., Sun, D. & Jakobs, T. C. Morphology of astrocytes in a glaucomatous optic nerve. *Invest Ophthalmol Vis Sci* **54**, 909-917, doi:10.1167/iovs.12-10109 (2013).
57 Kitaoka, Y. *et al.* Axonal protection by Nmnat3 overexpression with involvement of autophagy in optic nerve degeneration. *Cell Death Dis* **4**, e860, doi:10.1038/cddis.2013.391 (2013).
58 Lambert, W. S., Ruiz, L., Crish, S. D., Wheeler, L. A. & Calkins, D. J. Brimonidine prevents axonal and somatic degeneration of retinal ganglion cell neurons. *Mol Neurodegener* **6**, 4, doi:10.1186/1750-1326-6-4 (2011).
59 Cavanagh, J. B. The 'dying back' process. A common denominator in many naturally occurring and toxic neuropathies. *Archives of Pathology & Laboratory Medicine* **103**, 659-664 (1979).
60 Coleman, M. Axon degeneration mechanisms: commonality amid diversity. *Nature Reviews Neuroscience* **6**, 889-898 (2005).
61 Spencer, P. S. & Schaumburg, H. H. Central-peripheral distal axonopathy - The pathogenesis of dying-back polyneuropathies *Prog. Neuropathol* **3**, 253-295 (1976).
62 Conforti, L., Gilley, J. & Coleman, M. P. Wallerian degeneration: an emerging axon death pathway linking injury and disease. *Nature Reviews Neuroscience* **15**, 394-409 (2014).
63 Griffin, J. W., George, E. B., Hsieh, S.-T. & Glass, J. D. in *The Axon: Structure, Function, and Pathophysiology* (eds Stephen G. Waxman, Jeffery D. Kocsis, & Peter K. Stys) 3750-3790 (Oxford University Press, 1995).
64 Wang, J. T., Medress, Z. A. & Barres, B. A. Axon degeneration: Molecular mechanisms of a self-destruction pathway. *J. Cell Biol.* **196**, 7-18 (2012).
65 Schlamp, C. L., Li, Y., Dietz, J. A., Janssen, K. T. & Nickells, R. W. Progressive ganglion cell loss and optic nerve degeneration in DBA/2J mice is variable and asymmetric. *BMC Neurosci* **7**, 66, doi:10.1186/1471-2202-7-66 (2006).
66 Beirowski, B., Babetto, E., Coleman, M. P. & Martin, K. R. The WldS gene delays axonal but not somatic degeneration in a rat glaucoma model. *Eur J Neurosci* **28**, 1166-1179, doi:10.1111/j.1460-9568.2008.06426.x (2008).
67 Heiduschka, P., Julien, S., Schuettauf, F. & Schnichels, S. Loss of retinal function in aged DBA/2J mice – New insights into retinal neurodegeneration. *Exp Eye Res* **91**, 779-783 (2010).
68 Williams, P. A. *et al.* Inhibition of the classical pathway of the complement cascade prevents early dendritic and synaptic degeneration in glaucoma. *Mol Neurodegener* **11**, 26, doi:10.1186/s13024-016-0091-6 (2016).

69 Berry, R. H., Qu, J., John, S. W., Howell, G. R. & Jakobs, T. C. Synapse Loss and Dendrite Remodeling in a Mouse Model of Glaucoma. *PLoS One* **10**, e0144341, doi:10.1371/journal.pone.0144341 (2015).

70 Weber, A. J., Kaufman, P. L. & Hubbard, W. C. Morphology of single ganglion cells in the glaucomatous primate retina. *Invest Ophthalmol Vis Sci* **39**, 2304-2320 (1998).

71 Shou, T., Liu, J., Wang, W., Zhou, Y. & Zhao, K. Differential dendritic shrinkage of alpha and beta retinal ganglion cells in cats with chronic glaucoma. *Invest Ophthalmol Vis Sci* **44**, 3005-3010 (2003).

72 Feng, L. *et al.* Sustained ocular hypertension induces dendritic degeneration of mouse retinal ganglion cells that depends on cell type and location. *Invest Ophthalmol Vis Sci* **54**, 1106-1117, doi:10.1167/iovs.12-10791 (2013).

73 Qu, J., Wang, D. & Grosskreutz, C. L. Mechanisms of retinal ganglion cell injury and defense in glaucoma. *Exp Eye Res* **91**, 48-53, doi:10.1016/j.exer.2010.04.002 (2010).

74 Ashkenazi, A. & Dixit, V. M. Death receptors: signaling and modulation. *Science* **281**, 1305-1308 (1998).

75 Yang, X., Chang, H. Y. & Baltimore, D. Autoproteolytic activation of pro-caspases by oligomerization. . *Mol. Cell.* **1**, 319-325 (1998).

76 Hirata, H. *et al.* Caspases are activated in a branched protease cascade and control distinct downstream processes in Fas-induced apoptosis. *J. Exp. Med.* **187**, 587-600 (1998).

77 Slee, E. A. *et al.* Ordering the cytochrome c-initiated caspase cascade: hierarchical activation of caspases-2, -3, -6, -7, -8, and -10 in a caspase-9-dependent manner. *J. Cell. Biol.* **144**, 281-292 (1999).

78 Kim, H. S. & Park, C. K. Retinal ganglion cell death is delayed by activation of retinal intrinsic cell survival program. *Brain Res* **1057**, 17-28, doi:10.1016/j.brainres.2005.07.005 (2005).

79 Nakazawa, T. *et al.* Tumor necrosis factor-alpha mediates oligodendrocyte death and delayed retinal ganglion cell loss in a mouse model of glaucoma. *J Neurosci* **26**, 12633-12641, doi:10.1523/JNEUROSCI.2801-06.2006 (2006).

80 Huang, W. *et al.* Transcriptional up-regulation and activation of initiating caspases in experimental glaucoma. *Am J Pathol* **167**, 673-681, doi:10.1016/S0002-9440(10)62042-1 (2005).

81 McKinnon, S. J. *et al.* Caspase activation and amyloid precursor protein cleavage in rat ocular hypertension. *Invest Ophthalmol Vis Sci* **43**, 1077-1087 (2002).

82 Green, D. R. & Reed, J. C. Mitochondria and apoptosis. *Science* **281** (1998).

83 Nunez, G., Benedict, M. A., Hu, Y. & Inohara, N. Caspases: the proteases of the apoptotic pathway. *Onocgene* **17**, 3237-3245 (1998).

84 Li, P. *et al.* Cytochrome c and dATP-dependent formation of Apaf-1/caspase-9 complex initiates an apoptotic protease cascade. *Cell* **91**, 479-489 (1997).

85 Srinivasula, S. M., Ahmad, M., Fernandes-Alnemri, T. & Alnemri, E. S. Autoactivation of procaspase-9 by Apaf-1-mediated oligomerization. *Mol. Cell.* **1**, 949-957 (1998).

86 Zou, H., Li, Y., Liu, X. & Wang, X. An APAF-1.cytochrome c multimeric complex is a functional apoptosome that activates procaspase-9. *J. Biol. Chem.* **274**, 11549-11556 (1999).

87 Libby, R. T. *et al.* Susceptibility to neurodegeneration in a glaucoma is modified by Bax gene dosage. *PLoS Genet* **1**, 17-26, doi:10.1371/journal.pgen.0010004 (2005).

88 Bossy-Wetzel, E., Schwarzenbacher, R. & Lipton, S. A. Molecular pathways to neurodegeneration. *Nat Med* **10 Suppl**, S2-9, doi:10.1038/nm1067 (2004).

89 Lin, Y. C. & Koleske, A. J. Mechanisms of synapse and dendrite maintenance and their disruption in psychiatric and neurodegenerative disorders. *Annu Rev Neurosci* **33**, 349-378, doi:10.1146/annurev-neuro-060909-153204 (2010).

90 Masliah, E., Crews, L. & Hansen, L. Synaptic remodeling during aging and in Alzheimer's disease. *Journal of Alzheimer's Disease* (2006).

91 Wishart, T. M., Parson, S. H. & Gillingwater, T. H. Synaptic vulnerability in neurodegenerative disease. *J Neuropathol Exp Neurol* **65**, 733-739 (2006).

92 Friedlander, R. M. Apoptosis and Caspases in Neurodegenerative Diseases. *New England Journal of Medicine* **348** (2003).

93 Mattson, M. P. Apoptosis in neurodegenerative disorders. *Nature Reviews Molecular Cell Biology* **1** (2000).

94 Formichella, C. R., Abella, S. K., Sims, S. M., Cathcart, H. M. & Sappington, R. M. Astrocyte Reactivity: A Biomarker for Retinal Ganglion Cell Health in Retinal Neurodegeneration. *J Clin Cell Immunol* **5**, doi:10.4172/2155-9899.1000188 (2014).

95 Soto, I. *et al.* Retinal ganglion cell loss in a rat ocular hypertension model is sectorial and involves early optic nerve axon loss. *Invest Ophthalmol Vis Sci* **52**, 434-441, doi:10.1167/iovs.10-5856 (2011).

96 Echevarria, F. D., Formichella, C. R. & Sappington, R. M. Interleukin-6 Deficiency Attenuates Retinal Ganglion Cell Axonopathy and Glaucoma-Related Vision Loss. *Front Neurosci* **11**, 318, doi:10.3389/fnins.2017.00318 (2017).

97 Drance, S. M. The early field defects in glaucoma. *Invest Ophthalmol* **8** (1969).

98 Mikelberg, F. S. & Drance, S. M. The Mode of Progression of Visual Field Defects in Glaucoma. *American Journal of Ophthalmology* **98**, 443-445, doi:10.1016/0002-9394(84)90128-4 (1984).

99 Mikelberg, F. S., Schulzer, M., Drance, S. M. & Lau, W. The Rate of Progression of Scotomas in Glaucoma. *American Journal of Ophthalmology* **101**, 1-6, doi:10.1016/0002-9394(86)90457-5 (1986).

100 Werner, E. B. & Drance, S. M. Early visual field disturbances in glaucoma. *Arch Ophthalmol* **95** (1977).

101 Broadway, D. C. Visual field testing for glaucoma - a practical guide. *Community Eye Health* **25**, 66-70 (2012).

102 Kerrigan-Baumrind, L. A., Quigley, H., Pease, M. E., Kerrigan, D. F. & MItchell, R. S. Number of ganglion cells in glaucoma eyes compared with threshold visual field tests in the same persons. *IOVS* **41** (200).

103 Medeiros, F. A. *et al.* Retinal ganglion cell count estimates associated with early development of visual field defects in glaucoma. *Ophthalmology* **120**, 736-744, doi:10.1016/j.ophtha.2012.09.039 (2013).

104 Douglas, R. M. *et al.* Independent visual threshold measurements in the two eyes of freely moving rats and mice using a virtual-reality optokinetic system. *Vis Neurosci* **22**, 677-684, doi:10.1017/S0952523805225166 (2005).

105 Thomas, B. B., Seiler, M. J., Sadda, S. R., Coffey, P. J. & Aramant, R. B. Optokinetic test to evaluate visual acuity of each eye independently. *J Neurosci Methods* **138**, 7-13, doi:10.1016/j.jneumeth.2004.03.007 (2004).

106 Tong, J., Wang, J. & Sun, F. Dual-directional optokinetic nystagmus elicited by the intermittent display of gratings in primary open-angle glaucoma and normal eyes. *Curr Eye Res* **25**, 355-362 (2002).

107 Feng, L. *et al.* Long-Term Protection of Retinal Ganglion Cells and Visual Function by Brain-Derived Neurotrophic Factor in Mice With Ocular Hypertension. *Invest Ophthalmol Vis Sci* **57**, 3793-3802, doi:10.1167/iovs.16-19825 (2016).

108 Burroughs, S. L., Kaja, S. & Koulen, P. Quantification of deficits in spatial visual function of mouse models for glaucoma. *Invest Ophthalmol Vis Sci* **52**, 3654-3659, doi:10.1167/iovs.10-7106 (2011).

109 Rangarajan, K. V. *et al.* Detection of visual deficits in aging DBA/2J mice by two behavioral assays. *Curr Eye Res* **36**, 481-491, doi:10.3109/02713683.2010.549600 (2011).

110 Crish, S. D. *et al.* Failure of axonal transport induces a spatially coincident increase in astrocyte BDNF prior to synapse loss in a central target. *Neuroscience* **229**, 55-70, doi:10.1016/j.neuroscience.2012.10.069 (2013).

111 Echevarria, F., Walker, C., Abella, S., Won, M. & Sappington, R. Stressor-dependent Alterations in Glycoprotein 130: Implications for Glial Cell Reactivity, Cytokine Signaling and Ganglion Cell Health in Glaucoma. *J Clin Exp Ophthalmol* **4** (2013).

112 Soto, I. *et al.* Retinal ganglion cells downregulate gene expression and lose their axons within the optic nerve head in a mouse glaucoma model. *J Neurosci* **28**, 548-561, doi:10.1523/JNEUROSCI.3714-07.2008 (2008).

113 Armstrong, R. A. & Cairns, N. J. Different molecular pathologies result in similar spatial patterns of cellular inclusions in neurodegenerative disease: a comparative study of eight disorders. *J Neural Transm (Vienna)* **119**, 1551-1560, doi:10.1007/s00702-012-0838-3 (2012).

114 Armstrong, R. A., Cairns, N. J. & Lantos, P. L. What does the study of the spatial patterns of pathological lesions tell us about the pathogenesis of neurodegenerative disorders? *Neuropathology : official journal of the Japanese Society of Neuropathology* **21**, 1-12 (2001).

115 Pang, J. J., Frankfort, B. J., Gross, R. L. & Wu, S. M. Elevated intraocular pressure decreases response sensitivity of inner retinal neurons in experimental glaucoma mice. *Proc Natl Acad Sci U S A* **112**, 2593-2598, doi:10.1073/pnas.1419921112 (2015).

116 Chen, H. *et al.* Progressive Degeneration of Retinal and Superior Collicular Functions in Mice With Sustained Ocular Hypertension. *Invest Ophthalmol Vis Sci* **56**, 1971-1984, doi:10.1167/ (2015).

117 Porciatti, V. Electrophysiological assessment of retinal ganglion cell function. *Exp Eye Res* **141**, 164-170, doi:10.1016/j.exer.2015.05.008 (2015).

118 Jafarzadehpour, E., Radinmehr, F., Pakravan, M., Mirzajani, A. & Yazdani, S. Pattern electroretinography in glaucoma suspects and early primary open angle glaucoma. *J Ophthalmic Vis Res* **8**, 199-206 (2013).

119 Parisi, V., Miglior, S., Manni, G., Centofanti, M. & Bucci, M. G. Clinical ability of pattern electroretinograms and visual evoked potentials in detecting visual dysfunction in ocular hypertension and glaucoma. *Ophthalmology* **113**, 216-228, doi:10.1016/j.ophtha.2005.10.044 (2006).

120 Domenici, L. *et al.* Rescue of retinal function by BDNF in a mouse model of glaucoma. *PLoS One* **9**, e115579, doi:10.1371/journal.pone.0115579 (2014).

121 Saleh, M., Nagaraju, M. & Porciatti, V. Longitudinal evaluation of retinal ganglion cell function and IOP in the DBA/2J mouse model of glaucoma. *Invest Ophthalmol Vis Sci* **48**, 4564-4572, doi:10.1167/iovs.07-0483 (2007).

122 Alsarraf, O. *et al.* Acetylation preserves retinal ganglion cell structure and function in a chronic model of ocular hypertension. *Invest Ophthalmol Vis Sci* **55**, 7486-7493, doi:10.1167/iovs.14-14792 (2014).

123 Holcombe, D. J., Lengefeld, N., Gole, G. A. & Barnett, N. L. Selective inner retinal dysfunction precedes ganglion cell loss in a mouse glaucoma model. *Br J Ophthalmol* **92**, 683-688, doi:10.1136/bjo.2007.133223 (2008).

124 Sullivan, T. A., Geisert, E. E., Hines-Beard, J. & Rex, T. S. Systemic adeno-associated virus-mediated gene therapy preserves retinal ganglion cells and visual function in DBA/2J glaucomatous mice. *Hum Gene Ther* **22**, 1191-1200, doi:10.1089/hum.2011.052 (2011).

125 Sehi, M., Grewal, D. S., Goodkin, M. L. & Greenfield, D. S. Reversal of retinal ganglion cell dysfunction after surgical reduction of intraocular pressure. *Ophthalmology* **117**, 2329-2336, doi:10.1016/j.ophtha.2010.08.049 (2010).

126 Blanco, G. & Mercer, R. W. Isozymes of the Na-K-ATPase: heterogeneity in structure, diversity in function. *American Journal of Physiology* (1998).

127 Kofuji, P. & Newman, E. A. Potassium buffering in the central nervous system. *Neuroscience* **129**, 1045-1056, doi:10.1016/j.neuroscience.2004.06.008 (2004).

128 Newman, E. A. Distribution of potassium conductance in mammalian muller (glial) cells: a comparative study. *J Neurosci* **7**, 2423-2432 (1987).

129 Reichenbach, A. & Bringmann, A. New functions of Muller cells. *Glia* **61**, 651-678, doi:10.1002/glia.22477 (2013).

130 Geering, K. Functional roles of Na,K-ATPase subunits. *Current Opinion in Nephrology and Hypertension* **17**, 526-532 (2008).

131 McGrail, K. M. & Sweadner, K. J. lmmunofluorescent Localization of Two Different Na,K-ATPases in the Rat Retina and in Identified Dissociated Retinal Cells. *The Journal of Neuroscience* **6**, 1272-1283 (1986).

132 Wetzel, R. K., Arystarkhova, E. & Sweadner, K. J. Cellular and Subcellular Specification of Na,K-ATPase a and B Isoforms in the Postnatal Development of Mouse Retina. *The Journal of Neuroscience* **19**, 9878-9889 (1999).

133 Golubnitschaja, O., Yeghiazaryan, K. & Flammer, J. Key molecular pathways affected by glaucoma pathology: is predictive diagnosis possible? *EPMA J* **1**, 237-244, doi:10.1007/s13167-010-0031-4 (2010).

134 Wong, V. H., Bui, B. V. & Vingrys, A. J. Clinical and experimental links between diabetes and glaucoma. *Clin Exp Optom* **94**, 4-23, doi:10.1111/j.1444-0938.2010.00546.x (2011).

135 Ellis, D. Z., Rabe, J. & Sweadner, K. J. Global Loss of Na,K-ATPase and Its Nitric Oxide-Mediated Regulation in a Transgenic Mouse Model of Amyotrophic Lateral Sclerosis. *J Neurosci* **23**, 43-51 (2003).

136 Palladino, M. J., Bower, J. E., Kreber, R. & Ganetzky, B. Neural dysfunction and neurodegeneration in Drosophila Na+/K+ ATPase Alpha Subunit Mutants. *J Neurosci* **23**, 1276-1286 (2003).

137 Golden, W. C., Brambrink, A. M., Traystman, R. J. & Martin, L. J. Failure to sustain recovery of Na,K-ATPase function is a possible mechanism for striatal

neurodegeneration in hypoxic-ischemic newborn piglets. *Molecular Brain Research* **88**, 94-102 (2001).

138 Chibalin, A. V. *et al.* Dopamine-induced endocytosis of Na+,K+-ATPase is initiated by phosphorylation of Ser-18 in the rat alpha subunit and Is responsible for the decreased activity in epithelial cells. *J Biol Chem* **274**, 1920-1927 (1999).

139 Alves, D. S., Farr, G. A., Seo-Mayer, P. & Caplan, M. J. AS160 associates with the Na+,K+-ATPase and mediates the adenosine monophosphate-stimulated protein kinase-dependent regulation of sodium pump surface expression. *Mol Biol Cell* **21**, 4400-4408, doi:10.1091/mbc.E10-06-0507 (2010).

140 Lecuona, E., Sun, H. Y., Vohwinkel, C., Ciechanover, A. & Sznajder, J. I. Ubiquitination Participates in the Lysosomal Degradation of Na,K-ATPase in Steady-State Conditions. *American Journal of Respiratory Cell and Molecular Biology* **41**, 671-679, doi:10.1165/rcmb.2008-0365OC (2009).

141 Magnani, N. D. *et al.* HIF and HOIL-1L-mediated PKCzeta degradation stabilizes plasma membrane Na,K-ATPase to protect against hypoxia-induced lung injury. *Proc Natl Acad Sci U S A* **114**, E10178-E10186, doi:10.1073/pnas.1713563114 (2017).

142 Chibalin, A. V. *et al.* Phosphorylation of the catalyic alpha-subunit constitutes a triggering signal for Na+,K+-ATPase endocytosis. *J Biol Chem* **273**, 8814-8819 (1998).

143 Wang, Y. B. *et al.* Sodium transport is modulated by p38 kinase-dependent cross-talk between ENaC and Na,K-ATPase in collecting duct principal cells. *J Am Soc Nephrol* **25**, 250-259, doi:10.1681/ASN.2013040429 (2014).

144 Barlet-Bas, C., Khadouri, C., Marsy, S. & Doucet, A. Enhanced intracellular sodium concentration in kidney cells recruits a latent pool of Na-K-ATPase whose size is modulated by corticosteroids. *J Biol Chem* **265**, 7799-7803 (1990).

145 Horisberger, J. D. & Rossier, B. C. Aldosterone regulation of gene transcription leading to control of ion transport. *Hypertension* **19**, 221-227 (1992).

146 Bringmann, A. *et al.* Role of Glial K+ Channels in Ontogeny and Gliosis: A hypothesis based upon studies on Muller cells. *Glia* **29**, 35-44 (2000).

147 Jeon, C.-J., Strettoi, E. & Masland, R. H. The Major Cell Populations of the Mouse Retina. *The Journal of Neuroscience* **18**, 8936-8946, doi:10.1523/jneurosci.18-21-08936.1998 (1998).

148 Bringmann, A. *et al.* Muller cells in the healthy and diseased retina. *Prog Retin Eye Res* **25**, 397-424, doi:10.1016/j.preteyeres.2006.05.003 (2006).

149 Karwoski, C. J., Lu, H.-K. & Newman, E. A. Spatial Buffering of Light-Evoked Potassium Increases by Retinal Muller (Glial) Cells. *Science* **244** (1989).

150 Kofuji, P. & Newman, E. A. *Astrocytes in (Patho)Physiology of the Nervous System*. 151-175 (Springer Science + Business Media, LLC, 2009).

151 Butt, A. M. & Kalsi, A. Inwardly rectifying potassium channels (Kir) in central nervous system glia: a special role for Kir4.1 in glial functions. *Journal of Cellular and Molecular Medicine* **10**, 33-44 (2006).

152 Newman, E. A., Frambach, D. A. & Odette, L. L. Control of extracellular potassium levels by retinal glial cell K+ siphoning. *Science* **225**, 1174-1175 (1984).

153 Eberhardt, C., Amann, B., Feuchtinger, A., Hauck, S. M. & Deeg, C. A. Differential expression of inwardly rectifying K+ channels and aquaporins 4 and 5 in autoimmune uveitis indicates misbalance in Muller glial cell-dependent ion and water homeostasis. *Glia* **59**, 697-707, doi:10.1002/glia.21139 (2011).

154 Eaton, M. J. *et al.* Tandem-pore K+ channels display an uneven distribution in amphibian retina. *Glial Cells* **15**, 321-324, doi:10.1097/01.wnr.0000093482.65585.cf (2003).

155 Enyedi, P. & Czirjak, G. Molecular background of leak K+ currents: two-pore domain potassium channels. *Physiol Rev* **90**, 559-605, doi:10.1152/physrev.00029.2009 (2010).

156 Hughes, S., Foster, R. G., Peirson, S. N. & Hankins, M. W. Expression and localisation of two-pore domain (K2P) background leak potassium ion channels in the mouse retina. *Sci Rep* **7**, 46085, doi:10.1038/srep46085 (2017).

157 Pannicke, T. *et al.* Diabetes Alters Osmotic Swelling Characteristics and Membrane Conductance of Glial Cells in Rat Retina. *Diabetes* **55**, 633-639 (2006).

158 Yang, Z. *et al.* Effect of adenosine and adenosine receptor antagonist on Muller cell potassium channel in Rat chronic ocular hypertension models. *Sci Rep* **5**, 11294, doi:10.1038/srep11294 (2015).

159 Zhao, T., Li, Y., Weng, C. & Yin, Z. The changes of potassium currents in RCS rat Muller cell during retinal degeneration. *Brain Res* **1427**, 78-87, doi:10.1016/j.brainres.2011.10.011 (2012).

160 Bolz, S. *et al.* K(+) currents fail to change in reactive retinal glial cells in a mouse model of glaucoma. *Graefes Arch Clin Exp Ophthalmol* **246**, 1249-1254, doi:10.1007/s00417-008-0872-x (2008).

161 Skatchkov, S. N. *et al.* Tandem-pore domain potassium channels are functionally expressed in retinal (Muller) glial cells. *Glia* **53**, 266-276, doi:10.1002/glia.20280 (2006).

162 Feliciangeli, S., Chatelain, F. C., Bichet, D. & Lesage, F. The family of K2P channels: salient structural and functional properties. *J Physiol* **593**, 2587-2603, doi:10.1113/jphysiol.2014.287268 (2015).

163 Sommer, A. Intraocular pressure and glaucoma. *Am J Opthalmol* **107**, 186-188 (1989).

164 Ou, Y., Jo, R. E., Ullian, E. M., Wong, R. O. & Della Santina, L. Selective Vulnerability of Specific Retinal Ganglion Cell Types and Synapses after Transient Ocular Hypertension. *J Neurosci* **36**, 9240-9252, doi:10.1523/JNEUROSCI.0940-16.2016 (2016).

165 Crish, S. D., Sappington, R. M., Inman, D. M., Horner, P. J. & Calkins, D. J. Distal axonopathy with structural persistence in glaucomatous neurodegeneration. *PNAS* **107**, 5196-5201 (2010).

166 Weitlauf, C. *et al.* Short-term increases in transient receptor potential vanilloid-1 mediate stress-induced enhancement of neuronal excitation. *J Neurosci* **34**, 15369-15381, doi:10.1523/JNEUROSCI.3424-14.2014 (2014).

167 Echevarria, F. D., Rickman, A. E. & Sappington, R. M. Interleukin-6: A Constitutive Modulator of Glycoprotein 130, Neuroinflammatory and Cell Survival Signaling in Retina. *J Clin Cell Immunol* **7**, doi:10.4172/2155-9899.1000439 (2016).

168 Wareham, L. K. *et al.* Increased bioavailability of cyclic guanylate monophosphate prevents retinal ganglion cell degeneration. *Neurobiol Dis* **121**, 65-75, doi:10.1016/j.nbd.2018.09.002 (2018).

169 Lee, S. J. *et al.* Pressure-Induced Alterations in PEDF and PEDF-R Expression: Implications for Neuroprotective Signaling in Glaucoma. *J Clin Exp Ophthalmol* **6**, doi:10.4172/2155-9570.1000491 (2015).

170 Sappington, R. M. & Calkins, D. J. Contribution of TRPV1 to microglia-derived IL-6 and NFkappaB translocation with elevated hydrostatic pressure. *Invest Ophthalmol Vis Sci* **49**, 3004-3017, doi:10.1167/iovs.07-1355 (2008).

171 Sappington, R. M. & Calkins, D. J. Pressure-Induced Regulation of IL-6 in Retinal Glial Cells: Involvement of the Ubiquitin/Proteasome Pathway and NF B. *IOVS* **47**, 3860-3869, doi:10.1167/ (2006).

172 Sappington, R. M., Chan, M. & Calkins, D. J. Interleukin-6 protects retinal ganglion cells from pressure-induced death. *Invest Ophthalmol Vis Sci* **47**, 2932-2942, doi:10.1167/iovs.05-1407 (2006).

173 Sappington, R. M., Sidorova, T., Long, D. J. & Calkins, D. J. TRPV1: contribution to retinal ganglion cell apoptosis and increased intracellular Ca2+ with exposure to hydrostatic pressure. *Invest Ophthalmol Vis Sci* **50**, 717-728, doi:10.1167/iovs.08-2321 (2009).

174 Dreyfus, C. F., Friedman, W. J., Markey, K. A. & Black, I. B. Depolarizing stimuli increase tyrosine hydroxylase in the mouse locus coeruleus in culture. *Brain Res* **379**, 216-222 (1986).

175 Ji, M. *et al.* Group I mGluR-Mediated Inhibition of Kir Channels Contributes to Retinal Mu¨ller Cell Gliosis in a Rat Chronic Ocular Hypertension Model. *J Neurosci* **32**, 12744-12755 (2012).

176 Kofuji, P. *et al.* Kir potassium channel subunit expression in retinal glial cells: implications for spatial potassium buffering. *Glia* **39**, 292-303, doi:10.1002/glia.10112 (2002).

177 Fischer, R. A., Roux, A. L., Wareham, L. K. & Sappington, R. M. Pressure-dependent Modulation of Inward-Rectifying K+ Channels: Implications for Cation Homeostasis and K+ Dynamics in Glaucoma. *Am J Physiol Cell Physiol* **317**, C375-C389, doi:10.1152/ajpcell.00444.2018 (2019).

178 Sappington, R. M. *et al.* Activation of transient receptor potential vanilloid-1 (TRPV1) influences how retinal ganglion cell neurons respond to pressure-related stress. *Channels (Austin)* **9**, 102-113, doi:10.1080/19336950.2015.1009272 (2015).

179 Gavrieli, Y., Sherman, Y. & Ben-Sasson, S. A. Identification of programmed cell death in situ via specific labeling of nuclear DNA fragmentation. *The Journal of Cell Biology* **119**, 493-501, doi:10.1083/jcb.119.3.493 (1992).

180 Gorczyca, W., Gong, J. & Darzynkiewicz, Z. Detection of DNA strand breaks in individual apoptotic cell sby the in situ terminal deoxynucleotidyl transferase and nick translation assays. *Cancer Research* **53**, 1945-1951 (1993).

181 Kawano, T., Zhao, P., Nakajima, S. & Nakajima, Y. Single-cell RT-PCR analysis of GIRK channels expressed in rat locus coeruleus and nucleus basalis neurons. *Neurosci Lett* **358**, 63-67, doi:10.1016/j.neulet.2003.12.104 (2004).

182 Millar, I. D., Wang, S., Brown, P. D., Barrand, M. A. & Hladky, S. B. Kv1 and Kir2 potassium channels are expressed in rat brain endothelial cells. *Pflugers Arch* **456**, 379-391, doi:10.1007/s00424-007-0377-1 (2008).

183 Pondugula, S. R. *et al.* Glucocorticoid regulation of genes in the amiloride-sensitive sodium transport pathway by semicircular canal duct epithelium of neonatal rat. *Physiol Genomics* **24**, 114-123, doi:10.1152/physiolgenomics.00006.2005 (2006).

184 Pollema-Mays, S. L., Centeno, M. V., Ashford, C. J., Apkarian, A. V. & Martina, M. Expression of background potassium channels in rat DRG is cell-specific and down-regulated in a neuropathic pain model. *Mol Cell Neurosci* **57**, 1-9, doi:10.1016/j.mcn.2013.08.002 (2013).

185 Marsh, B., Acosta, C., Djouhri, L. & Lawson, S. N. Leak K(+) channel mRNAs in dorsal root ganglia: relation to inflammation and spontaneous pain behaviour. *Mol Cell Neurosci* **49**, 375-386, doi:10.1016/j.mcn.2012.01.002 (2012).

186 Fischer, R. A. *et al.* Impact of Graphene on the Efficacy of Neuron Culture Substrates. *Adv Healthc Mater*, e1701290, doi:10.1002/adhm.201701290 (2018).

187 Ruiz-Ederra, J., Zhang, H. & Verkman, A. S. Evidence against functional interaction between aquaporin-4 water channels and Kir4.1 potassium channels in retinal Muller cells. *J Biol Chem* **282**, 21866-21872, doi:10.1074/jbc.M703236200 (2007).

188 Chen, L., Yu, Y. C., Zhao, J. W. & Yang, X. L. Inwardly rectifying potassium channels in rat retinal ganglion cells. *Eur J Neurosci* **20**, 956-964, doi:10.1111/j.1460-9568.2004.03553.x (2004).

189 Raap, M. *et al.* Diversity of Kir channel subunit mRNA expressed by retinal glial cells of the guinea-pig. *Neuroreport* **13**, 1037-1040 (2002).

190 Ma, L., Zhang, X., Zhou, M. & Chen, H. Acid-sensitive TWIK and TASK two-pore domain potassium channels change ion selectivity and become permeable to sodium in extracellular acidification. *J Biol Chem* **287**, 37145-37153, doi:10.1074/jbc.M112.398164 (2012).

191 Stockklausner, C. & Klocker, N. Surface expression of inward rectifier potassium channels is controlled by selective Golgi export. *J Biol Chem* **278**, 17000-17005, doi:10.1074/jbc.M212243200 (2003).

192 Chatelain, F. C. *et al.* TWIK1, a unique background channel with variable ion selectivity. *Proc Natl Acad Sci U S A* **109**, 5499-5504, doi:10.1073/pnas.1201132109 (2012).

193 Renigunta, V. *et al.* Cooperative endocytosis of the endosomal SNARE protein syntaxin-8 and the potassium channel TASK-1. *Mol Biol Cell* **25**, 1877-1891, doi:10.1091/mbc.E13-10-0592 (2014).

194 Rescher, U. & Gerke, V. S100A10/p11: family, friends and functions. *Pflugers Arch* **455**, 575-582, doi:10.1007/s00424-007-0313-4 (2008).

195 Sandoz, G. *et al.* Mtap2 is a constituent of the protein network that regulates twik-related K+ channel expression and trafficking. *J Neurosci* **28**, 8545-8552, doi:10.1523/JNEUROSCI.1962-08.2008 (2008).

196 Weaver, C. D., Harden, D., Dworetzky, S. I., Robertson, B. & Knox, R. J. A thallium-sensitive, fluorescence-based assay for detecting and characterizing potassium channel modulators in mammalian cells. *J Biomol Screen* **9**, 671-677, doi:10.1177/1087057104268749 (2004).

197 Deak, F. *et al.* Inhibition of voltage-gated calcium channels by fluoxetine in rat hippocampal pyramidal cells. *Neuropharmacology* **39**, 1029-1036 (2000).

198 Kirsch, G. E. *et al.* Variability in the measurement of hERG potassium channel inhibition: effects of temperature and stimulus pattern. *J Pharmacol Toxicol Methods* **50**, 93-101, doi:10.1016/j.vascn.2004.06.003 (2004).

199 Hahn, S. J. *et al.* Inhibition by fluoxetine of voltage-activated ion channels in rat PC12 cells. *Eur J Pharmacol* **367**, 113-118 (1999).

200 Choi, J. S. *et al.* Mechanism of fluoxetine block of cloned voltage-activated potassium channel Kv1.3. *J Pharmacol Exp Ther* **291**, 1-6 (1999).

201 Traboulsie, A., Chemin, J., Kupfer, E., Nargeot, J. & Lory, P. T-type calcium channels are inhibited by fluoxetine and its metabolite norfluoxetine. *Mol Pharmacol* **69**, 1963-1968, doi:10.1124/mol.105.020842 (2006).

202 Ohno, Y., Hibino, H., Lossin, C., Inanobe, A. & Kurachi, Y. Inhibition of astroglial Kir4.1 channels by selective serotonin reuptake inhibitors. *Brain Res* **1178**, 44-51, doi:10.1016/j.brainres.2007.08.018 (2007).

203 Kennard, L. E. *et al.* Inhibition of the human two-pore domain potassium channel, TREK-1, by fluoxetine and its metabolite norfluoxetine. *Br J Pharmacol* **144**, 821-829, doi:10.1038/sj.bjp.0706068 (2005).

204 Oselkin, M., Tian, D. & Bergold, P. J. Low-dose cardiotonic steroids increase sodium-potassium ATPase activity that protects hippocampal slice cultures from experimental ischemia. *Neurosci Lett* **473**, 67-71, doi:10.1016/j.neulet.2009.10.021 (2010).

205 Brosemer, R. W. Effects of inhibitors of Na+,K+-ATPase on the membrane potentials and neurotransmitter efflux in rat brain slices. *Brain Res* **334**, 125-137 (1985).

206 Fink, S. L. & Cookson, B. T. Apoptosis, pyroptosis, and necrosis: mechanistic description of dead and dying eukaryotic cells. *Infect Immun* **73**, 1907-1916, doi:10.1128/IAI.73.4.1907-1916.2005 (2005).

207 Chen, H. *et al.* Progressive degeneration of retinal and superior collicular functions in mice with sustained ocular hypertension. *Invest Ophthalmol Vis Sci* **56**, 1971-1984, doi:10.1167/iovs.14-15691 (2015).

208 Huang, K. P. The mechanism of protein kinase C activation. *Trends Neurosci* **12**, 425-432 (1989).

209 Herlaar, E. & Brown, Z. p38 MAPK signalling cascades in inflammatory disease. *Mol Med Today* **5**, 439-447 (1999).

210 Raingeaud, J. *et al.* Pro-inflammatory cytokines and environmental stress cause p38 mitogen-activated protein kinase activation by dual phosphorylation on tyrosine and threonine. *J Biol Chem* **270**, 7420-7426 (1995).

211 Zarubin, T. & Han, J. Activation and signaling of the p38 MAP kinase pathway. *Cell Res* **15**, 11-18, doi:10.1038/sj.cr.7290257 (2005).

212 Duda, J., Potschke, C. & Liss, B. Converging roles of ion channels, calcium, metabolic stress, and activity-pattern of substantia nigra dopaminergic neurons in health and Parkinson's disease. *J Neurochem*, doi:10.1111/jnc.13572 (2016).

213 Zhang, Y. *et al.* Probing electrical signals in the retina via graphene-integrated microfluidic platforms. *Nanoscale* **8**, 19043-19049, doi:10.1039/c6nr07290a (2016).

214 Veliev, F., Briancon-Marjollet, A., Bouchiat, V. & Delacour, C. Impact of crystalline quality on neuronal affinity of pristine graphene. *Biomaterials* **86**, 33-41, doi:10.1016/j.biomaterials.2016.01.042 (2016).

215 He, Z. *et al.* The structural development of primary cultured hippocampal neurons on a graphene substrate. *Colloids Surf B Biointerfaces* **146**, 442-451, doi:10.1016/j.colsurfb.2016.06.045 (2016).

216 Lee, J. S. *et al.* Graphene substrate for inducing neurite outgrowth. *Biochem Biophys Res Commun* **460**, 267-273, doi:10.1016/j.bbrc.2015.03.023 (2015).

217 Fabbro, A. *et al.* Graphene-Based Interfaces Do Not Alter Target Nerve Cells. *ACS Nano* **10**, 615-623, doi:10.1021/acsnano.5b05647 (2016).

218 Bendali, A. *et al.* Purified neurons can survive on peptide-free graphene layers. *Adv Healthc Mater* **2**, 929-933, doi:10.1002/adhm.201200347 (2013).

219 Sahni, D. *et al.* Biocompatibility of pristine graphene for neuronal interface. *J Neurosurg Pediatr* **11**, 575-583, doi:10.3171/2013.1.PEDS12374 (2013).

220 Park, H.-B. Effect of Graphene on Growth of Neuroblastoma Cells. *Journal of Microbiology and Biotechnology* **23**, 274-277, doi:10.4014/jmb.1212.12005 (2013).

221 Li, N. *et al.* The promotion of neurite sprouting and outgrowth of mouse hippocampal cells in culture by graphene substrates. *Biomaterials* **32**, 9374-9382, doi:10.1016/j.biomaterials.2011.08.065 (2011).

222 Kuzum, D. *et al.* Transparent and flexible low noise graphene electrodes for simultaneous electrophysiology and neuroimaging. *Nat Commun* **5**, 5259, doi:10.1038/ncomms6259 (2014).

223 Park, D. W. *et al.* Graphene-based carbon-layered electrode array technology for neural imaging and optogenetic applications. *Nat Commun* **5**, 5258, doi:10.1038/ncomms6258 (2014).

224 Meyer-Franke, A., Kaplan, M. R., Pfreiger, F. W. & Barres, B. A. Characterization of the Signaling Interactions That Promote the Survival and Growth of Developing Retinal Ganglion Cells in Culture. *Neuron* **15**, 805-819 (1995).

225 Chen, Q., Kinch, M. S., Lin, T. H., Burridge, K. & Juliano, R. L. Integrin-mediated Cell Adhesion Activates Mitogen-activated Protein Kinases. *The Journal of Biological Chemistry* **269**, 26602-26605 (1994).

226 Kuhn, T. B., Brown, M. D. & Bamburg, J. R. Rac1-dependent actin filament organization in growth cones is necessary for ?1-integrin-mediated advance but not for growth on poly-D-lysine. *Journal of Neurobiology* **37**, 524-540, doi:10.1002/(sici)1097-4695(199812)37:4<524::aid-neu3>3.0.co;2-h (1998).

227 Smalheiser, N. R., Crain, S. M. & Reid, L. M. Laminin as a substrate for retinal axons in vitro. *Developmental Brain Reserach* **12**, 136-140 (1984).

228 Cohen, J., Burne, J. F., McKinlay, C. & Winter, J. The Role of Laminin and the Laminin/Fibronectin Receptor Complex in the Outgrowth of Retinal Ganglion Cell Axons. *Developmental Biology* **122**, 407-418 (1987).

229 Cohen, J. & Johnson, A. R. Differential effects of laminin and merosin on neurite outgrowth by developing retinal ganglion cells. *Journal of Cell Science* **15**, 1-7 (1991).

230 Park, D. W. *et al.* Fabrication and utility of a transparent graphene neural electrode array for electrophysiology, in vivo imaging, and optogenetics. *Nat Protoc* **11**, 2201-2222, doi:10.1038/nprot.2016.127 (2016).

231 Chen, S., Nilsen, J. & Brinton, R. D. Dose and temporal pattern of estrogen exposure determines neuroprotective outcome in hippocampal neurons: therapeutic implications. *Endocrinology* **147**, 5303-5313, doi:10.1210/en.2006-0495 (2006).

232 Grieshaber, P., Lagreze, W. A., Noack, C., Boehringer, D. & Biermann, J. Staining of fluorogold-prelabeled retinal ganglion cells with calcein-AM: A new method for assessing cell vitality. *J Neurosci Methods* **192**, 233-239, doi:10.1016/j.jneumeth.2010.07.037 (2010).

233 Echevarria, F. D., Walker, C. C., Abella, S. K., Won, M. & Sappington, R. M. Stressor-dependent Alterations in Glycoprotein 130: Implications for Glial Cell Reactivity, Cytokine Signaling and Ganglion Cell Health in Glaucoma. *J Clin Exp Ophthalmol* **4** (2013).

234 Kitko, K. E. *et al.* Membrane cholesterol mediates the cellular effects of monolayer graphene substrates. *Nat Commun* **9**, 796, doi:10.1038/s41467-018-03185-0 (2018).